Cosmic Rays and the Atmospheric Electric Field

Reconstruction and Data Analysis of Radio Emission from Air Showers at the Auger Engineering Radio Array

Dissertation
zur Erlangung des Grades
eines Doktors der Naturwissenschaften

dem Fachbereich Physik
der Bergischen Universität Wuppertal

vorgelegt von
Jens Neuser
aus
Siegen

Wuppertal
Oktober 2015

1. Gutachter:
Prof. Dr. Karl-Heinz Kampert
(Bergische Universität Wuppertal)

2. Gutachter:
Dr. Tim Huege
(Karlsruher Institut für Technologie)

Contents

CHAPTER 1

Introduction

Cosmic rays have been investigated by scientists from all over the world for more than a century now. However, still some fundamental questions could not be answered to full detail. Where do they originate from? How are they accelerated to the highest energies? Measuring cosmic ray properties like particle flux, arrival directions and chemical composition is a key component on the road towards a better understanding of the high energy Universe and solving the remaining mysteries of cosmic rays.

The Pierre Auger Observatory, located in Argentina, is dedicated to research this topic. It has been designed to measure extensive air showers induced by primary particles with energies above 10^{18} eV and provides high quality data at the same time with unprecedented statistics by combining the most advanced detection techniques with a large exposure. The experiment is applying a hybrid approach with a surface detector to measure the secondary particles and deduce their lateral distribution and an optical detector for the longitudinal shower development via the detection of fluorescence light. In addition, the synergy of these techniques reduces systemic uncertainties and allows an improved reconstruction of shower parameters by cross-checking the gathered information.

A new detector type was added with the deployment of the Auger Engineering Radio Array, utilizing a method, which has experienced rediscovery in the last decade. Measuring the radio emission of air showers in the MHz range can provide further and especially complementary information of the incoming primary particle. After an extended R&D

phase used for the testing of different hardware, the detector array started data-taking in 2010 and has been operated continuously since then. Beside several achievements in the technological compartment, also first physical results have been published in the recent years. This has led to a much more detailed understanding, particularly on the underlying mechanisms of the emitted radiation. This work is mainly focused on the development of a standardized reconstruction environment and procedure for the data recorded with the radio detector. Furthermore, the influence of the external atmospheric field on the amount of radiated emission and its properties will be investigated.

Chapter 2 will give an introduction on cosmic ray physics, while Chapter 3 is targeted at the basic principles of extensive air showers and their detection. In Chapter 4 the current understanding of radio emission in the context of air showers will be presented as well as some fundamentals on the development of strong atmospheric field conditions. Chapter 5 is dedicated to the Pierre Auger Observatory, while the Auger Engineering Radio Array will be introduced in Chapter 6. In Chapter 7 the general analysis framework of the experiment and the developments regarding the standard radio reconstruction RdObserver will be discussed. Chapter 8 is focused on the improvements with respect to algorithms and parameters that have been made inside the RdObserver procedure, while Chapter 9 presents the results of the analysis of the influence of the atmospheric conditions. Finally, Chapter 10 yields a summary of the obtained results and conclusions as well as an outlook and suggestions for further analysis.

CHAPTER 2

Cosmic Rays

For more than 100 years cosmic rays are now under investigation by several generations of physicists. Still many questions have not been answered to full extend. But what are cosmic rays? In a first approach, a cosmiy ray is an elementary particle, which originates from an astrophysical object. It traverses the interstellar medium, due to its incredibly high energy, and can be measured afterwards at an observer, e.g. at Earth. Although cosmic rays can be of any particle type, in most cases the term refers to the charged ones. They are categorized by their energy (c.f. Section 2.1) and chemical composition (c.f. Section 2.2).

The history of cosmic rays started in the beginning of the 20th century, when Charles Wilson set up an experiment to investigate the self-discharge of perfectly insulated electrostatic devices. Already at that time it was known, that this phenomenon could be understood by free ionized particles in the atmosphere, but there was no explaination, where those particles should originate from. Therefore, Wilson performed a variety of measurements with a gold leaf electroscope, but he could not find any variation in different atmospheric conditions and concluded, that these ions were formed randomly within the air. Radioactive isotopes in the Earth's crust seemed plausible candidates to be the origin of this ionizing radiation, as it showed similar properties to radioactive rays. Therefore, the amount of ionization should decrease when moving further up in the atmosphere.

Inspired by results of Theodor Wulf, who had shown that the amount of radiation on top of the Eiffel Tower was higher then expected by the current theory, Victor Franz Hess,

a physicist from Austria, initiated ballon ascents in 1912 to measure the ionization as a function of height. Using an improved and hermetically sealed electroscope he found, that up to a height of 1000 m the ionization was decreasing as expected. But while ascending even further, he recognized that it was rising again, reaching almost the amount as on ground level at approximately 3000 m height and further increasing above. Thus, he concluded that this effect might be attributed to a yet unknown, but highly penetrating radiation from outer space moving through the Earth's atmosphere [1]. This discovery of the "Cosmic Radiation" was awarded with a shared Nobel prize in 1936.

Three years later, Pierre Auger, a french physicist, performed a series of cosmic ray experiments in the Swiss Alps using a setup of detectors with a spacing of 300 m similar to Kohlhörster before. He could measure coincident hits in different detectors and concluded that it is not a single particle, but a whole cascade of secondary particle, which is formed in the atmosphere, if the energy of the incoming primary is high enough, and can be measured at ground level [2]. This effect became known as extensive air shower (EAS).

In 1962, Askaryan was the first to predict a radio emission from an EAS [3]. Due to an excess of negative charges in the shower front he calculated a coherent radiation in the MHz regime. A first measurement of radio pulses in coincidence with EAS was published by Jelley et al. in 1965 [4]. Only one year and few experimental results later another emission mechanism was proposed by Kahn and Lerche [5, 6]. They stated that the radiation caused by the deflection of the charged particles in the Earth's magnetic field adds an important contribution to the measured radio pulse. A summary report written by Allan in 1971 concludes that this geomagnetic emission is expected to be the dominant one [7].

After some years of oblivion the detailed measurement of EAS has experienced a renewed growth of interest, especially with the deployment of very large detector arrays like the Pierre Auger Observatory. In this context, also the radio technique has been revisited and first small scale experiments like LOPES [8] and CODALEMA [9] have shown the general feasibility of qualitive air shower measurements via their radio emission. The Auger Engineering Radio Array (AERA) at the Pierre Auger Observatory is designed to measure these pulses for showers with the highest energies ($E > 10^{17}$ eV). It has significantly improved the technological development of the radio technique and the insight on the underlying physical processes (see Chapter 6).

2.1 Energy Spectrum

The energy spectrum of cosmic rays is probably one of the best-known physical quantities. Starting at some MeV it has been measured up to energies of 10^{20} eV, which is way higher than any currently reached energy of man-made particle accelerators. In this range the

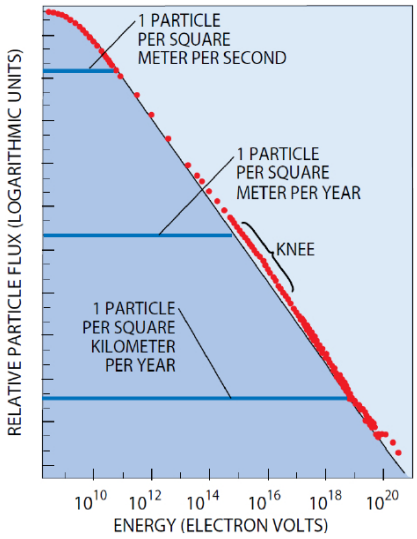

Figure 2.1: Overview of the full energy spectrum of cosmic rays (from [14]).

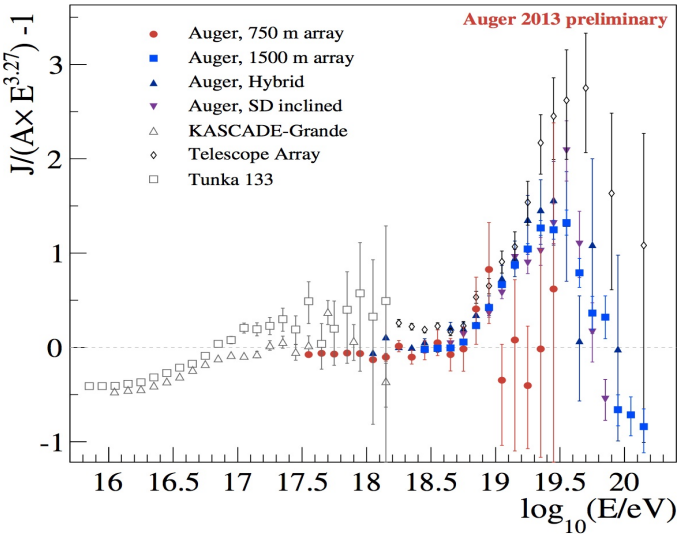

Figure 2.2: Measured spectra of cosmic rays at the highest energies for several air shower experiments scaled with $E^{3.27}$ (from [15]).

flux is constantly decreasing with approximately several particles per m^2 per second at 100 GeV, while at the highest energies only 1 particle per km^2 and year can be observed. Therefore, the measurement of cosmic rays requires different approaches. At lower energies the flux is still large enough to be directly measured with airborne experiments on top of the atmosphere (e.g. [10, 11]). Whereas, for energies above 10^{12} eV one has to use the atmosphere as a detector and observe the remnants of the primary particle, i.e. the secondary particles in the EAS, using large detector arrays on ground level (e.g. [12, 13]). Figure 2.1 shows the overall energy spectrum of cosmic rays. It can be well described by an inverse power law with a differential flux as

$$\frac{dN}{dE} \propto E^{-\gamma}. \tag{2.1}$$

While the lower regions of the spectrum are rather smooth with $\gamma = 2.7$, some prominent features appear at the higher energies. The so-called *knee* at an energy of $E \leq 3 \times 10^{15}$ eV marks the point, where galactic sources are not able to accelerate lighter elements [16]. Here, the spectral index changes to $\gamma \approx 3.1$ for roughly three decades in energy. At $\sim 4 \times 10^{18}$ eV another structure can be found, which is known as the *ankle* and puts the spectral index back to $\gamma \approx 2.6$. To the current state there are two different explanations for this renewed change. The first one accounts it to the transition from the galactic to the extragalactic component of the cosmic ray flux [17], while in the second one, the so-called "dip"-model, the ankle is created by a modification of the source proton spectrum due to $e^{\pm}$ pair production during propagation [18]. At the highest energy a significant suppression is found with the flux dropping to half the amount as expected from a linear extrapolation of the power law at roughly $E = 10^{19.6}$ eV. This is similar to the expectation from the suppression by the

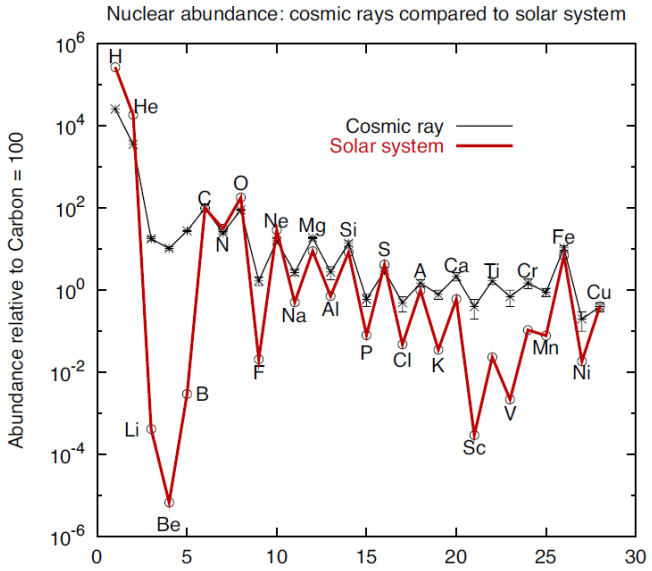

Figure 2.3: Relative abundances of elements in the solar system and in the cosmic ray flux for low energies. The abundances are normalized to Carbon. Modified from [19]

GZK effect, which will be explained in further detail in Section 2.4. All these feature can be illustrated better, when multiplying the spectrum with E^{γ}, with $\gamma \sim 3$. Figure 2.2 shows the energy spectrum as measured by different experiments.

2.2 Composition

The second relevant quantity for the description of cosmic rays is their chemical composition. For lower energies up to some TeV the individual components can be measured directly using airborne and space detectors above the atmosphere. Figure 2.3 shows the relative abundance of different elements in the solar system material and in the cosmic ray flux for these energy regions. In general the cosmic rays follow the abundance in the solar system and are heavily dominated by lighter nuclei with almost 95% being either Hydrogen or Helium. This leads to the assumption that they share the same composition at their origin. Nevertheless, there are some smaller differences. While for Hydrogen and Helium the solar system material has an overabundance, Lithium, Beryllium and Boron as well as some elements slightly lighter than Iron are found more often in cosmic rays. This can be understood by the spallation of heavier nuclei, when interacting with gas and dust particles or the cosmic background radiation during their propagation through the interstellar space. Due to the rapidly decreasing flux of cosmic rays for higher energies an identifcation by direct measurement is no longer possible. Therefore, the particle type has to be deduced from the secondary particles created when the primary interacts with the atmosphere, which

suffers from statistical as well as systematic uncertainties. One option is measuring the mixture of particles at ground level, while the other one is to track the shower development, during the EAS evolves inside the atmosphere (see Section 3.3). A frequently used quantity in this sense is the mean logarithmic mass, which is defined as

$$\langle \ln A \rangle = \sum r_i \ln A_i, \tag{2.2}$$

with r_i as the relative fraction of nuclei i with atomic mass number A_i. It can be used for both approaches as it is proportional to the number of electrons and positrons at ground level

$$\langle \ln A \rangle \propto \log_{10} \left(\frac{N_\mu}{N_e} \right) \tag{2.3}$$

as well as inverse proportional to the depth of the shower maximum

$$\langle \ln A \rangle \propto X_{\max}^{-1}. \tag{2.4}$$

A summary of results of the mean $X_{\max}$ obtained from a number of air shower experiments is displayed in Fig. 2.4. Up to an energy of $\sim 4 \times 10^{15}$ eV (the *knee*), there is a trend from a mixed towards a lighter composition of elements. For the next decade in energy though, the composition shows an increase in mass again, which can be explained by breaks in the energy spectra for some elements [20]. Above 10^{17} eV (the *ankle*) the composition experiences a slow, but constant change towards lighter elements again. This energy range is under current testing by the low-energy enhancements of the Pierre Auger Observatory (see Section 5.2) including AERA. The composition at the highest energies is still not measured to a sufficient detail and therefore quite indistinct, suffering especially from statistical errors due to the low flux in this regime. Nevertheless, measurements by the Pierre Auger Observatory and the Telescope Array have increased the energy range up to almost 10^{20} eV. Figure 2.5 shows the latest results on the composition of cosmic rays of the Pierre Auger Observatory. One can see, that the mean depth of the shower maximum as well as its RMS both show a change towards a heavier composition for ultra-high energies $E \geq 10^{19}$ eV.

2.3 Sources and acceleration

With the cosmic ray energy spectrum reaching up to the highest energies ever measured, the search for the origin of these particles is still one of the most researched and discussed questions in the field. From measurements of the magnetic field it is well understood that only particles up to energies of $\sim 10^{16}$ eV can be confined inside of our galaxy, so especially the origin of ultra-high energy cosmic rays (UHECR) with $E > 1$ EeV has to be outside of the Milky Way. Currently there are two favored models for the acceleration of cosmic rays, which will be discussed in the following:

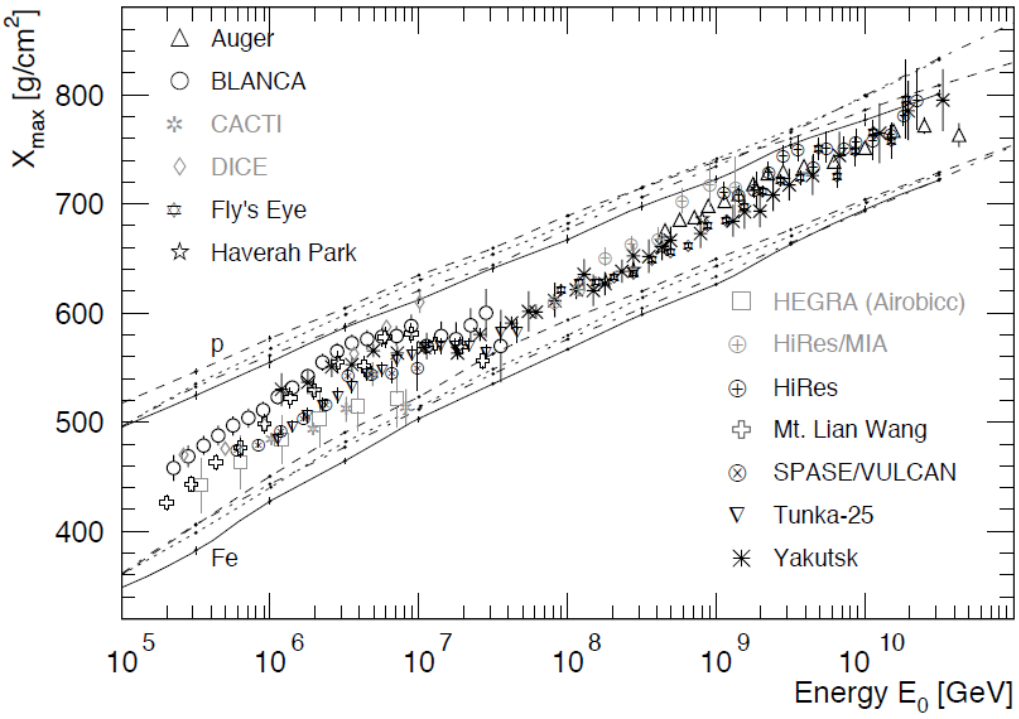

Figure 2.4: Average depth of shower maximum $X_{\max}$ as a function of primary energy E_0 taken from [21]. Shown are experimental results from Auger [22], BLANCA [23], CACTI [24], DICE [25], Fly's Eye [26], Haverah Park [27], HEGRA [28], HiRes/MIA [29], HiRes [30], Mt. Lian Wang [31], SPASE/VOLCAN [32], Tunka-25 [33] and Yakutsk [34]. The results are compared to predictions from simulations for proton and iron induced showers using the CORSIKA code with the hadronic interaction model QGSJET 01 (solid) [35], QGSJET II-3 (dashed) [36], SIBYLL 2.1 (dotted) [37] and EPOS 1.6 (dash-dotted) [38].

In the first scenario the particles are produced at lower energies and gain their immense energy by some external acceleration process. Therefore, those models are called *bottom-up*. The most prominent candidate is the stochastic acceleration proposed by Enrico Fermi already in 1949 [43]. Here, the particles interact with cosmic objects like magnetized clouds, while propagating through the interstellar space. As those clouds will have a random orientation and velocity with respect to the particle track, the cosmic ray gains or loses energy. If a particle with primary energy E_0 encounters the magnetized cloud, it gains an amount of $\delta E = \xi E_0$. Therefore, after n encounters the energy E_n is

$$E_n = E_0(1+\xi)^n \tag{2.5}$$

with

$$n = \frac{\ln(E_n/E_0)}{\ln(1+\xi)}. \tag{2.6}$$

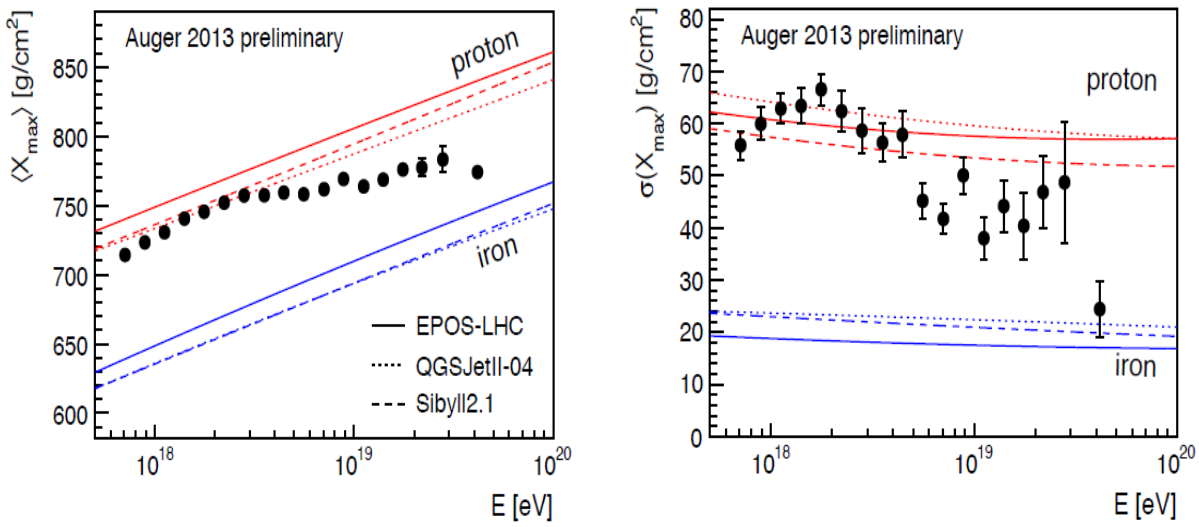

Figure 2.5: Recent measurement of the Pierre Auger Collaboration [39] of the mean $X_{\max}$ (left) and RMS($X_{\max}$) (right) as a function of primary energy E_0 compared to simulations using different interaction models [40–42].

Particles will escape from the region of acceleration with a probability P_{esc} and the probability for a particle to reach E_n goes with $(1 - P_{\text{esc}})^n$. Therefore, the amount of particles with energies larger than E_n is given by

$$N(E > E_n) = N_0 \sum_{m=n}^{\infty} (1 - P_{\text{esc}})^m \propto \frac{1}{P_{\text{esc}}} \left(\frac{E_n}{E_0} \right)^{-\gamma} \tag{2.7}$$

with

$$\gamma = \frac{\ln(1/1 - P_{\text{esc}}))}{\ln(1 + \xi)} \approx \frac{P_{\text{esc}}}{\xi}. \tag{2.8}$$

Thus, the energy spectra resulting from a stochastic acceleration can be described by a power law.

The original proposal from Fermi was driven by the idea, that the probability for a head-on collision of the particle moving within the magnetized cloud is larger than a head-tail collision and therefore in average the particles would be accelerated. It can be shown that for this so-called *second order Fermi acceleration* scenario the fractional energy gain is $\Delta E \propto \frac{4}{3}\beta^2 E$ per cycle, where β is the the velocity of the magnetized cloud [44].

Another mechanism was established in the 1970's by Blandford and Ostriker [45] using plane shock fronts and improving the existing approach, which was a very inefficient and therefore slow process beforehand. Assuming a large shock wave and a shocked gas moving in the downstream direction they found, that in here the fractional energy gain can be written as $\Delta E \propto \frac{4}{3}\beta E$. Due to the linear behavior of this mechanism with respect to β it is

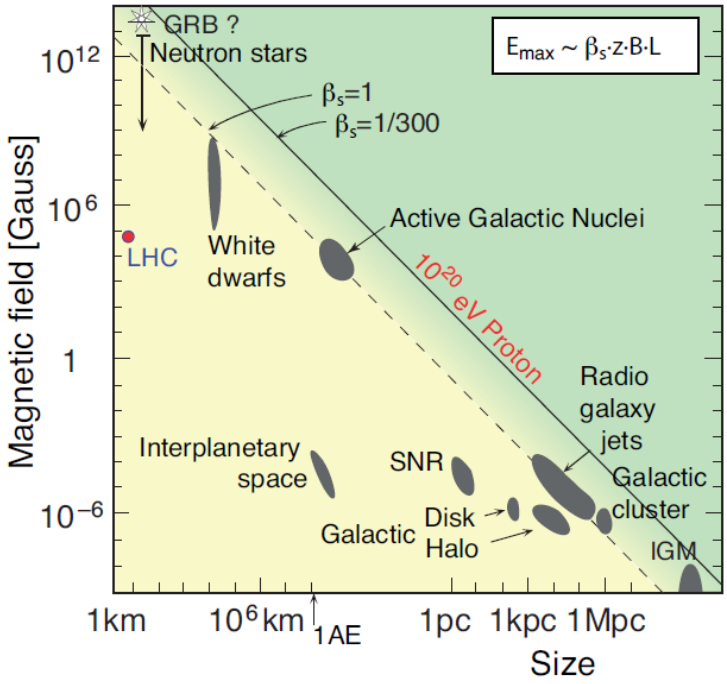

Figure 2.6: The *Hillas plot* showing possible astronomical accelerators with respect to their extend and magnetic field. Candidate sources for energies of $E_{\max} = 10^{20}$ eV for a proton primary have to lie on or above the diagonal lines, which represents equation 2.9 assuming a shock acceleration with velocity $\beta_s = 1$ (dashed) and $\beta_s = 1/300$ (solid). From [21], originally in [17].

called *first order Fermi acceleration* and thus more efficient then Fermi's first proposal due to $\beta < 1$.

However, both mechanisms can only contribute to a gain in energy as long as the particle is inside the acceleration region. Magnetic fields can confine particles with the Larmor radius r_L to a region of size L as long as $r_L < L$. Therefore, the maximum reachable energy $E_{\max}$ is proportional to L and the magnetic field strength, B, in the source. This relation was firstly summarized by A. M. Hillas [17] to be

$$E_{\max} \approx \frac{1}{2} \frac{B}{\mu\mathrm{G}} \frac{L}{\mathrm{kpc}} \beta_s Z \times 10^{18}\mathrm{eV}, \tag{2.9}$$

with the shock velocity, β_s, and the atomic number, Z. This dependency of Z leads to a decreasing efficency for lighter elemetents and can be used to explain the measured features in the cosmic ray energy spectrum between the ankle and the knee as already discussed in Section 2.4. Assuming typical values for galactic supernovae with $B \approx 100\mu$G, $L \approx 1$pc and $\beta_s \approx 1/40$ results in a maximum energy of $E_{\max} \approx Z \times 10^{15}$ eV and makes supernovae a well-suited candidate for the acceleration of cosmic rays in this energy region. A graphical representation of Eq. 2.9 can be found in Fig. 2.6 showing also some possible astronomical

accelerators. Candidates for the acceleration of a 10^{20} eV proton primary have to lie on or above the diagonal to fulfill the constraints on the combination of magnetic field strength and size of the acceleration region. Therefore, only some source types remain in the pool of candiates: Active galactic nuclei (AGN), gamma ray bursts (GRB), neutron stars and radio galaxy jets. Those will be briefly described in the following:

- *Active Galactic Nuclei (AGN):* One of the most favoured sources of UHECR. Having a typical size of $R \approx 10^{-2}$ pc and a magnetic field of $B \approx 5$ G they fulfill the criteria for pushing protons up to the highest energies. They gain their power by accreting matter into a supermassive black hole with about $10^6 - 10^8$ solar masses. Unfortunately, there is also a huge energy loss in regions of high field density, which limits the maximum energy for protons and prohibits the escape of heavier nuclei at all. Considering AGNs as sources one can look for anistropies in the arrival direction of CRs and correlate them with the position of nearby AGNs. This was done e.g. with data from the Pierre Auger Observatory and is discussed in Section 2.5.

- *Gamma Ray Bursts (GRBs):* The collapse of a massive star or the merging of black holes could be a possible explantion for the detected huge bursts of gamma rays up to GeV energies. These gamma rays are emitted via synchroton radiation and inverse Compton scattering by highly relativistic electrons. Therefore, it is necessary to accelerate electrons and also protons to the highest energies. The energy release in the burst time is consistent with the required luminosity for cosmic rays above 10^{19} eV. But also here a limitiation, namely the huge distance of GRBs (up to $z = 5$), gives constraints on this model.

- *Neutron stars:* Rotating neutron stars or pulsars could accelerate particles to very high energies. For a magnetic field of $B \approx 10^{12}$ G, a star radius of $R \approx 10$ km and an angular velocity of about 50 Hz we end up with a maximal energy of about 10^{18} eV.

- *Radio galaxies:* Termination shocks of jets from radio galaxies extend more than 100 kpc and can have magnetic fields, which are sufficient for an acceleration of UHECR up to $E \approx 10^{20}$ eV. Additionaly, no adiabatic deceleration is expected as these shocks are already inside the extragalactic space. A possible candidate galaxy, Centaurus A, has been investigated e.g. in [46].

For a more detailed description of the source candidates compare [47].

The second approach explains UHECR by the decay of super-massive particles, which are assumed to be relicts of some high energetic processes in the early universe. Possible candidates are topological defects [48, 49], super heavy dark matter [50, 51], QCD fragmentation [52] or the Z-burst model [53, 54]. The so created particles with a mass of $m_\chi > 10^{20}$ eV mostly decay into leptons and quarks. The latter ones then produce

hadronic jets built out of mesons (pions) and a small amount of baryons (nucleons). The pions afterwards decay again into electrons / positrons, neutrinos and a large fraction of photons. As the decay products carry only a small portion of the primary energy these are the so-called *top-down* models. Nevertheless, due to the current experimental limits on the flux of ultra-high energy (UHE) photons [55], these models are highly disfavored with respect to the bottom-up approach.

2.4 Propagation

After they have left the source region the propagation direction of the cosmic ray is influenced by galactic and extragalactic magnetic fields, while travelling towards the Earth. Within our galaxy the magnetic fields are known to be regular structured and mainly uniform on a kpc scale with a value of a few µG. Therefore, energetic cosmic rays can not kept confined inside the galactic plane. As the Larmor radius is proportional to the charge of the cosmic ray this loss will happen at varying energies for different primary particles. This can explain the increase of the spectral index of the cosmic ray spectrum above the ankle as well as the shift towards a heavier composition as indicated by the $X_{\max}$ measurements.

The strenth of the extragalactic magnetic field is only known rather poorly, an average estimate is in the order of a few nG [56, 57]. As the distance between galaxies can be in the order of several 10 Mpc, this would lead to a significant deflection of the cosmic ray direction resulting in a bias of the measured energy spectra as lower energy particles could not propagate through fields of this strength and extend [58].

In addition to the influence of the magnetic field, attenuation of the cosmic ray flux plays an important role during the propagation process. While performing some radio astronomy measurements with a horn antenna A. Penzias and R. Wilson found an unexpected excess at 3.5 K antenna tempurature [59], which turned out to be the cosmic microwave background (CMB) radiation. The discovery of this relict of the creation stage of our universe was awarded with the Nobel prize in 1978. Greisen [60] and independently Zatsepin and Kuzmin [61] proposed, that due to this radiation the universe should become intransparent for protons as pion production sets in via an intermediate baryon resonance described by:

$$p + \gamma_{CMB} \longrightarrow \Delta^+(1232) \longrightarrow n + \pi^+ \tag{2.10}$$

$$\longrightarrow p + \pi^0. \tag{2.11}$$

The threshold energy for a head-on collision is defined as

$$E^{\pi}_{\text{th}} = \frac{m_\pi(2m_p + m_\pi)}{4\epsilon} \simeq 6.8 \times 10^{19}\text{eV}, \tag{2.12}$$

with the typical CMB photon energy of about 10 meV, the pion mass, m_π, and the proton mass, m_p. This distinct cutoff of the energy spectrum is know as the *GZK-suppression*.

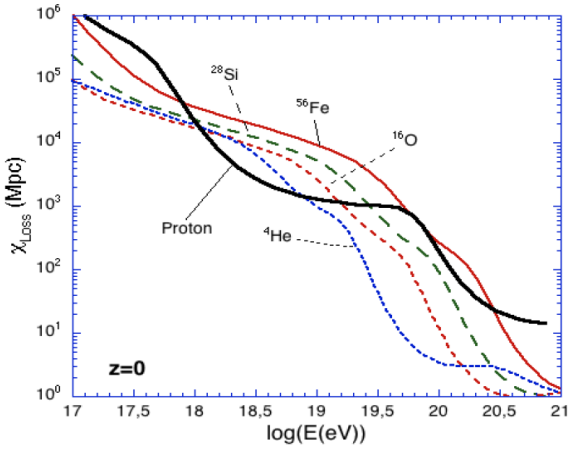

Figure 2.7: Attenuation length for different primary particles as function of the cosmic ray energy for redshift $z = 0$. The initiation of the pair and pion production at their respective energies are clearly visible for protons (solid black line). From [63].

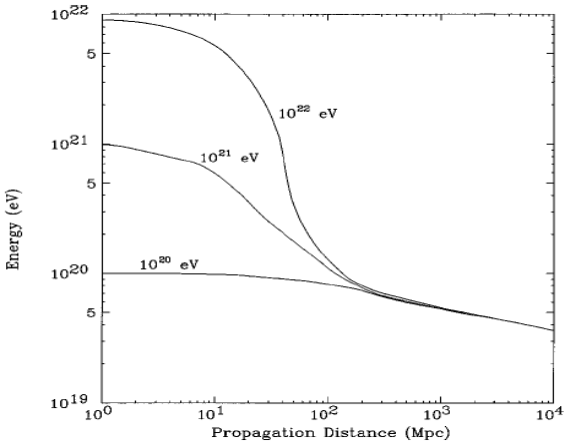

Figure 2.8: Development of the mean energy of the proton energy with respect to the propagation distance through the extragalactic cosmic background radiation for different source energies E_0. From [64].

Already at lower energies the $e^{\pm}$ pair production leads to an additional significant energy loss. It can be described as:

$$p + \gamma_{\mathrm{CMB}} \longrightarrow p + e^{+} + e^{-}. \tag{2.13}$$

This is also known as the Bethe-Heitler process with a threshold energy of

$$E^{e}_{\mathrm{th}} = \frac{m_e(m_p + m_e)}{\epsilon} \simeq 4.8 \times 10^{17}\mathrm{eV}, \tag{2.14}$$

with m_e and m_p as the electron and proton mass, respectively. For energies above the GZK-suppression this production process plays only a very minor role as the characteristic time for $e^{\pm}$ production is in the order of 10^9 years [62].

Figure 2.7 shows these two processes in the context of the attenuation length for various particle types. The strong decrease due to the above discussed features are clearly visible at their corresponding energy for protons. Nonetheless, several experiments have reported the measurements of air shower events with $E > 10^{20}$ eV with Volcano Ranch [65] being the first one in 1966. The most recent results have been presented by the HiRES experiment, which observed a break in the cosmic ray flux at 6×10^{19} eV with a 4σ significance [66], and the Pierre Auger Observatory, which reported a flux suppression of more than 20σ above $\sim 4 \times 10^{19}$ eV [67].

This puts another restriction to the list of source candidates for UHECR protons. As can be seen in Fig. 2.8, the energy of a proton primary averages to the same energy well below

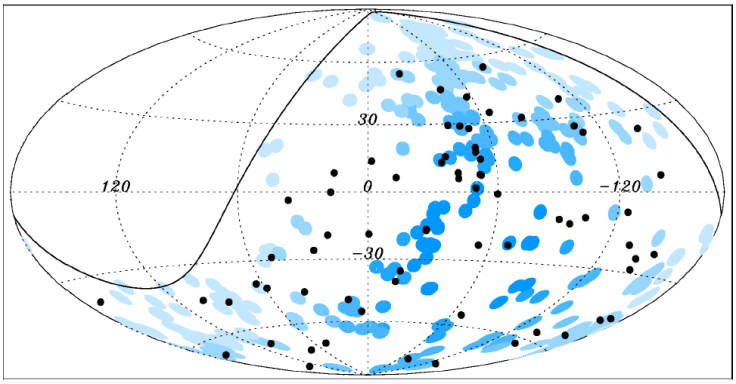

Figure 2.9: The arrival directions of CRs with energy E $\geq$ 55 EeV detected by the Pierre Auger Observatory up to 31 December 2009 are plotted as black dots in galactic coordinates. The solid line represents the field of view of the Southern Observatory for zenith angles smaller than 60°. Blue circles of radius 3.1° are centred at the positions of the AGNs in the VCV catalog within 75 Mpc and within the field of view of the Observatory. Darker blue indicates larger relative exposure. The exposure-weighted fraction of the sky covered by the blue circles is 21%. From [71].

10^{20} eV for traveled distances larger than 100 Mpc. Therefore, the observation of cosmic rays above that cutoff threshold implies sources in close vicinity to the Earth.

2.5 Anisotropy

A promising way to identify the origin of cosmic rays is to check for anistropies in their arrival directions and correlate them with the known positions of point sources or source regions of a specific type. However, due to the multitude of unknown factors in the modeling of the galactic and extragalactic magnetic fields this is still a difficult approach. As already discussed in Section 2.4 it is not expected to find any point sources of charged cosmic rays with an energy of $E \lesssim 1$ PeV within the Milky Way. This of course does not hold for the highest energies. Several experiments reported an excess in the arrival directions from the Galactic Center and the Cygnus region for energies of $E \approx 1$ EeV [68, 69]. In contrast to that an analysis by the Pierre Auger Observatory did not reveal any regional excesses [70]. However, an anisotropy analysis performed in 2007 on data from the Pierre Auger Observatory, which correlated AGNs with cosmic ray arrival directions yielded a significant result [72]. AGN positions were taken from the Véron-Cetty & Véron catalog [73] with a cut on the maximum red-shift of $z_{\max} < 0.017 \mathrel{\widehat{=}} D_{\max} < 75 Mpc$. It was found that 8 out of 13 cosmic ray events with energies above $E_{\mathrm{th}} = 5.7 \times 10^{19}$ eV correlate with these positions within an angular window of $\psi = 3.1°$, while the isotropic expectation is 2.7 events, i.e. 21%. This yields a probabilty 1.7×10^{-3} to happen by chance.

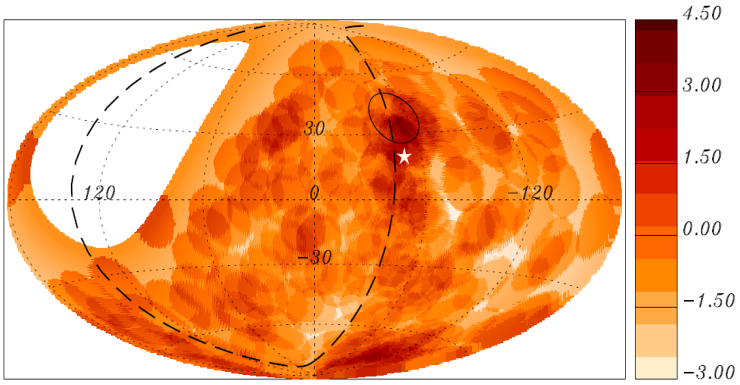

Figure 2.10: Map in Galactic coordinates of the Li-Ma significances of overdensities in 12°-radius windows for the events with E $\geq$ 54 EeV. The highest significant region at longitude and latitude $(l, b) = (-51.1°, 37.6°)$ is marked with a black circle. Also indicated are the Super-Galactic Plane (dashed line) and Centaurus A (white star). From [46].

A further analysis using an enlarged dataset still showed a level of correlation of $37^{+7}_{-6}\%$, thus weaker, but still above istropocic expectations [71]. A map of the events and AGNs used in this analysis can be seen in Fig. 2.9. A recent publication, using now almost ten years of Pierre Auger data, presented an updated fraction of correlation of $28.1^{3.8}_{3.6}\%$, which is now only 2σ above the isotropic expectation of 21%. Therefore, it was concluded that the initial correlation was probably affected by a statistical fluctuation and that this particular test does currently not yield a significant indication of anisotropy [46].

In the same publication a numerous amount of additional anisotropy tests have been performed, inter alia a blind search for excesses over the visible sky. Here, the binomial probabilty to find an equal or larger amount of events in an isotropic flux than found in data was calculated for windows with varying radii $1° < \psi < 30°$ on a $1° \times 1°$ grid. The minimum probability was found in a 12° window at the Galactic coordinates $(l, b) = (-51.1°, 37.6°)$ with an energy threshold of $E_{\mathrm{th}} = 5.4 \times 10^{19}$ eV, yielding a Li-Ma significance of 4.3σ. This region is not only close to the Super-Galactic plane, but also centered at about 18° from the direction of Centaurus A. The Li-Ma map for the events in the whole visible sky is shown in Fig. 2.10. Nevertheless, it turned out that the found excess is compatible with the maximum excess produced by iostropic simulations. Overall, none of the tests in [46] yields a statistically significant evidence of a non-istropic distribution of UHECR with the current data.

CHAPTER 3

Extensive Air Showers

3.1 Shower development

The detection of air showers is the only practicable way of measuring cosmic rays with energies above 10^{14} eV due to the very low flux in this regime. The Earth's atmosphere is not transparent for cosmic rays with such energies and therefore, the primary particle will interact with an air nucleus and produce secondary particles in these collisions. The energy will be split among a leading baryon, kaons as well as pions. This second generation of particles still carries enough energy to interact again and produce further sub-generations, thus leading to a whole cascade of particles, which is then called an *extensive air shower* (EAS). A schematic view can be seen in Fig. 3.1.

This air shower is moving through the atmosphere as a thin disc with almost the speed of light. Its longitudinal extend is only some meters, whereas the lateral radius can be up to several kilometers. During the development of the shower hadronic and electromagnetic interactions take place as well as particle decays. This leads to three different shower components, which will be discussed in more detail in Section 3.2. In the beginning the number of particles rises multiplicatively with each new generation until a maximum is reached. At this point the particle do not have enough energy to produce new particles anymore and the shower attenuates again. The longitudinal development of the shower is described by the *slant depth*, X, which is measured in g/cm^2. This parameter quantifies the

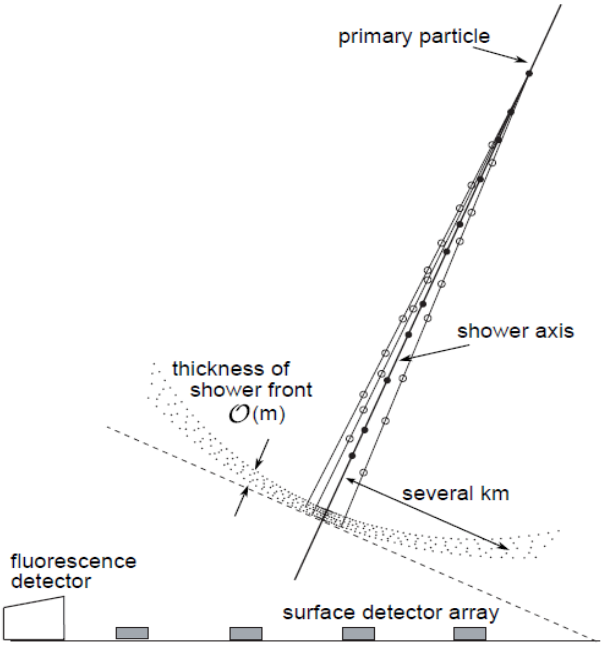

Figure 3.1: Schematic view of an air shower with the primary particle. The shower axis and the slightly curved shower disc is shown as well as different detection techniques. From [74].

amount of matter traversed by the particle cascade starting at the top of the atmosphere. Using the density profile of the atmosphere, $\rho(h)$, one can calculate the vertical atmospheric depth

$$X_{\text{vert}} = \int_h^\infty \rho(h')dh, \tag{3.1}$$

which then translates into the slant depth as

$$X = \frac{X_{\text{vert}}}{\cos(\theta)} \tag{3.2}$$

with θ as the zenith angle of the shower. A simple model to understand the main feature of the cascade development was invented by Heitler [75], who describes the propagation of particles of the same type. After the primary particle with energy E_0 has traveled one interaction lenght λ it produces two new particles carrying each half the amount of the initial energy $E_1 = E_0/2$. This process continues, doubling the number of particles and sharing the energy, until the critical energy E_c for particle splitting is reached. This maximum is reached at a depth

$$X_{\text{max}} = \lambda \frac{\ln(E_0/E_c)}{\ln(2)} \tag{3.3}$$

with a maximum number of particles

$$N_{\text{max}} = E_0/E_c. \tag{3.4}$$

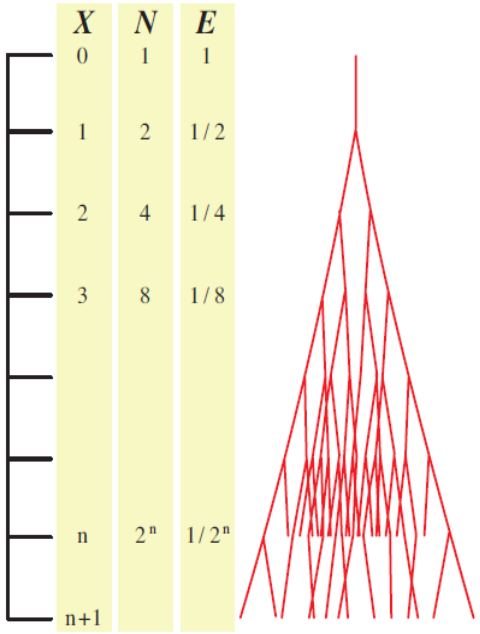

Figure 3.2: The cascade toy model by Heitler with E as the energy, N the number of particles and $X = n\lambda$ the slant depth.

After this point particles only lose their energy, decay or get absorbed. A schematic representation of the Heitler model is shown in Fig. 3.2. Electromagnetic as well as hadronic cascades can be described qualitatively rather well with this simple model using the main properties of Eq.s 3.3 and 3.4.

A more detailed description of the particle propagation inside the atmosphere can be achieved by using cascade equations. They are described e.g. in [19] and have been implemented in air shower simulation codes like CONEX [76].

To account for the development of air showers for different primary particles one can use the superposition model. Here, a nucleus of mass A and energy E_0 is treated like A equivalent nuclei, which share the same amount of energy E_0/A each and have a similar distribution of first interactions. This translates Eq. 3.3 into

$$X_{\max} \propto \ln\left(\frac{E_0}{A \cdot E_c}\right), \tag{3.5}$$

which yields that showers initiated by heavy primary particles have their first interaction X_0 and thus their maximum $X_{\max}$ at a lower slanth depth and therefore, develop more rapidly than showers from lighter elements. This behaviour has been verified by air shower simulations and two example showers for a proton and an iron primary are shown in Fig. 3.3. A parametrization for the longitudinal development of an air shower, which was developed by Gaisser and Hillas [80] using the point of first interaction, X_0, the shower maximum,

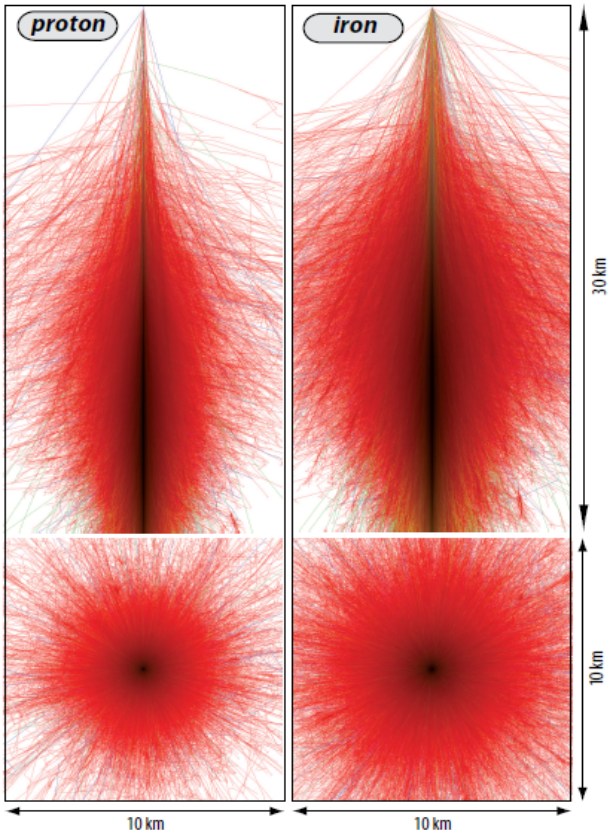

Figure 3.3: Top pictures: Longitudinal shower development of proton and iron induced showers with $E = 10^{14}$ eV from CORSIKA simulations [77, 78]. Electrons/positrons in red, photons in green and hadrons in black. Bottom pictures: xy-projection of the above shower. From [79].

$X_{\max}$, the maximum number of particles, $N_{\max}$, and the mean free path length, λ, is given by

$$N(X) = N_{\max} \left(\frac{X - X_0}{X_{\max} - X_0} \right)^{\frac{X_{\max} - X_0}{\lambda}} \exp\left(-\frac{X - X_{\max}}{\lambda} \right). \tag{3.6}$$

The lateral profile of the shower at ground level respectively the thickness of the shower disc is heavily dependent on the energy of the primary particle. In general, the number of particles can be calculated by integrating over the particle density

$$N(r) = \int n(r)\mathrm{d}r \propto \int S(r)\mathrm{d}r. \tag{3.7}$$

Nevertheless, air shower measurements are performed with detectors placed with discrete distances r from the shower axis. Thus, a lateral distribution function (LDF) is needed for a continuous estimate of the particle density. This will be discussed in Section 3.3.2.

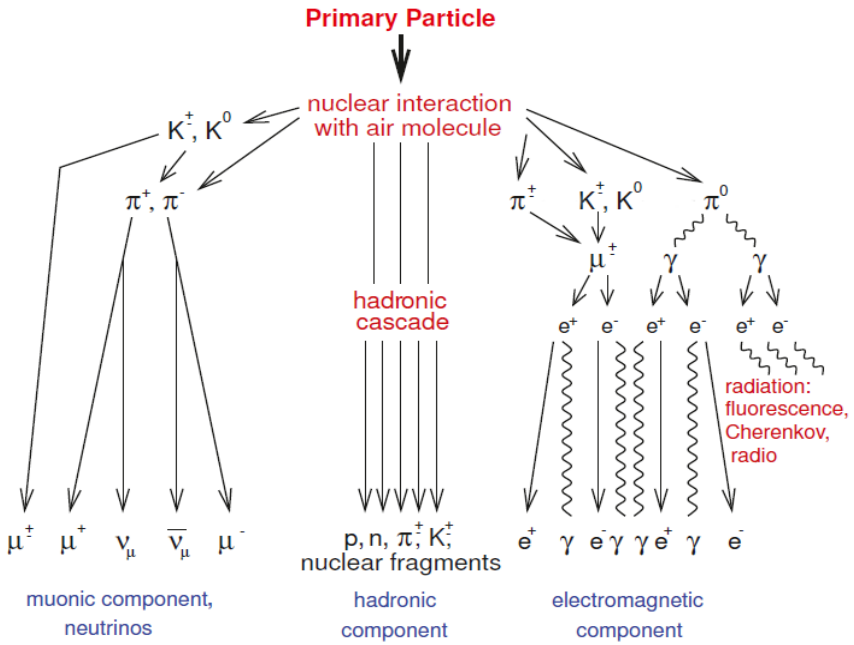

Figure 3.4: Scheme of an air shower development initiated by a cosmic ray nucleus. Modified from [81].

3.2 Components

During its development the air shower can be split into three seperate components, the hadronic, the electromagnetic and the muonic component as depicted in Fig. 3.4. As the primary particles are mainly nuclei the first interaction taking place in the atmosphere is a hadronic one, producing further generations of hadrons, mostly pions and kaons from collisions. As shown in Fig. 3.3 the hadronic particles form the central area of the air shower and therefore are often refered to as the *shower core*, which is also initializing the other components.

Despite the already discussed difference in the depth of the first interaction in the atmosphere and therefore varying $X_{\max}$, also the fluctuations in the position of the shower maximum can be used to estimate the primary composition. Due to their larger interaction length proton primaries will have a wider spread in the distribution than heavier nuclei.

The neutral mesons produced in the hadronic interactions are the main starters for the second component. The decay of pions leads to an electromagnetic cascade

$$\pi^0 \longrightarrow \gamma + \gamma \tag{3.8}$$

$$\pi^0 \longrightarrow \gamma + e^+ + e^-, \tag{3.9}$$

where the first reaction is the dominant one ($\sim 99\%$).

Nevertheless, these cascade can also be initiated directly by high energy electrons or photons via a combination of bremsstrahlung and pair production in the electromagnetic field of a nucleus N

$$e^{\pm} + N \longrightarrow N + e^{\pm} + \gamma \tag{3.10}$$
$$\gamma + N \longrightarrow N + e^{+} + e^{-}. \tag{3.11}$$

This chain continues until the energy loss from ionization is dominating the bremsstrahlung process at $E < E_c \approx 81$ MeV. Below this threshold the electron is attenuated within one radiation length and the electromagnetic component starts to die out.

The third component of an extensive air shower consists of the particles, which are created by the decay of the charged mesons, in this case mainly pions and kaons, of the hadronic component:

$$\pi^{\pm} \longrightarrow \mu^{\pm} + \nu_{\mu}(\bar{\nu}_{\mu}) \tag{3.12}$$
$$K^{\pm} \longrightarrow \mu^{\pm} + \nu_{\mu}(\bar{\nu}_{\mu}). \tag{3.13}$$

The resulting muons are not stable ($\tau_{\mu} \approx 2.2\mu$s), but due to time dilation effects almost all of them reach the ground, if they have an energy of some GeV. The muonic component can be used for composition studies as its magnitude carries information on the primary particle type. Additionally, the muons follow more or less a straight path through the atmosphere as they are not heavily deflected by multiple scattering. Therefore, they can be used to reconstruct the early shower development.

3.3 Methods of Observation

Due to the low flux of UHECRs the currently used techniques for the measurement of air showers are based on ground observations. In the last years two methods have been well established and will be discussed in the following sections: The tracking of the longitudinal shower development via fluorescence light in the atmosphere in Section 3.3.1 and the direct detection of the lateral extend of shower particles with an array of sensors on ground level in Section 3.3.2. Finally, some newly developed or recently revived methods will be presented in Section 3.3.3. An overview of the different detection techniques is depicted in Fig. 3.5.

3.3.1 Optical Observation

While the charged particles of an air shower cross the atmosphere, they exite air molecules (mostly nitrogen). During the de-excitation process fluoresence light in the UV-range

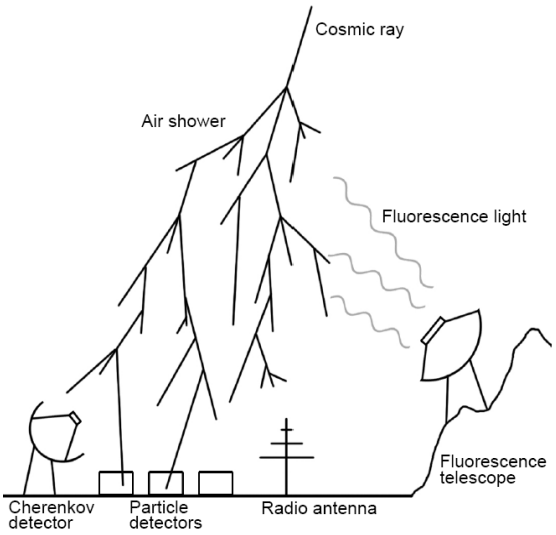

Figure 3.5: Schematic overview of different methods to detect air showers. From [82].

($\lambda \sim 300 - 400$ nm) is emitted istropically, which can be measured by well equipped telescopes even at large distances. This is realized typically by the usage of a camera assembled from photo-multiplier tubes. Here, the development of the shower can been followed as a bright spot moving across the sky, which also allows the reconstruction of the shower axis. The brightness of the spot is a measure for the number of charged particles, but has to be corrected for attenuation in the atmosphere. For an estimation of the amount of energy, which was transfered into the radiated photons the fluorescence yield is needed, which has been measured in dedicated experiments [83]. As this yield is only in the order of 1%, the detection of showers with energies $E < 10^{17}$ eV is very difficult.

This detection technique grants immediate access to the longitudinal energy deposit profile $dE(X)/dX$ of the measured air shower. This profile can be parametrized using a Gaisser-Hillas function as of Eq. 3.6, which yields the total deposited electromagnetic shower energy, when integrated:

$$E_{\mathrm{cal}} = \int \frac{dE}{dX} dX. \tag{3.14}$$

This method allows a very precise determination of the shower maximum $X_{\max}$ with a resolution of $\Delta X_{\max} \sim 20\mathrm{g/cm}^2$, but is limited to excellent observing conditions (dark, cloudless nights), which results in a duty cycle of about 15%. An example event measured by the Pierre Auger Observatory and fitted with Eq. 3.6 is shown in Fig. 3.6. The Fly's eye experimented reported the measurement of air shower with an energy of $E \sim 3.2 \times 10^{20}$ eV, which is the highest measured energy by a fluorescence detector so far [84].

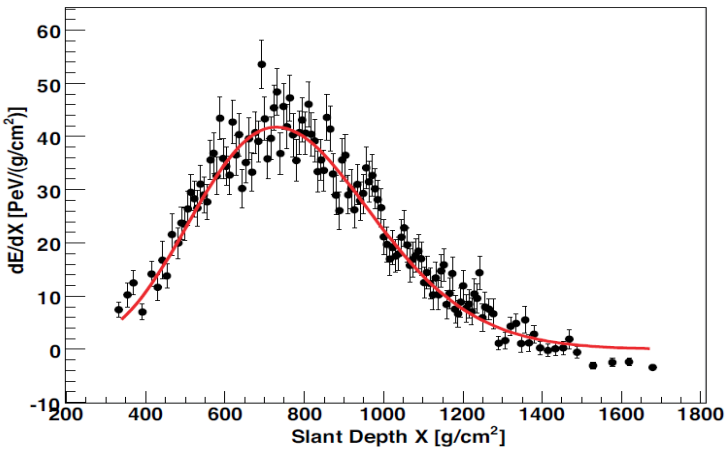

Figure 3.6: Longitudinal profile of an example event measured by the fluorescence detectors of the Pierre Auger Observeratory. Shown is the deposited energy as a function of slant depth. The red line indicates a fit of the Gaisser-Hillas function (Eq. 3.6).

3.3.2 Particle Detection

Air showers can also be detected by measuring the particles as a function of time using arrays of particle detectors, like Cherenkov detectors or scintillators. The individual stations are commonly deployed on regular grids of $\sim$ 1000 m spacing, on the one hand to be able to equip large areas to deal with the low flux of UHECR, on the other hand to still record a sufficient amount of signal information. Thus, the direction of the shower is reconstructed from the relative timing of the individual detectors and the total shower energy can be determined by the particle density at ground using Eq. 3.7 as the total number of particles N_{total} is proportional to the primary particle energy E_p:

$$N_{\text{total}} \propto E_p. \tag{3.15}$$

As already discussed in Section 3.1 a parametrization of the continuous particle distribution, the LDF, is needed for this due to the discrete measurement points. A general approach is given by the Nishimura-Kamara-Greisen (NKG) function [85], which is commonly used in air shower experiments:

$$S(r) = k \left(\frac{r}{r_0}\right)^{-\alpha} \left(1 - \frac{r}{r_0}\right)^{-(\eta-\alpha)} \tag{3.16}$$

with the Molière radius of the air shower, r_0, a scaling factor k and two independent functions α and η, which have to be calculated empirically from data of the individual experiment. The lateral signal distribution of an example event measured with the Pierre Auger Observatory is shown in Fig. 3.7. The advantage of particle detectors is the 100%

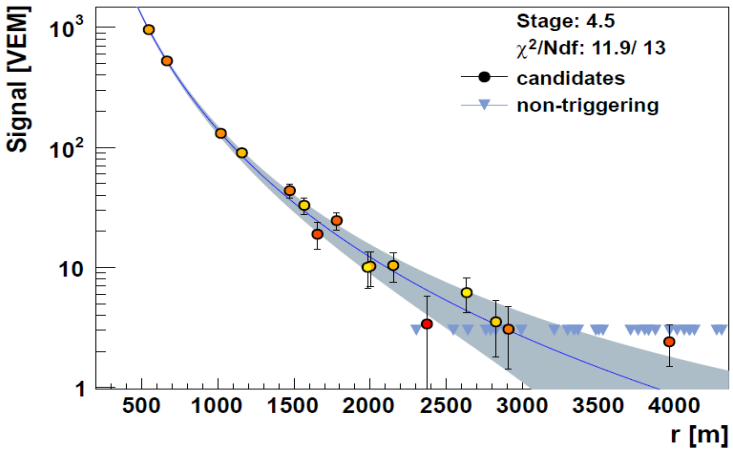

Figure 3.7: Lateral profile of an example event measured by the surface detectors of the Pierre Auger Observatory. Shown is the detector signal as function of the distance to the shower axis. Candidate stations (circles) are color-coded with respect to the signal arrival time from early (yellow) to late (red). The solid line represents a fit of a lateral distribution function (modified version of Eq. 3.16).

duty cycle and the good determinability of the exposure. Nevertheless, measurements by surface arrays only provide a short snapshot of the full shower and thus, need a lot of correction effort to be able to provide information on e.g. the kinetic properties of the primary particle. Their reconstruction requires the use of simulations using hadronic interaction models.

3.3.3 Other methods

In the recent years several other detection techniques have been developed and tested, either as complementary approach to the established methods to overcome their weak points or as addition to existing setups to provide an even more complete picture of the full air shower:

- **Radio detection:** Firstly explored in the 1960s [4], this technique has recently been revived to great success. Radio detectors combine the high-duty cycle of particle detectors with the ability to measure the longitudinal shower development like an optical detector and therefore compose a well-suited alternative to the established techniques. This approach will be discussed in greater detail in Chapter 4.

- **Microwave detection:** Beside the measurement of emission in the MHz range, also radiation in the microwave regime has been studied as possibility for the detection of air showers as a result of laboratory measurements by Gorham et al. [86]. The

molecular bremsstrahlung radiation from collisions of free electrons in the post-shower plasma has been studied by several test facilities and results have been published e.g. in [87–89].

- **Acoustic detection:** If a particle cascade traverses water or ice there is a significant local heating, which leads to expansion of the medium. The resulting bipolar, thermo-acoustic signal can be used to reconstruct the direction of the incoming air shower. Mainly targeting at the detection of cosmogenic neutrions this technique has also found recent renewed interest, almost 50 years past its first description by Askaryan [90].

CHAPTER 4

Radio Emission

In 1962 Askaryan proposed the creation of a radio emission during the development of an extensive air showers [3] and soon after Jelley et al. deployed an experiment at the Jodrell Bank observatory. They used a large array of 72 dipole antennas in East-West direction triggered by a triplet of Geiger-Müller counters. A schematic overview of this experiment is shown in Fig. 4.1. They were the first to successfully detect a radio pulse emitted from an air shower, measuring at radio frequencies around 45 MHz [4]. Some years later Allan et al. performed first systematic studies at the Haverah Park experiment [7]. They investigated the radio signal with respect to primary energy and shower geometry and found the following parametrization for the electric field amplitude:

$$\varepsilon_\nu \left[\mu\mathrm{V\,m^{-1}\,MHz^{-1}}\right] = 20 \cdot \left(\frac{E_p}{10^{17}\mathrm{eV}}\right) \cdot \sin(\alpha) \cdot \cos(\theta) \cdot \exp\left(-\frac{R}{R_0(\nu,\theta)}\right) \tag{4.1}$$

Here, ε_ν is the electric field strength at the normalized bandwidth of the receiver, i.e. center frequency divided by bandwidth, E_p the primary particle energy, α the angle between shower axis and geomagnetic field vector, θ the air shower inclination and R the distance of the observing antenna to the shower axis. $R_0(\nu,\theta)$ is the scale parameter for the exponential, lateral fall-off, which Allan found to vary between $R_0 = 100$ m and $R_0 = 140$ m depending on the receiver frequency and the zenith angle.

However, due to a lack of sufficient hardware at that time the interest in the radio technology vanished as it became clear, that the identification of the underlying emission

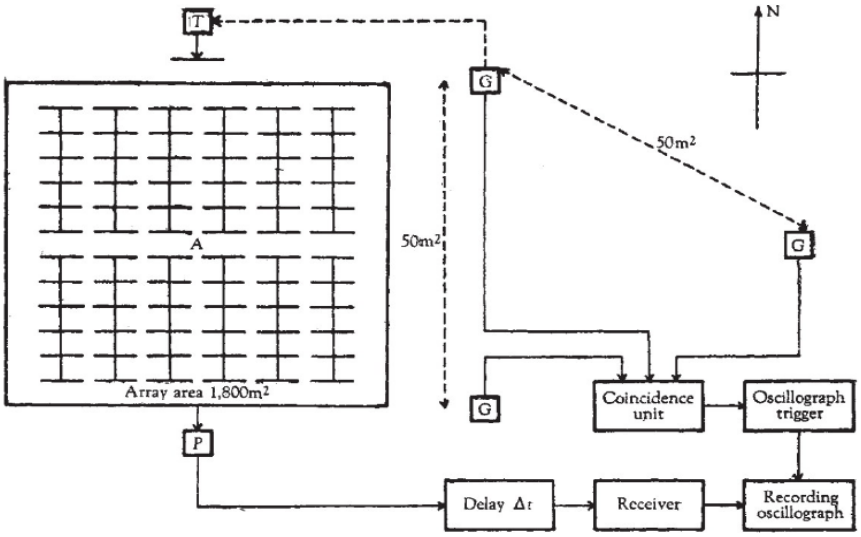

Figure 4.1: Schematic of the experiment at Jodrell Bank. From [4].

processes would not be possible. Only recently, with the advent of digital radio antenna arrays, this identification seemed feasible again and several experiments like LOPES [91], CODALEMA [9], AERA [92], LOFAR [93] and Tunka-Rex [94] have started to re-explore the capability of the radio technique in the MHz regime for the detection of cosmic rays with energies $E > 10^{16}$ eV. Especially LOPES (embedded in the KASCADE detector at the KIT) and CODALEMA (at the Nancay Radio Observatory) were key experiments and have proven the general feasibility of radio detection. The gained knowledged was combined for the design of the first large-scale radio array AERA at the Pierre Auger Observatory, which will be discussed in Chapter 6.

4.1 Emission mechanisms

Today we know that the radio emission from the electromagnetic component of an air shower is a superposition of different mechanisms. The major contribution is known either as *geomagnetic effect* or as *time varying transvers current* and was first introduced by Kahn and Lerche in 1966 [5, 6]. They stated that this effect could be dominating from 30 MHz to 300 MHz. The electrons and positrons are deflected and separated by the Lorentz force

$$\vec{F_{\mathrm{L}}} = q(\vec{v} \times \vec{B}) \tag{4.2}$$

due to the local magnetic field as shown in Fig. 4.2a. This induces a transverse current with a varying strenth depending on the currently present charge in the shower. This current then emits dipole radiation, which is strongly beamed forward in the direction of the shower due to the relativistic velocity of the dipole. An alternative idea concerning the

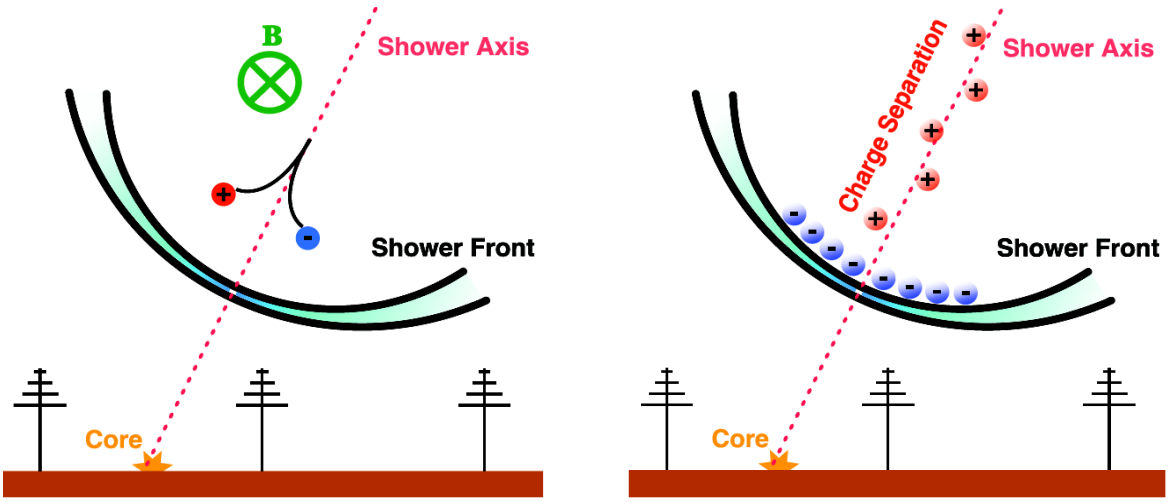

Figure 4.2: Schematic overview of the geomagnetic (a) and charge-excess (b) emission mechanisms. From [98].

geomagnetic emission was published by Falcke and Gorham [95] and followed by Falcke and Huege [96], who modeled the emission as synchrotron radiation from the accelerated electrons and positrons gyrating as pairs in the geomagnetic field. This approach yields the big advantage that the total emission can be seen as superposition of the synchrotron radiation of the single particles. Recent studies have shown though, that this is only a minor contribution in the regime from 30 to 80 MHz [97]. It is not quite clear yet how independent of each other these two models really are. Thus, from this point on we refer to both mechanisms described above, when talking about "geomagnetic" emission. The second mechanism originates from the already mentioned initial ansatz by Askaryan. He assumed that the radio emission results from a superposition of the Cherenkov effect and a charge-excess in the air shower. While the shower particles move faster than the speed of light in air, they emit Cherenkov radiation due to the time compression. This increase of the total emission takes place at the Cherenkov angle α_{Ch}, which is depends on the index of refraction, n, and the relativistic velocity, β. This leads to $\alpha_{\mathrm{Ch}} \sim 1°$ for a typical air shower, which corresponds to a ring of enhanced emission with, depending on the shower geometry, a radius of roughly 100 m from the shower axis. However, the radiation of electrons and positrons, if present in the same amout, would cancel out as they are emitted with opposite phase. Therefore, an excess of one charge is needed for a non-zero amount of emission. Askaryan suggested that the annihilation of shower positrons with electrons from air molecules leads to a negative charge-excess. Later, it was found that the dominant part of the total charge-excess results from knock-on electrons and Compton recoil electrons, while only 10% of the total charge-excess is due to positron annihilation [99]. Due to the dependence of the refractive index n, Cherenkov emission plays a more important role for particle showers in dense media. For extensive air showers the "original" Askaryan emission

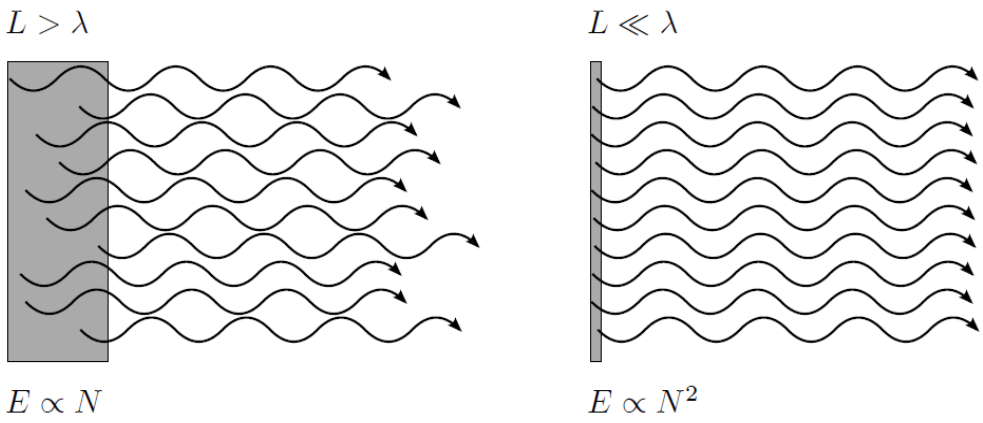

Figure 4.3: Schematic drawing of incoherent versus coherent emission. From [102].

is instead resulting from the varying of the net charge in the shower front as shown in Fig. 4.2b.

Finally, the electric field in the Earth's atmosphere can produce similar radiation mechanism as the geomagnetic field, if enhanced e.g. during thunderstorm conditions. Also here a seperation of the charged particles can result from a strong electric field component perpendicular to the direction of the air shower. As calculated by Charman [100] this geoelectric emission is negligable to the geomagnetic one for normal atmospheric conditions, but can lead to a strong amplification of the radio signal, if a huge field gradient is present. Recently, Buitink et al. [101] have shown by simulations, that not only the strength, but also the polarization of the radio signal can be changed significantly. As a main topic of this thesis, this will be discussed in greater detail in Section 4.5 (atmospheric electric fields) and analyzed in Chapter 9 (radio emission in strong atmospheric fields). One of the most important features for the detection is the coherence of the radio pulses. The basic principle behind the coherence theory is shown in Fig. 4.3. The main contribution for the electromagnetic radiation is located inside the shower front, whose thickness is typically of the order of a few meters. Therefore, the emission is a highly coherent broad-band pulse for wavelength below this measure, i.e. frequencies below 100 MHz. This assumption holds for the geomagnetic as well as the charge-excess approach.

According to [103] the radiated power of a single particle can be written as

$$P_{\text{single}} = \frac{2\gamma^2}{3c^3} \cdot \frac{q^4}{m^2} \cdot \beta_\perp^2 \cdot |\vec{B}|^2, \tag{4.3}$$

with charge q, mass m, transverse particle velocity $\beta_\perp$, Lorentz factor γ and the Earth's magnetic field $\vec{B}$. If we now add the coherence assumption of the whole shower by setting $q = N \cdot q$ and $m = N \cdot m$ we achieve

$$P_{\text{shower}} = \frac{2\gamma^2}{3c^3} \cdot \frac{(Nq)^4}{(Nm)^2} \cdot \beta_\perp^2 \cdot |\vec{B}|^2 = N^2 \cdot P_{\text{single}}. \tag{4.4}$$

Hence, the energy of the radiated pulse P is proportional to the squared number of electrons N^2 in the shower front, which itself scales linearly with the energy of the primary cosmic ray. As the amplitude of the radio signal is proportional to $\sqrt{P}$ a linear increase with respect to the shower energy is expected. This has been shown experimentally by the LOPES measurements [104], confirming that most of the emission is coherent. Additionally, the emitted signal power scales with the strength and orientation of the Earth's magnetic field, which therefore leads to a varying detection threshold with respect to the arrival direction of the shower. In any case, the radio detection provides the possibility for a calorimetric measurement just like the fluorescence method.

Being sensitive to the longitudinal shower development, the determination of $X_{\max}$ and therefore the primary composition seems possible. A property, which might help in this process is the shape of the shower front as a sensitivity of the curvature to the height of the shower maximum has been predicted [105]. Determined by the regions of emission and also the shower geometry, the coherent radio wavefront arrives later at ground level than the particle front due to the index of refraction. It was found to be neither purely spherical [106], which would correspond to a point-source emission, nor conical [107], as expected from continuous emission on a linear path, but can well described by a hyperbola. This means that the size of the emission region is of signifcant, but not to large extend.

The local radio background opposes a minimum detectable energy and forms a detection threshold. The most prominent sources of radio frequency interferences (RFI) are both man-made. On the one hand there are narrow-band transmitter like AM/FM radio, which are well detectable within the frequency spectrum and continuously contribute to the received power. On the other hand short, transient pulses as result from e.g. electronic devices are even harder to handle as they kind of "mimic" real air shower pulses. Some methods to discriminate these pulses are discussed in Section 8.5. A globally existing and mostly constant background is introduced by the diffuse emission of our Galaxy. It can be observed as continuous noise floor in the MHz range [108] and puts a lower limit on the detectable energies of cosmic rays at about 10^{16} eV.

4.2 Emission models

Reliable predictions of the radio emission can nowadays only be made by the use of dedicated models and associated computer simulations. Two approaches, a microscopic and a macroscopic model, have been used for the latest description and will be discussed in this section.

In the microscopic model the total radio signal is calculated by the superposition of the emission contributions of the individual particles during the shower development. This can

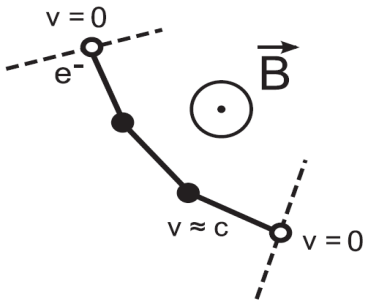

Figure 4.4: Schematic drawing of the endpoint formalism for a single particle track as used in REAS3 and CoREAS. Endpoints are indicated as hollow circles, track "kinks", which are induced by the presence of a magnetic field, as solid circles. From [113].

be made without direct assumption on the actual emission mechanism. This approach is used in the full Monte Carlo simulation codes REAS3 / CoREAS [109], which is based on CORSIKA [77], as well as ZHAires [110] based on Aires [111]. As the simulations in this thesis were performed with CoREAS, we will focus on this code in the following. One of the microscopic methologies, which were implemented in REAS3 and CoREAS is the so-called "end-point" formalism as described in [112]. Here, a series of discrete acceleration and de-acceleration events describes the motion of the shower particles as shown in Fig. 4.4, which leads to hard radiation. The polarization direction of an end- and the following start-point are inverse and therefore, the resulting radiation cancels out when superposed. The remaining radiation results from changes in the particle momentum in between the end-points. Providing a sufficient number of these end-points any classical problem can be reconstructed by a dissection into individual trajectories.

A macroscopic description is encoded in the MGMR [114] and EVA [115] models, which derive the radio emission from the time variation of the net charge, the dipole moment and the transverse current within a shower. Here, the necessary particle input is either parametrized or taken from the air shower simulation CONEX [76]. Using this approach one can derive e.g. a good sensitivity to the early stages of the shower development.

Although these two approaches are fundamentally different, the predictions of all models have started to converge and deliver a consistent description of the current data [97]. Figure 4.5 shows the radio pulses simulated with REAS3 and MGMR for different distances from the shower axis. Both codes predict bipolar pulses with a length of several 10 ns, which was already expected from the coherence criteria, and similar shapes. The pulse amplitudes agree fairly well, especially for larger distances.

Figure 4.6 shows the frequency spectra obtained from REAS3 and MGMR simulations again for different distances to the shower axis. Both sets show a consistent decrease of spectral field strength for higher frequencies, which can be attributed to the reduced amount of coherent emission with increasing frequencies. Close to the shower core the

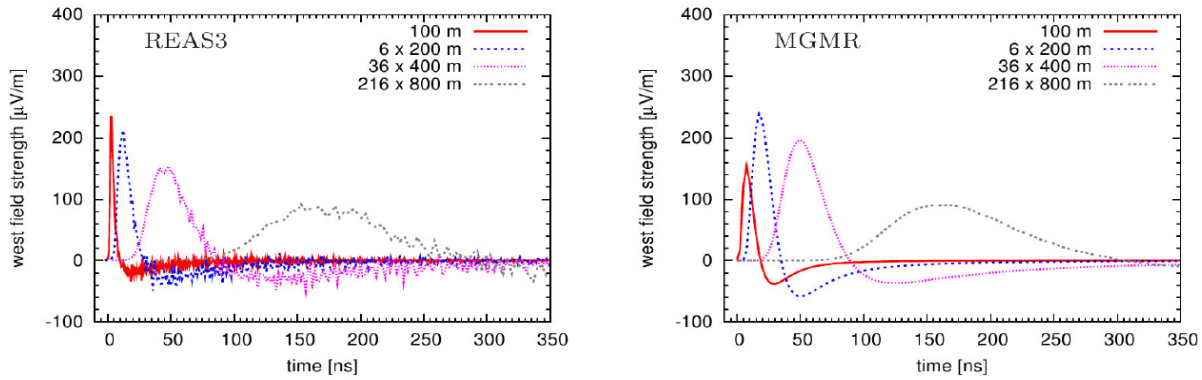

(a) **(b)**

Figure 4.5: Simulation of the radio emission from a 10^{17} eV, vertical air shower for different distances from the shower axis. Signal amplitude as function of time for a REAS3 (a) and MGMR (b) simulation. Amplitudes have been scaled for a common display. From [97].

spectrum extends up to several 100 MHz, while for larger distances the upper cut-off moves downwards and the spectrum is dominated by numerical noise from the simulation.

4.3 Polarization

A good option to disentangle the different emission mechanisms is the polarization of the radio pulse. It can be determind by using bipolar antennas, which then enable the reconstruction of the full three-dimensional electric field vector and the polarization signature.

4.3.1 Signatures

Both mechanisms, the geomagnetic and the charge-excess, induce radio signals with a linear polarization. This means that for the whole duration of the pulse the electric field vector stays constant, if the ratio of the two processes is constant in time itself. However, an observer at a fixed position will measure different signatures with respect to its positon to the shower axis.

The radiation of the geomagnetic emission process is always aligned in the direction of the Lorentz force $\vec{v} \times \vec{B}$, with $\vec{v}$ as the direction of the shower axis. This is shown in Fig. 4.7a for a vertical shower with $\vec{B}$ pointing towards North. Therefore, the polarization angle is

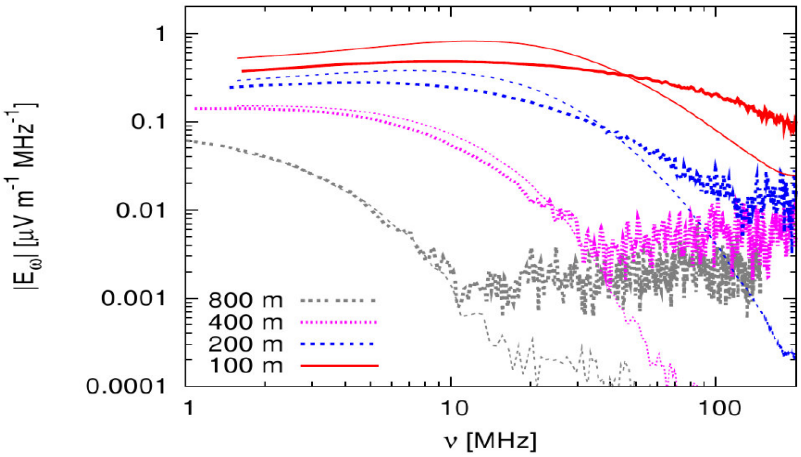

Figure 4.6: Simulation of the radio emission from a 10^{17} eV, vertical air shower for different distances from the shower axis. Spectral content of the pulses for a REAS3 (thick lines) and a MGMR (thin lines) simulation. From [97].

independent of the position of the observer. Additionally, the emission strength scales with the angle α between geomagnetic field and shower axis as $|\vec{E}| \propto \sin(\alpha)$.

The polarization for different shower directions and a pure geomagnetic emission is shown in Fig. 4.8. The length of the vector directly corresponds to the emission strength. It is clearly visbile that the maximum is found for directions perpendicular to the magnetic field and the emission strength goes to zero for parallel showers.

For the charge-excess emission the electric field is always radially polarized towards the shower axis as shown in Fig. 4.7b. This is due to the net-charge being distributed symmetrically around the shower axis. Thus, the measured polarization signature will vary with respect to the relative position of the observer to the shower axis.

We know from recent mesurements that the radiation of an air shower consists of both, geomagnetic and charge-excess emission, and so their electric fields will interfere at the observer position. As stated in [98] the superposition of two linear polarized contributions will again be polarized linearly, if they share the same time structure. The total electric field $\vec{E}(t)$ is then given by the vector sum of the individual components, depending on their strength and orientation as

$$\vec{E}(t) = \vec{E}_G(t) + \vec{E}_C(t) \tag{4.5}$$

with $\vec{E}_G(t)$ as the geomagnetic and $\vec{E}_C(t)$ as charge-excess contribution. Thus, we can define the ratio a of the charge-excess to the geomagnetic contribution corrected by the geomagnetic angle as

$$a \equiv \sin\alpha \frac{|E_C|}{|E_G|} \tag{4.6}$$

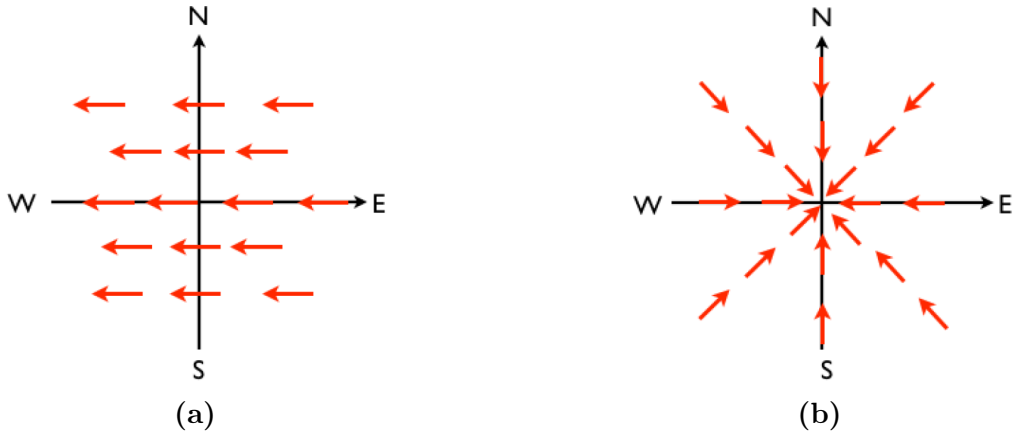

Figure 4.7: Polarization pattern at the ground level for a vertical shower in a geomagnetic field oriented along the NS axis. The shower is propagating into the paper plane and produces an uni-polar pattern for the geomagnetic mechanism (a) and a radial pattern for the charge-excess emission. From [116].

where the absolute values denote the amplitude of the electric field at the maximum of the total electric field vector. As an example, $a = 1$ for a shower with its axis orthogonal to the Earth's magnetic field means an equal contribution. A mixture leads to an asymmetry in the resulting polarization pattern. Therefore, by determining the polarization signature of the radio signal, one can achieve a good sensitiy to the emission mechanisms and their relative strengths.

This sensitivity has been shown by AERA in recent publications [118]. The dominance of the geomagnetic emission can easily be derived from the distribution of the shower arrival directions as depicted in Fig. 4.9. A clear deficite of events can be seen around the direction of the magnetic field at the Pierre Auger Observatory. The decreasing event density towards the horizon can be explained by the reduced detection efficiency for these directions due to the antenna sensitivity (c.f. Section 6.3). Additionally, a dedicated analysis has found a radial polarization component in the radio signals as expected from an Askaryan-like emission. The charge-excess fraction, i.e. the relative strength of the radial component, for a set of AERA events is shown in Fig. 4.10. Despite a large spread in the individual event measurements an average fraction of $a = 14 \pm 2\%$ was found [118].

4.3.2 Parameters

Performing this analysis requires an accurate calculation of the individual polarization contributions. To be able to do this a basic set of parameters is mandatory, which will be introduced now.

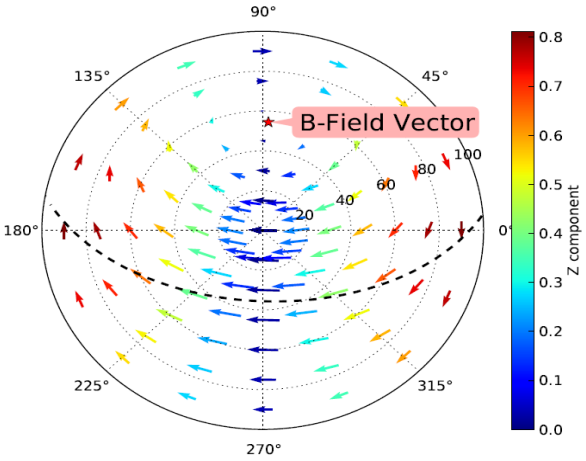

Figure 4.8: Polar skyplot of the polarization due to the geomagnetic radio emission for various arrival directions of the air shower. The vector length scales with the emission strength, the orientation indicates the horizontal component of the electric field and the vertical component is color coded. The magnetic field at the Pierre Auger Observatory is shown with the red star, the dashed line depicts the direction of maximal geomagnetic emission. From [117].

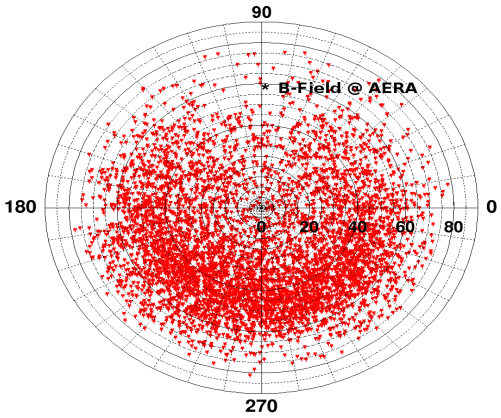

Figure 4.9: Skymap of air shower arrival directions as measured with AERA. The magnetic field at the Pierre Auger Observatory is shown with the black star. Note that the resulting distribution is a superposition of the geomagnetic emission and the varying sensitivity of the antenna with respect to the shower inclination.

For the calculation of the Stokes parameters, which we will discuss later, a complex representation of the measured time-series is needed. This can be achieved by applying a Hilbert transformation. For this purpose we perform a discrete Fourier transformation on x_l, the l-th measurement of a time-series with n ensuing measurements. This leads to the complex representation of the measurement in the frequency domain:

$$f_k = \frac{1}{\sqrt{n}} \sum_{l=1}^{n} x_l e^{-2\pi\imath kl/n}. \tag{4.7}$$

The Hilbert transformation is now obtained by shifting the phase of the complex frequencies f_k by $-\frac{\pi}{2}$ for positive frequencies with $1 \leq k < (n-1)/2$ and $+\frac{\pi}{2}$ for negative frequencies with $(n+1)/2 < k \leq n$.

$$\hat{f}_k = \begin{cases} \frac{1}{\sqrt{n}} \sum_{l=1}^{n} -\imath x_l e^{-2\pi\imath kl/n} & \text{if } k < n/2 \\ \frac{1}{\sqrt{n}} \sum_{l=1}^{n} \imath x_l e^{-2\pi\imath kl/n} & \text{if } k > n/2 \\ 0 & \text{if } k = n/2 \end{cases} \tag{4.8}$$

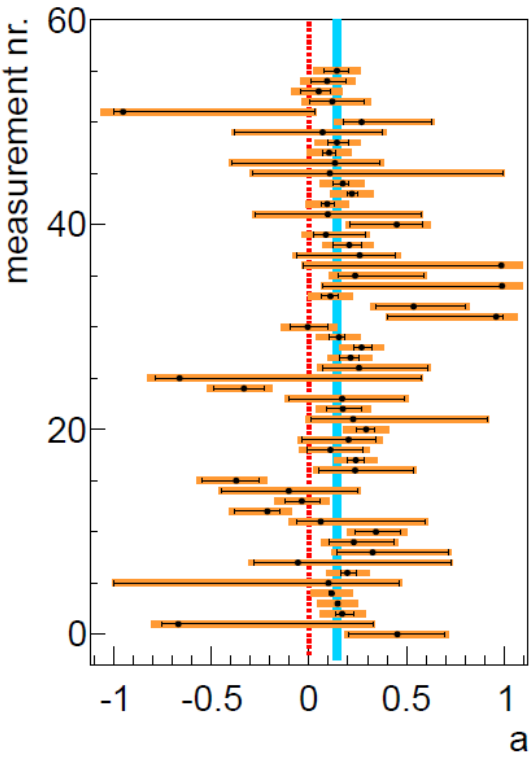

Figure 4.10: Distribution of the most probable value of the charge-excess fraction a for a set of AERA events. The solid blue line indicates the 68% confidence belt around the determined mean value of $a = 0.14 \pm 0.02$. Error bars denote the 68% uncertainty of the most probable value. From [118].

$\hat{f}_k$ now is the Hilbert transformed frequency spectrum, which can be re-converted to the Hilbert transform of the time sample m by applying the inverse Fourier transformation. After applying some simplifications this can be written as

$$\hat{x}_m = \frac{2}{n} \sum_{k=1}^{n/2} \sum_{l=1}^{n} x_l \sin\left(\frac{2\pi k(m-l)}{n}\right). \tag{4.9}$$

This transformation can be used to calculate an envelope on a bandpass limited time-series. The envelope $\tilde{\vec{x}}$ of a time-series $\vec{x}$ is given by

$$\tilde{x}_i = \sqrt{x_i^2 + \hat{x}_i^2}. \tag{4.10}$$

This procedure is applied during the data reconstruction of AERA to derive specific signal related quantities. An example trace showing both time-series and the calculated envelope can be found in Fig. 4.11.

The polarization signature of the radio emission from air showers can be parametrized by the Stokes parameters, which originate from classical radio astronomy. They have the

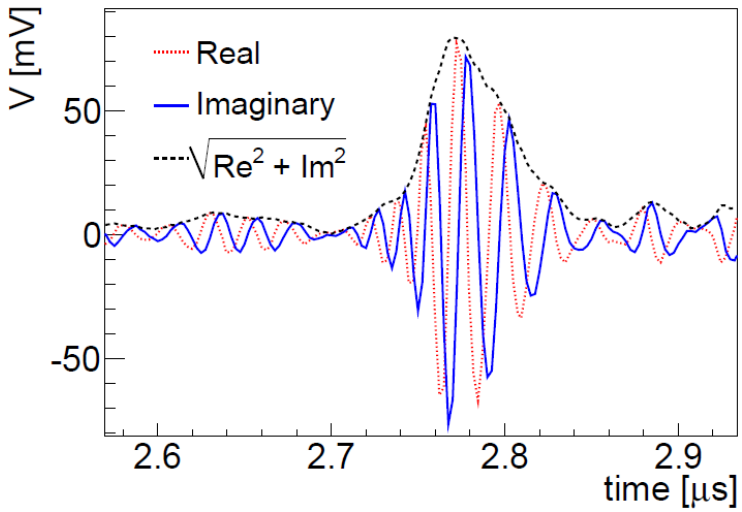

Figure 4.11: Example of a real time-series, the Hilbert transformed imaginary propagation and the calculated envelope. From [98].

advantage that they can describe completly polarized as well as partially or non-polarized signals. However, they can only be obtained if two perpendicular channels are available. In the horizontal plane they are defined as

$$S_0 \equiv \frac{1}{n}\sum_{i=1}^{n}(x_i^2 + \hat{x}_i^2 + y_i^2 + \hat{y}_i^2), \tag{4.11}$$

$$S_1 \equiv \frac{1}{n}\sum_{i=1}^{n}(x_i^2 + \hat{x}_i^2 - y_i^2 - \hat{y}_i^2), \tag{4.12}$$

$$S_2 \equiv \frac{2}{n}\sum_{i=1}^{n}(x_i y_i + \hat{x}_i \hat{y}_i), \tag{4.13}$$

$$S_3 \equiv \frac{2}{n}\sum_{i=1}^{n}(\hat{x}_i y_i + x_i \hat{y}_i), \tag{4.14}$$

with the time-series $\vec{x}$ of the East-West component and $\vec{y}$ of the North-South component and their corresponding complex propagations $\hat{x}_i$ and $\hat{y}_i$ obtained by Eq. 4.9. Each parameter hereby has a specific meaning: S_0 yields the total intesity of the signal, S_1 and S_2 gives the linear components and S_3 the circular component of the polarization.

The so-called Poincaré sphere as depicted in Fig. 4.12 allows a good way to visualize the Stokes vector

$$\vec{S} = \begin{pmatrix} S_1 \\ S_2 \\ S_3 \end{pmatrix}. \tag{4.15}$$

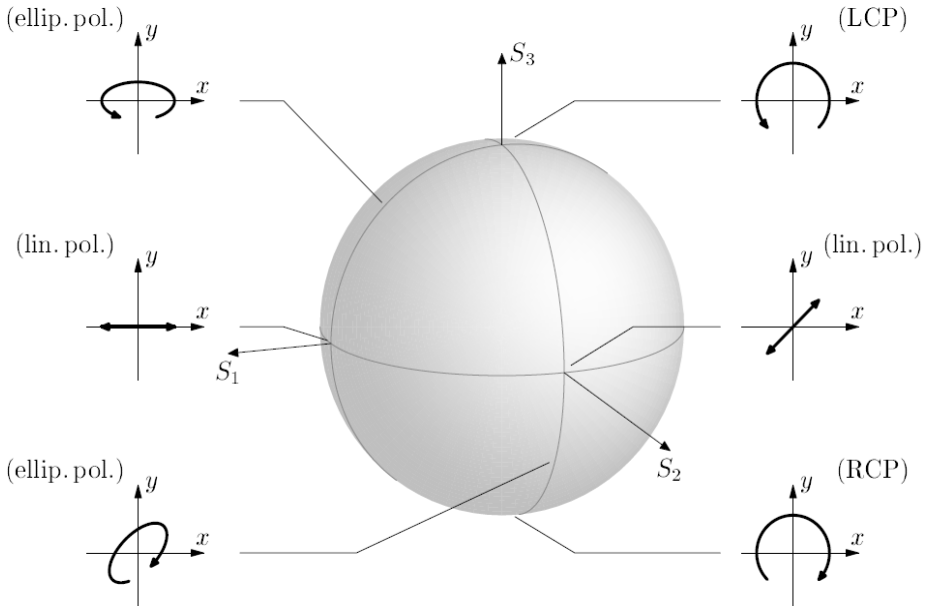

Figure 4.12: The Poincaré sphere, on which the Stokes vector $\vec{S} = (S_1, S_2, S_3)$ provides a representation of the polarization state of the signal. The small figures show the paths traversed by the end point of the electric field vector as the observer looks into the oncoming wave, propagating in the positive z-direction. LCP / RCP denotes left / right circular polarization. From [119].

If the signal is completly polarized $\vec{S}$ can be found on the surface of the sphere, within the sphere for partial polarization, and in the center if not polarized at all. The fraction of the signal power in the polarized component is defined as the degree of polarization

$$p = \frac{\sqrt{S_1^2 + S_2^2 + S_3^2}}{S_0} \tag{4.16}$$

with $0 \leq p \leq 1$. All fully linear polarizations are located on the equator ($S_3 = 0$), their orientations are determined by the meridian. Complete circular polarization is found at the upper and lower pole ($S_1 = S_2 = 0$) and the ellipticity of the polarization in between is defined by the latitude.

For a physical interpretation of the Stokes parameters their uncertainties have to be known. They can be obtained using standard error propagation:

$$\begin{aligned}\sigma_{S_k}^2 = \sum_{i=1}^{n}\sum_{j=1}^{n}\Bigg(&\frac{\partial S_k}{\partial x_i}\frac{\partial S_k}{\partial x_j}\mathrm{Cov}(x_i, x_j) + \frac{\partial S_k}{\partial y_i}\frac{\partial S_k}{\partial y_j}\mathrm{Cov}(y_i, y_j) \\ &+ \frac{\partial S_k}{\partial x_i}\frac{\partial S_k}{\partial y_j}\mathrm{Cov}(x_i, y_j) + \frac{\partial S_k}{\partial x_j}\frac{\partial S_k}{\partial y_i}\mathrm{Cov}(x_j, y_i)\Bigg)\end{aligned} \tag{4.17}$$

The resulting uncertainties are

$$\sigma^2_{S_0} = \frac{16}{n^2}\sum_{i=1}^{n}\sum_{j=1}^{n}(x_i x_j \mathrm{Cov}(x_i,x_j) + y_i y_j \mathrm{Cov}(y_i,y_j) + x_i y_j \mathrm{Cov}(x_i,y_j) + x_j y_i \mathrm{Cov}(x_j,y_i)) \tag{4.18}$$

$$\sigma^2_{S_1} = \frac{16}{n^2}\sum_{i=1}^{n}\sum_{j=1}^{n}(x_i x_j \mathrm{Cov}(x_i,x_j) + y_i y_j \mathrm{Cov}(y_i,y_j) - x_i y_j \mathrm{Cov}(x_i,y_j) - x_j y_i \mathrm{Cov}(x_j,y_i)) \tag{4.19}$$

$$\sigma^2_{S_2} = \frac{16}{n^2}\sum_{i=1}^{n}\sum_{j=1}^{n}(y_i y_j \mathrm{Cov}(x_i,x_j) + x_i x_j \mathrm{Cov}(y_i,y_j) + x_j y_i \mathrm{Cov}(x_i,y_j) + x_i y_j \mathrm{Cov}(x_j,y_i)) \tag{4.20}$$

$$\sigma^2_{S_3} = \frac{16}{n^2}\sum_{i=1}^{n}\sum_{j=1}^{n}(\hat{y}_i \hat{y}_j \mathrm{Cov}(x_i,x_j) + \hat{x}_i \hat{x}_j \mathrm{Cov}(y_i,y_j) - \hat{x}_i \hat{y}_j \mathrm{Cov}(x_i,y_j) + \hat{x}_j \hat{y}_i \mathrm{Cov}(x_j,y_i))\,. \tag{4.21}$$

Moreover, due to the inevitable presence of noise in the measurements an additional bias can be introduced to the parameters. We consider a time sample $x_i = s_{x_i} + b_{x_i}$, which consists out of a signal $\vec{s}$ and a noise $\vec{b}$ component. This leads to

$$\sum_{i=1}^{N} x_i^2 = \sum_{i=1}^{N}(s_{x_i}^2 + b_{x_i}^2 + 2 s_{x_i} b_{x_i}) \approx \sum_{i=1}^{N}(s_{x_i}^2 + b_{x_i}^2), \tag{4.22}$$

which holds, if the phases between signal and noise are uncorrelated and so the remaining bias is $\sum_{i=1}^{N} b_{x_i}^2$. This can be corrected for by calculating the mean bias $\bar{b}_x^2$ inside a noise window and subtracting it from the signal as

$$\sum_{i=1}^{N} s_i^2 \approx \sum_{i=1}^{N}(x_{x_i}^2 - \bar{b}_x^2). \tag{4.23}$$

Applying this correction to S_0 and S_1 results in:

$$S_0 \approx \frac{1}{n}\sum_{i=1}^{n}(x_i^2 + \hat{x}_i^2 + y_i^2 + \hat{y}_i^2 - \bar{b}_x^2 - \bar{b}_{\hat{x}}^2 - \bar{b}_y^2 - \bar{b}_{\hat{y}}^2) \tag{4.24}$$

$$S_1 \approx \frac{1}{n}\sum_{i=1}^{n}(x_i^2 + \hat{x}_i^2 - y_i^2 - \hat{y}_i^2 - \bar{b}_x^2 - \bar{b}_{\hat{x}}^2 + \bar{b}_y^2 + \bar{b}_{\hat{y}}^2). \tag{4.25}$$

While S_0 always needs correction, the noise contributions in S_1 will cancel out, if the noise levels in $\vec{x}$ and $\vec{y}$ are comparable. Regarding the cross terms one finds,

$$\sum_{i=1}^{N} x_i y_i = \sum_{i=1}^{N}((s_{x_i} + b_{x_i})(s_{y_i} + b_{y_i})) \approx \sum_{i=1}^{N} s_{x_i} s_{y_i}, \tag{4.26}$$

which is valid, if the phases of the noise in both channels and the phase and signal of opposing channels are uncorrelated. Thus, no bias is expected for S_2 and S_3 as they only consist of those cross terms.

One last parameter will be introduced to further quantify the polarization signature. The angle of polarization ψ_p is defined as the angle between the semi-major axis of the polarization ellipse and the x-axis. It can be written as

$$\psi_p = \frac{1}{2}\tan^{-1}(S_2/S_1). \tag{4.27}$$

Also here the uncertainty on ψ_p can be determined from standard error propagation, which simplies due to the fact that S_1 and S_2 are assumed to be uncorrelated to

$$\begin{aligned}\sigma_{\psi_p} &= \sqrt{\left(\frac{\partial\psi_p}{\partial S_1}\sigma_{S_1}\right)^2 + \left(\frac{\partial\psi_p}{\partial S_2}\sigma_{S_2}\right)^2} \\ &= \sqrt{\frac{(\sigma_{S_1}^2 S_2^2 + \sigma_{S_2}^2 S_1^2)}{4(S_2^2+S_1^2)}}.\end{aligned} \tag{4.28}$$

The full calculations and validation tests for both, uncertainties and bias, can be found in [98]. The analysis of the radio emission polarization performed later in Section 9.5 takes this bias estimation of the Stokes parameters into account and also their uncertainties are calculated as presented above.

4.4 Lateral distribution function and radio energy

The lateral distribution function of the radio signal has been studied by several experiments in the recent past. LOPES [120] as well as CODALEMA [121] both measured an exponential fall-off as already reported by Allan in the 1970s (c.f. Eq. 4.1) with a slope parameter of $R_0 \approx 150 \pm 50$ m. In addition, LOPES reported the observation of a significant flattening of the LDF towards the core for about 20% of the events [120]. This is a result of an effect due to the index of refraction, n, which is varying throughout the atmosphere. Air shower simulations using a realistic refractive index have reproduced events with a flat profile as a consequence of a Cherenkov ring [109]. Figure 4.13 shows the LDF of an example event measured with AERA. Also here the flattening or even a drop off towards the shower axis can be observed. Furthermore, CODALEMA found a systematic shift of the radio core with respect to the particle core. A good representation of this feature could be generated when considering a charge-excess contribution in the simulations [122]. This azimuthal invariance makes the use of purely one-dimensional LDFs, especially close the shower axis, inappropriate.

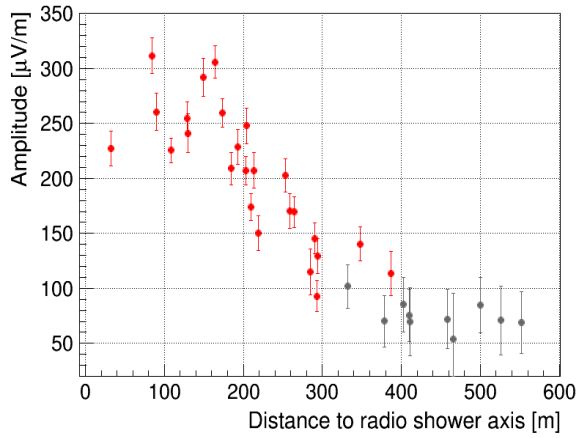

Figure 4.13: One-dimensional LDF for an air shower ($\theta = 54°$, $\phi = 315°$, $E = 5.1 \times 10^{17}$ eV) measured with AERA showing the amplitude versus the distance to the RD shower axis. Detector stations above min. SNR in red, sub-threshold in gray.

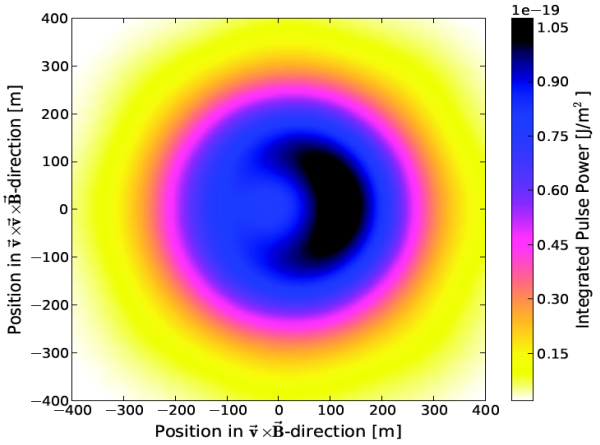

Figure 4.14: Interpolated two-dimensional pattern of the total pulse power in the shower plane for a simulated air shower ($\theta = 45°$, $\phi = 37°$, $E = 4.4 \times 10^{16}$ eV) showing the typical bean-shape pattern. From [82].

Recent measurements by LOFAR, which is well-suited for this analysis due to its extremely dense antenna grid, have confirmed both effects. These findings have been merged into a two-dimensional LDF function composed of two Gaussian distributions, which shows a good agreement for LOFAR as well as for AERA data [82]. The general parametrization for the pulse power is given by

$$P(x', y') = A_+ \cdot \exp\left(\frac{-[(x' - X_+)^2 + (y' - Y_+)^2]}{\sigma_+^2}\right) - A_- \cdot \exp\left(\frac{-[(x' - X_-)^2 + (y' - Y_-)^2]}{\sigma_-^2}\right) \tag{4.29}$$

with x' and y' as the coordinates in the shower plane, aligned with the $\vec{v}\times\vec{B}$- and $\vec{v}\times(\vec{v}\times\vec{B})$-axis. Here, the larger Gaussian describes the general property of the radio emission, while the smaller one combined with a shifting accounts for the flattening of the signal and the asymmetry due to the different emission processes resulting in a bean-shaped pattern. An example of an interpolated event simulation is shown in Fig. 4.14. However, this general form, although well fitting for LOFAR, was modified for AERA due to the lower station multiplicity to

$$P(x', y') = A_+ \cdot \exp\left(\frac{-[(x' - X_c)^2 + (y' - Y_c)^2]}{\sigma_+^2}\right) - C_0 \cdot A_- \cdot \exp\left(\frac{-[(x' - (X_c - C_3))^2 + (y' - Y_c)^2]}{(e^{C_1 + C_2 \cdot \sigma_+})^2}\right) \tag{4.30}$$

zenith range	C_3
$0 - 10°$	32.3 ± 0.7
$10 - 20°$	36.3 ± 0.8
$20 - 30°$	40.8 ± 0.5
$30 - 40°$	56.9 ± 0.8
$40 - 50°$	73.1 ± 1.4
$50 - 60°$	61.9 ± 1.9

Table 4.1: Values for the constant fit parameter C_3 for different zenith ranges. From [82].

with the free parameters A_+, X_c, Y_c and σ_+ and constants $C_0 = 0.41$, $C_1 = 2.788$ and $C_2 = 0.0079$. C_3 was found to be zenith dependent, but can be fixed for a set of angular ranges. The actual values are denoted in Tab. 4.1. However, if enough stations are present in the reconstructed event also C_3 can be added to the fit procedure.

A benefit from this parametrization is the direct access to the amount of energy which is transfered from the air shower into the radio emission by integration over the whole shower plane

$$S_{\text{radio}} = \frac{1}{\sin(\alpha)} \int P(x', y') dx' dy'. \tag{4.31}$$

The $\sin(\alpha)$ term is to account for different emission strengths at different angles between shower axis and magnetic field. This formula has been applied to AERA data and plotting the energy estimator versus the energy measured with the surface detector of the Pierre Auger Observatory yields a clear correlation [123]. Using a likelihood function the calibration function

$$S_{\text{radio}} = A \times \left(\frac{E_{\text{SD}}}{10^{18}\text{eV}} \right)^B \times 10^7\text{eV} \tag{4.32}$$

could be determined with $A = 1.569 \pm 0.071$ and $B = 1.975 \pm 0.040$. This implies that the deposited radiation energy increases quadratically with the air shower energy as expected from coherent emission (c.f. Section 4.1).

Further dependencies of the LDF parameters, like a sensitivity to the distance to the shower maximum, have been proven using simulations, but have yet to be shown for measured data.

4.5 Atmospheric electric fields

For a full understanding of measured data a detailed knowledge of the instrument used for the detection is mandatory. In case of a man-made detector this can be achieved more or

less easily by lab measurements of the individual components and their influence on the signal chain (c.f. Section 7.4). However, for air shower experiments the initial detector volume is the atmosphere itself, which can influence the shower development in multiple ways.

While surface detectors are only slightly affected by its density [124], especially detectors using the optical technique suffer a lot from atmospheric conditions. For example, aerosols, clouds or dust layers have a significant impact on the propagation of the emitted fluorescence light and thus, the detectable amount at the detector site. This manifests the need for atmospheric monitoring systems like cloud cameras or laser systems as operated e.g. by the Pierre Auger Observatory.

Concerning the radio detection of air showers its big advantage is that it is not attenuated in the atmosphere. But a new atmospheric component comes into play, which is the atmospheric electric field. Only few years after the first predictions of the radio emission, Charman came up with calculations for a significant contribution due to charge separation in the electric field [100] and due to the acceleration of ionization electrons [125, 126]. The group of Mandolesi was the first to report experimental evidence of overly large pulses in the radio regime during thunderstorms in 1971 [127].

The most challenging part in this approach is for sure the parametrization of the highly complex structure of atmospheric electric fields, which is needed for a detailed understanding of their influences during the development of the air shower. In normal, fair weather conditions the static electric field changes only slowly with values up to ~ -100 V/m on ground level, decreasing rapidly with increasing altitude. Normal clouds, charged up by fair weather currents or particle collisions, can have field strengths of several hundred V/m, while Nimbostratus clouds can reach 10 kV/m. The electric fields inside thunderclouds with an extend of several kilometers can be even stronger by one order of magnitude.

While the field is mostly aligned vertical in normal clouds, thunderclouds also yield a non-trivial structure of field directions due to the chaotic distributions of charges. They can be formed under strongly convective meteorological conditions. Stolzenburg et al. performed a series of balloon soundings in convective regions of mesoscale (2 - 2000 km) thunderstorm systems [128]. They found two systems of charge structures, which can describe most of their measurements. For soundings in the updraft region, i.e. the average ascent rate is larger than the mean vertical velocity of the balloon, the electric field profile shows three dominant peaks with changing polarity. A lower positive peak of 30 to 110 kV/m near 5 km, a midlevel negative peak of -45 to -120 kV/m near 8 km and an upper positive peak of 30 to 50 kV/m near 11 km. Additionally, multiple rapid field changes, which can be accounted to lightnings, were found in between heights of 6 to 10 km. Outside the updraft regions the profile shows up to six different charge regions with the lowest being again of positive polarity at approximately 3 km followed by a negative region near 4 km. In general the maximum field amplitude for both polarities was found to be larger and located at

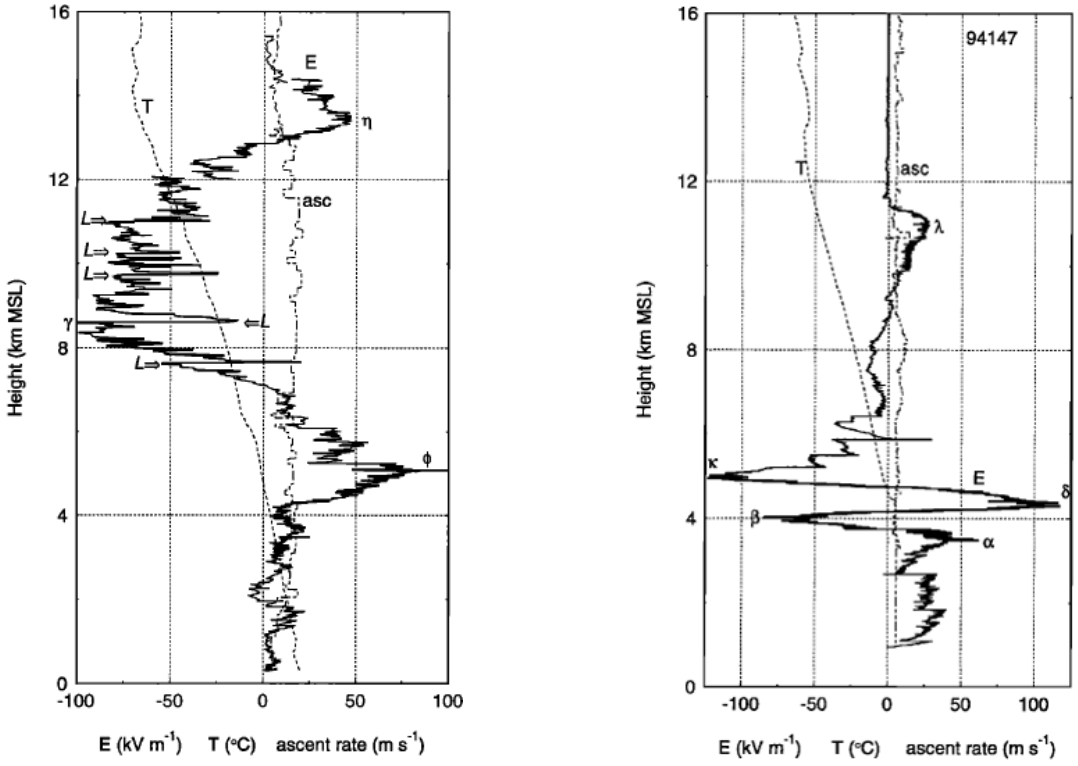

Figure 4.15: Balloon soundings of the electrical structure in a thunderstorm convective region. Plotted are electric field (E) as well as temperature (T) and ascent rate (asc) versus height for a measurement in the updraft region (a) and in the non-updraft region (b). Regions of maximal field strength are marked with greek labels, lightning-related field changes are marked with L. From [128].

lower heights for these measurements. Also the difference in altitude for a change from the maximum electric field of one polarity to the other is lower [128]. The measurements for two balloon soundings, one inside and one outside the updraft, are shown in Fig. 4.15.

While balloon measurements are appropriate for special cloud studies, continuous field measurements can only be performed on the ground. Figure 4.16 exhibits the measurement of the atmospheric electric field on ground level as performed with two weather stations at the Pierre Auger Observatory during four days of normal conditions as well as four hours of thunderstorm conditions. The field in the normal days shows a rather smooth development with only day-night variations in the range of 0 V/m to -60 V/m, while the thunderstorm period yields huge field strengths of both polarities up to $\pm$ 5 kV/m, changing on rather short timescales. Also depicted are some flags, which have been introduced in the context of LOPES to identifiy conditions by an analytical approach to the electric field development like threshold crossings and slopes. Further details can be found in [129].

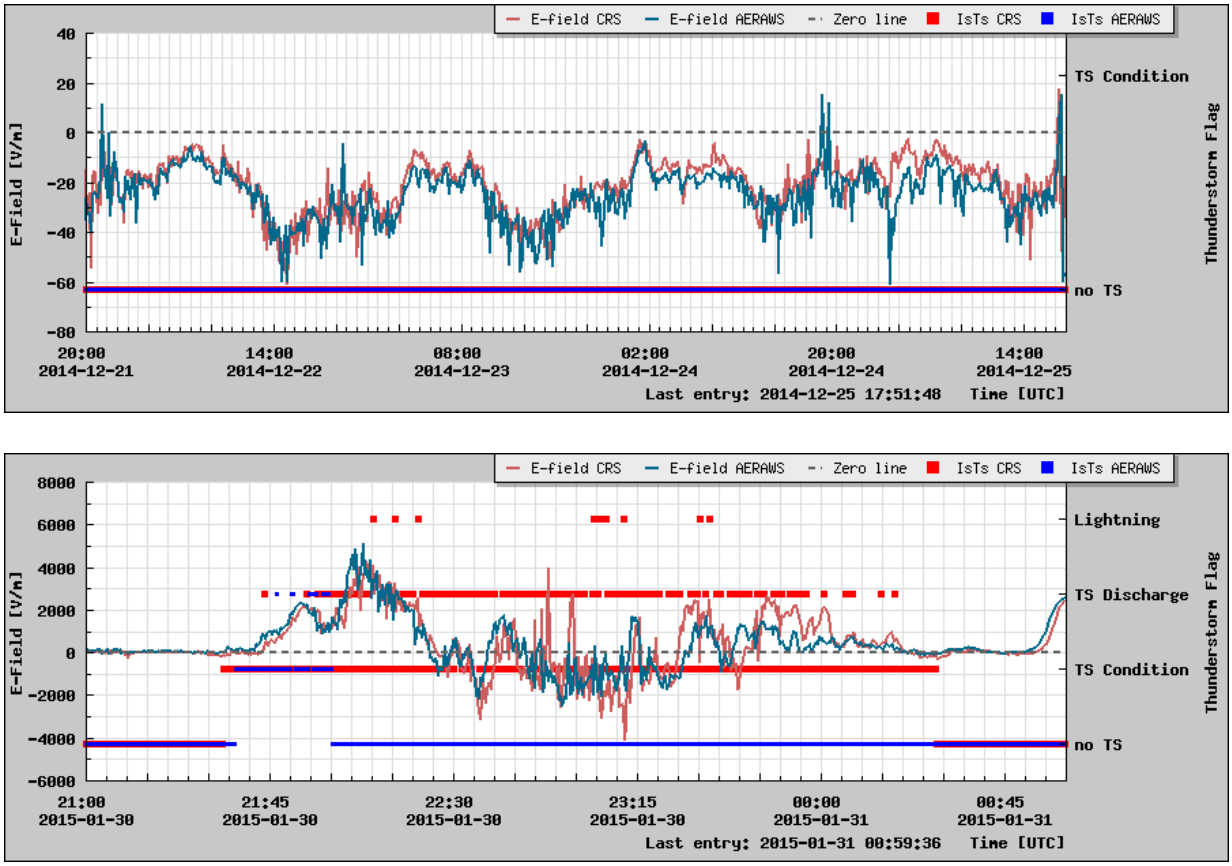

Figure 4.16: The atmospheric electric field on ground level as measured with the weather stations at the Pierre Auger Observatory for four days of fair weather conditions (top) and four hours during thunderstorm conditions (bottom). In addition, some flags deduced from the development of the electric field to classify specific conditions are indicated.

Although it is heavily influenced by the processes in the higher atmosphere, there is yet no reliable way to estimate field strength of clouds by measurements on ground level. However, there are several approaches, which can be used to at least gather a rough estimate of the present field strength. Multiple measurements at large distances to each other (several km) can be used to gain an analytical description of the spatial field structure on ground level. With this pattern a determination of the charge distribution inside the cloud is possible. Another method uses numerical models of the shape of the radio frequency emission for a remote estimation of the electric fields in the emission region [130].

The atmospheric electric field can have an impact on the radio emission in multiple ways. First, as already mentioned in Section 4.1, the electric field can accelerate the electrons and positrons just like the Earth's magnetic field does. This leads to a change of the radio emission depending on the orientation of the field, but should not change the width of the pulse though. Figure 4.17 shows some possible geometries for this model. Without a

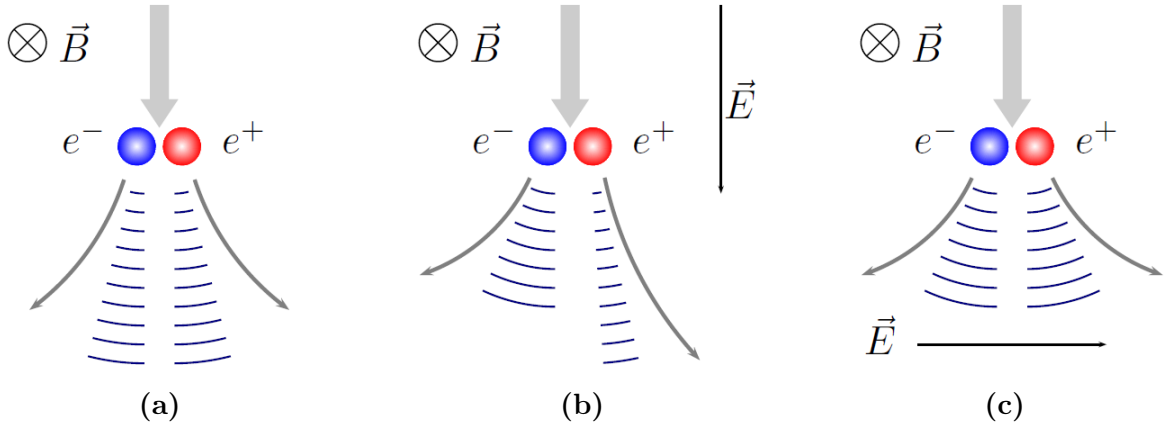

Figure 4.17: Schematic view of the change in the particle trajectory due to additional electric fields and the resulting difference in the radio emission. Standard geometry for no electric field (a), asymmetric trajectories for a parallel electric field (b) and amplified emission for a perpendicular electric field (c). From [131].

(sufficiently strong) electric field the particles will just emit synchrotron radiation. If the additional electric field is aligned parallel to the shower, it will accelerate one particle type and decelerate the other with respect to its orientation, which leads to an asymmetry in the trajectory. Finally, for a perpendicular electric field the electric force can act either in the same or in the opposite direction as the Lorentz force for both types, which results in an amplification or attenuation of the emission correspondingly. The radio emission from this mechanism is of the same order of magnitude as the radiation from the geomagnetic process for fields of roughly 100 V/cm.

The second mechanism uses the free electrons resulting from the ionization of molecules, when an air shower traverses the atmosphere. If they do not recombine immediately, these electrons are accelerated by the electric field and can therefore produce a current pulse with a length of the order of 100 ns. Since the free electrons do not reach relativistic velocities under normal conditions this radiation is not beamed forward and only coherent up to ca. 10 MHz. However, these electrons will not only produce a large numer of slow thermal electrons, but can also ionize new air molecues. This requires the presence of a strong electric field, which is able to accelerate them to an energy of $E_c \approx 0.1 - 1$ MeV to overcome the loses of frictional scattering as shown in Fig. 4.18. [132]. The field strength necessary for this effect to start is

This is the critical energy for the so-called runaway breakdown, an electron avalance process, introduced by Gurevich et al.

$$\varepsilon_c \approx 200 \text{ kV/m} \left(\frac{N_m(z)}{N_m(0)} \right), \tag{4.33}$$

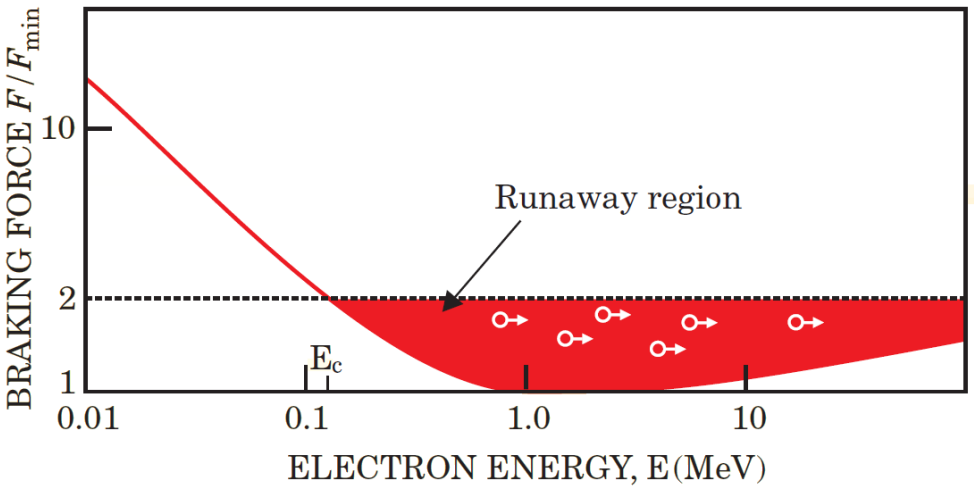

Figure 4.18: Braking force F acting on an electron transversing matter as a function of particle energy E. The red shaded area is the region, where runaway breakdown can occur. Modified from [133].

with $N_m(z)$ as the neutral molecule density at height z and $N_m(0) = 2.7 \times 10^{19}$ cm^3 at sea level. For typical thunderclouds at a height between 4 - 6 km, this results in $\varepsilon_c \approx 100 - 150$ kV/m, which is an often measured value during thunderstorms. Figure 4.19 shows the measurement of the vertical electric field of four different thunderclouds. It is clearly visible that lightning flashes often occur when the electric field reaches ε_c. The full radiation pattern of this emission has been calculated and is similar to the one from a current pulse, but with an amplitude that is several orders of magnitude larger than the geomagnetic emission [134].

In addition, the atmospheric electric field has also an influence on the total electromagnetic cascade. If present in equal numbers, the energy gained or lost by electrons and postitrons would be in equilibrium. However, if a charge excess is present, which is known to be the case, this will result in an energy variation of the whole shower. This effect is estimated to be on the order of a few percent of the total shower energy [135]. Furthermore, the electric field can have an impact on the general shower development as it acts on all charged particles.

Also the phenomenon of lightnings is strongly correlated with the atmospheric electric field and has been thoroughly studied in this context. The conventional breakdown theory is similar to the idea of the runaway breakdown. However, here the free electrons are not the high-energetic air shower secondaries, but originate from the tail of the thermal distribution function resulting in a mean particle energy of only 1 - 10 eV. This amount is still sufficient to ionize matter and generate new electrons, but would require a breakdown field of $\varepsilon \approx 2$ MV/m in large spatial extend. Fields of this magnitude have not been

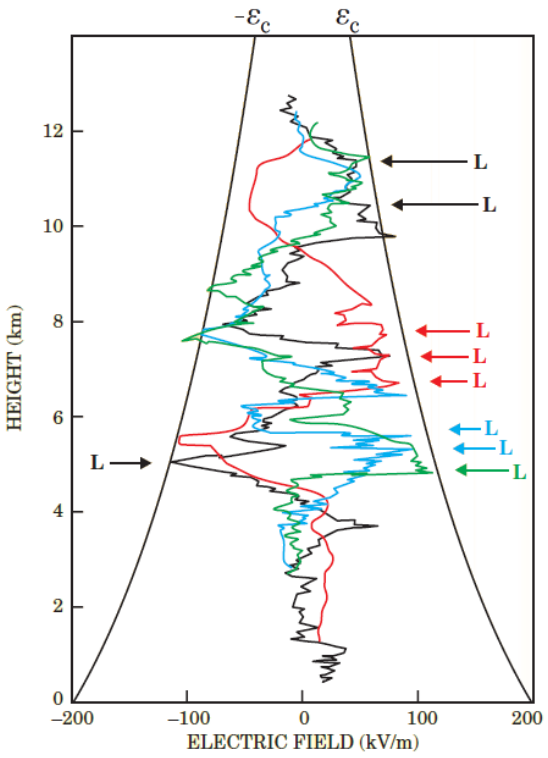

Figure 4.19: Four balloon soundings of the vertical electric field in thunderclouds as function of height. The critical energy for a runaway breakdown ε_c is indicated with the solid black lines, lightning-related field changes are marked with L. Modified from [133].

measured yet even in thunderclouds, which enforces the runaway breakdown theory even more as possible explanation for the initiation of lightnings. In that case, an observer could measure a follow-up emission to the air shower signal caused by electrical processes inside the thunderstorm and finally a discharge signature [101].

CHAPTER 5

The Pierre Auger Observatory

The Pierre Auger Observatory, located in the Pampa Amarilla near the town of Malargüe in the province Mendoza, Argentina (c.f. Fig. 5.1a), is currently the largest detection system for UHECR worldwide. Built as a hybrid detector it is designed to study cosmic rays via the observation of air showers at the highest energies ($E \geq 10^{18}$ eV). A schematic overview of the array is shown in Fig. 5.1b.

The baseline design consists of the Fluorescence Detector (FD) and the Surface Detector (SD), which are discussed in more detail in Section 5.1. These two detector types observe the same shower and can therefore help to study systematic effects for each type as well as enhance the resolution for the important air shower parameters like energy, arrival direction and composition. First data taking started in 2004 with several hundreds of detectors while the full array was completed with a ceremonial inauguration in November 2008. Using the environment of these well established techniques a lot of enhancements like the low-energy extensions AMIGA and HEAT (see Section 5.2) or the radio extension AERA (see Chapter 6) have been deployed and thoroughly tested in the last years. Today, the Auger Collaboration consists of around 500 scientists from more than 60 institutions around the world.

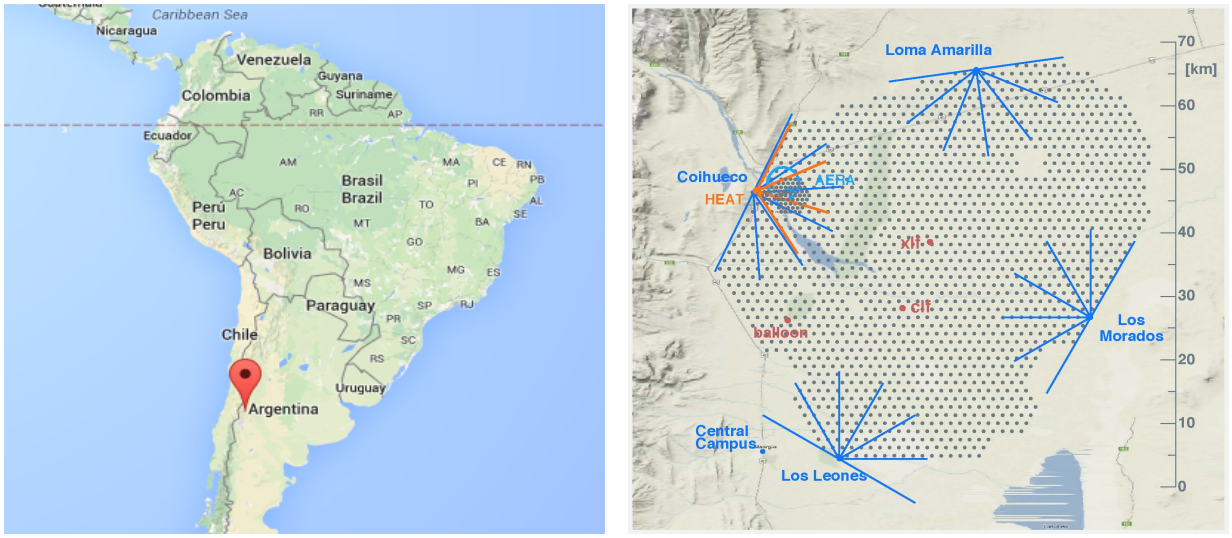

(a) (b)

Figure 5.1: Location of the Pierre Auger Observatory near Malargüe, Mendoza in Argentina (a) and overview of the Pierre Auger Observatory (b). Each dot indicates the position of a water-Cherenkov detector, the Fluorescence telescopes and their field of view are represented by the solid blue lines. Additionally, the extension HEAT (orange lines), the position of AERA as well as the facilities for atmospheric monitoring BLS ('balloon'), CLF and XLF are shown.

5.1 Baseline detectors

A key feature of the Pierre Auger Observatory is its hybrid design, enabling simultaneous air shower observation by two complementary techniques, particle and optical detection, and taking advantage of the capabilities of both types.

5.1.1 The Surface Detector

The Surface Detector is a ground array of 1660 water-Cherenkov detectors covering an area of about 3000 km^2. The stations are deployed in a hexagonal grid with a spacing of 1.5 km, which leads to a full detection efficiency for air showers with an energy above $E = 3 \times 10^{18}$ eV.

Each individual surface detector station (SDS) consists of a water-proof tank filled with 12 m^3 purified water inside a Tyvek bag. The Cherenkov radiation, which is emitted by particles traversing the water of the detector, is measured by three semi-hemispheric photo-multiplier tubes (PMTs). They are read out with a flash analog-to-digital converter

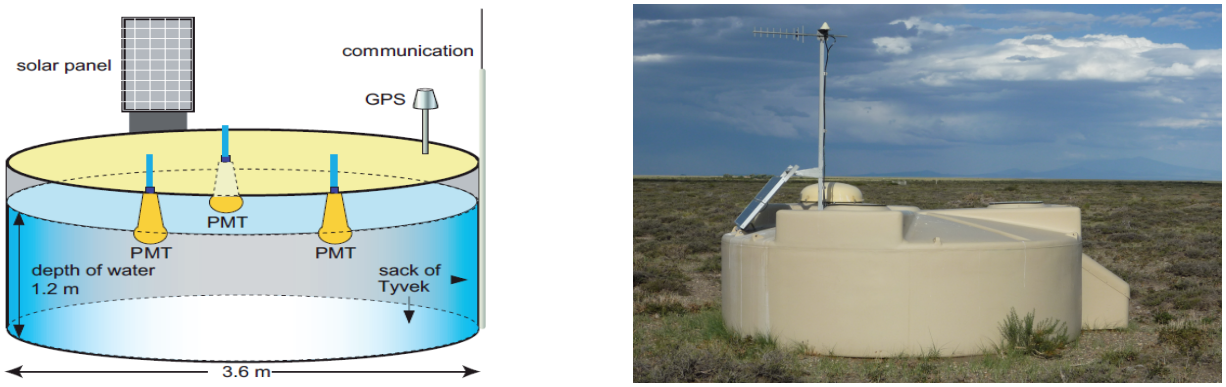

(a) (b)

Figure 5.2: Schematic drawing of a Surface Detector Station (SDS) with its most important individual components [136] (a) and picture of a SDS within the Argentinean pampa (b).

running on 40 MHz. A GPS clock is used for an absolute station timing accuracy of about 10 ns. Figure 5.2a shows a schematic drawing of a SDS.

Several trigger algorithms are used to provide a local station trigger, which is then sent to the central data-acquisition system (CDAS). If a coincidence of at least three stations is found, the full station data are transfered, merged and written to disk. Each detector is equipped with a solar panel and a battery providing a fully autonomous power supply.

The average angular resolution of the SD for zenith angles up to 55° is approximately 2° for an event measured with 3 SDS and well below 1° for 6 or more SDS [137]. The uncertainty on the core position is on the level of 50 m for well reconstructed events. The SD provides an uptime of 100% only reduced by failures of the communication system. An image of a deployed SDS in the Argentinean pampa can be seen in Fig. 5.2b.

The reconstruction of data is done in a two step procedure (c.f. [138]). First, an initial fit of the shower direction and the core position is performed using the arrival times of the measured signals in the individual stations. This is followed by a more detailed determination of the lateral signal distribution with a modified NKG-function (c.f. Section 3.1):

$$S(r) = S_{1000} \cdot \left(\frac{r}{r_{1000}}\right)^{\beta} \cdot \left(\frac{r + r_{700}}{r_{1700}}\right)^{\beta+\gamma} \tag{5.1}$$

Here, $S(r)$ gives the measured signal in VEM with respect to the distance to the shower core. The position of the shower core and S_{1000} are the free fit parameters, whereas β and γ are only fitted if a sufficient number of stations were triggered ($\beta_{\text{init}} = 0.9\,\sec(\theta) - 3.3$, $\gamma_{\text{init}} = 0$). S_{1000} is the signal at 1000 m distance from the shower axis. At this point the systematic effect of the primary particle on the LDF shape is minimal and therefore, this quantity can be used as energy estimator with $E = a(\theta) \cdot (S_{1000})^{b(\theta)}$. It has been cross-calibrated with

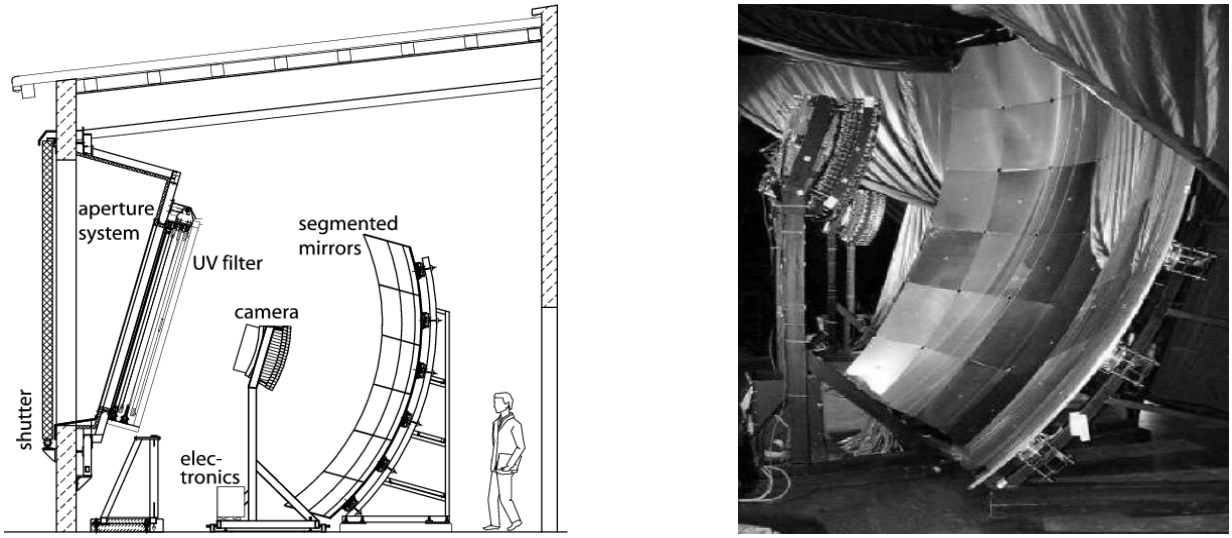

(a) **(b)**

Figure 5.3: Schematic drawing of a Fluorescence Detector inside the telescope building (a) and picture of a camera system and spherical mirror (b). From [139].

the calorimetric data from the Fluorescence Detector as a determination of the absolute energy scale is difficult for sole SD measurements due to the dependence on the simulation of the hadronic interactions in the shower development.

5.1.2 The Fluorescence Detector

The Fluorescence Detector (FD) consists of 24+3 Schmidt telescopes located at four detection sites at the perimeter around the SD array to ensure a complete coverage of the atmosphere above the observatory. The six telescopes, each covering a field of view of 30° × 30°, at one site form an "eye" of the FD.

Figure5.3a displays a schematic drawing of a fluoresence telescope. After passing a corrector optic and a filter the incoming light, which was emitted by the de-excitation of nitrogen molecules, is focused by a 3.5 × 3.5 m^2 spherical mirror onto a camera built up out of 440 PMTs, each one a so-called "pixel". The recorded signals are digitized with a sampling rate of 10 MHz. Afterwards a trigger decision is formed by a hierarchical structure of air shower signal patterns and sent to the CDAS. This triggers a raed-out even of single SDS based on the FD information.

In the FD reconstruction the shower axis is determined by the pointing directions of the triggered pixels and their timing information. In addition, the information from the SDS with the highest signal, the "hottest station" is used, to confine the shower geometry

even further. As the detection of the fluorescence light is a calorimetric measurement, an integration over the longitudinal profile, the Gaisser-Hillas function (see Section 3.1), yields a good estimate of the deposited shower energy with a systematic uncertainty of $\sim 20\%$. Also the position of the shower maximum, which is used for composition studies, can be reconstructed from the profile, yielding a resolution of ~ 20 g/cm^2 [140].

The FD reaches full detection efficiency at energies of about $E \sim 10^{18}$ eV. However, due to moonlight, clouds and other non-defined atmospheric conditions the detector uptime is limited to only 15% of the SD. Using the reconstruction method described in 3.3.1 one can achieve an angular resolution below 1°. To guarantee the high quality of data during a measurement period a continuous atmospheric aerosol monitoring is performed by the operation of two laser facilites (CLF & XLF) [141] located inside the SD array and a LiDAR system at each FD site [142].

5.2 Enhancements

A few years ago the Pierre Auger Observatory has been enhanced with two extensions to be able to measure also the lower energetic component of the cosmic ray spectrum around $E = 10^{17}$ eV with a higher precision and drive the development towards multi-hybrid detection of EAS.

The first one is the *Auger Muons and Infill for the Ground Array* (AMIGA). In a first step the grid spacing of the SD was decreased to 750 m inside the so-called *Infill* by deploying 61 additional SDS in the field of view of the fluorescence telescopes at the site "Coihueco" (see Fig. 5.4). Data taking started in 2008 and has increased the acceptance for showers in the energy range from 10^{17} eV to 10^{18} eV significantly.

Additionally, sets of plastic scintillators, each with a total area of 40 m^2, have been buried in a unitary cell in the immediate vicinity of seven SDS inside the Infill to form the *Muon* part of AMIGA. Shielded by approx. 2.3 m of soil the muon detectors (MD) are designed to provide an independent measurement of the muon number, which then can give further indications on the composition of the cosmic ray primary particles. A schematic drawing of a scintillator set forming a muon detector station (MDS) is depicted in Fig. 5.5. A MDS is composed of four independent modules, two with a size of 5 m^2 and two of 10 m^2. Each of these modules consists of 64 plastic scintillator strips, which guide the light into a 64-pixel PMT. The MD front-end electronics then detects signals above an adjustable threshold. The unitary cell of the MD is taking data in a stable mode since 2014. A summary of the detector status and first results is given in [143].

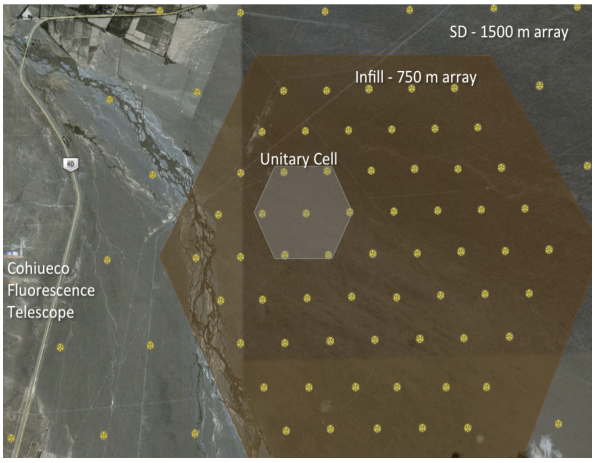

Figure 5.4: GoogleMaps view of the AMIGA array. Indicated are the SDS (yellow dots), the Infill area (brown background) and the area of the muon detector unitary cell (gray background). The location of the FD site "Coihueco" is shown as well, which is also the position of the HEAT extension. From [143].

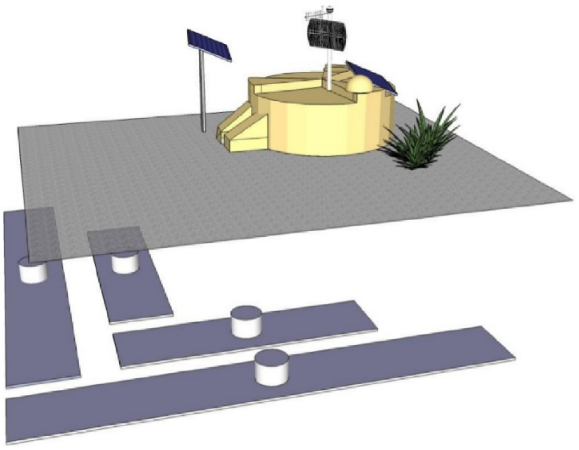

Figure 5.5: Schematic drawing of a buried muon detector showing the four individual scintillator panels. Indicated is the on-top housing of the front-end electronics, which can be accessed from the surface through a plastic tube. From [143].

The second extension consists of three additional telescopes, which are build near the fluorescence site "Coihueco" to overlook the infill array (compare Fig. 5.4). The main feature of the new buildings is, that they can be tilted upward as depicted in Fig. 5.6. If in upward mode their field of view ranges from 30° to 58.6° in elavation. This allows a detection of showers, which develop their shower maximum higher up in the atmosphere and/or closer to the telescopes.This lowers the energy range of the FD by one decade. A camera view of an example event measured with HEAT and the FD is shown in Fig. 5.7.

5.3 Future plans

The Pierre Auger Observatory has collected ten years of data, which corresponds to $40.000\,\mathrm{km}^2\,\mathrm{sr}\,\mathrm{yr}$ by now [144]. Unfortunately it is yet not possible to clearly pin down the origin of the flux-suppression at the highest energies, which would be an important keystone to resolve the remaining mystery of the sources of cosmic rays. A major step into this direction would be an improved identification of the primary composition. This can be achieved by a better discrimation between the electromagnetic and muonic shower components of the shower with the ground array, which requires a complementation of the existing water-Cherenkov detectors. After intense R&D efforts and assessments a

Figure 5.6: Picture of the three HEAT telescopes with closed shutters tilted to the upward mode.

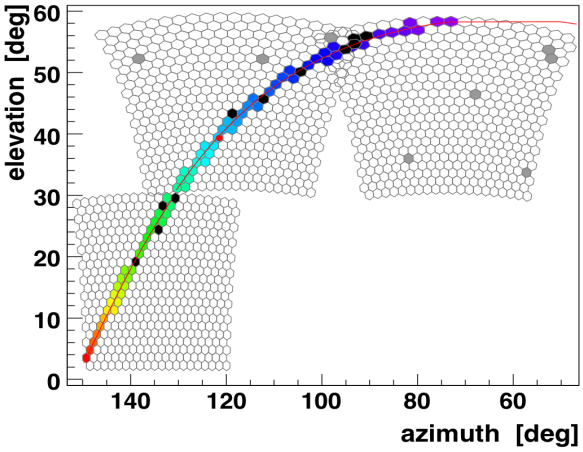

Figure 5.7: Combined view of the light trace of an air shower as measured in the cameras of one FD telescope and two HEAT telescopes.

solution with a scintillator on top of the detector was chosen to be deployed in the field. A photography of a prototype with a 4 m^2 scintillator is shown in Fig. 5.8.

Additionally, the electronics of the SD will be exchanged with a more powerful version allowing further trigger and monitoring possibilites. The deployment period is planned to last for about two years starting in 2016 and followed by at least five more years of data-taking until 2023, which would lead to a doubling of the currently collected statistics.

Figure 5.8: Picture of a water Cherenkov detector with a 4 m^2 scintillation prototype detector placed on top.

CHAPTER 6

The Auger Engineering Radio Array

The Auger Engineering Radio Array (AERA) was constructed within the Pierre Auger Observatory and is currently the biggest experiment for the detection of radio emission from extensive air showers worldwide. It was designed as an engineering array to follow up on the first digital radio experiments LOPES and CODALEMA and prove this method for large scale applications.

6.1 Motivation

The original proposal to the Pierre Auger Collaboration, submitted in 2009, includes three major physics cases [145]:

- **Calibration of the radio emission from air showers:** A detailed understanding of the underlying emission mechanism and their individual contribution to the total radio signal is mandatory for the improvement of hardward and methods for upcoming radio experiments. This will be achieved by the analysis of hybrid measurements of air showers, i.e. simultaneous detection by AERA and one or more different detectors of the Pierre Auger Observatory.

- **Exploration of the capability of the radio-detection technique:** The accuracy in the determination of direction, energy and mass composition of the measured air showers is the main criteria for the feasibilty of future stand-alone radio detectors and their performance in comparison to the already existing and established techniques. Additionally, the usability as component of a multi-hybrid detector (c.f. Section 5.3) can be tested in the co-operation with the other detectors at the Pierre Auger Observatory.

- **Composition measurements in the transition region of galactic to extragalactic cosmic rays:** Being sensitive to the longitudinal shower development, the detection of radio emission with an almost complete duty-cycle will allow high precision measurements of the composition in the energy range between 10^{17} and 10^{19} eV, where the transition from galactic to extragalactic source is expected to take place.

As already discussed in Chapter 4 the first two items of this list have already been targeted by AERA and other detectors with great success. A summary of recent results and future perspectives of AERA can be found in [146].

6.2 Deployment

Prior to AERA several small prototype setups have been installed at the Pierre Auger Observatory, operating as test-bench for hardware components like antennas and hardware. The first one was located at the BLS (c.f. Fig. 5.1b) and built up of three antennas in a triangle of 100 m distance in 2006. With a second setup at the BLS the first radio signal in coincidence with the SD was measured [147] and some hundred coincident events were observed until its shutdown in 2008. Afterwards, these antennas were replaced with a fully autonomous setup of four antennas, which then offered a starting point for a scalable array of radio detectors [148]. The data acquision for this setup was stopped in 2011. Another setup of three antennas placed at 140 m distance to each other around a SDS near the CLF, was also deployed in 2006. It was able to firstly measure a radio self-triggered air shower in his four years of operation [149].

AERA is located in the north-western part of the SD array, just inside the Infill and in the field of view of the FD sites Coihueco and HEAT to provide maximum intersection with the existing detectors and especially the low-energy enhancements of the Pierre Auger Observatory. The deployment was performed in several phases. Phase I started in September 2010 and consists of 24 radio detector stations (RDS) arranged in a triangular grid with 150 m spacing. It includes one triplet station, where three stations are separated by only 30 m to analyse small scale fluctuations. Phase II, deployed in May 2013, added 100 new RDS on a more sparse grids of 250 m and 375 m distance. Additionally, a low frequency antenna

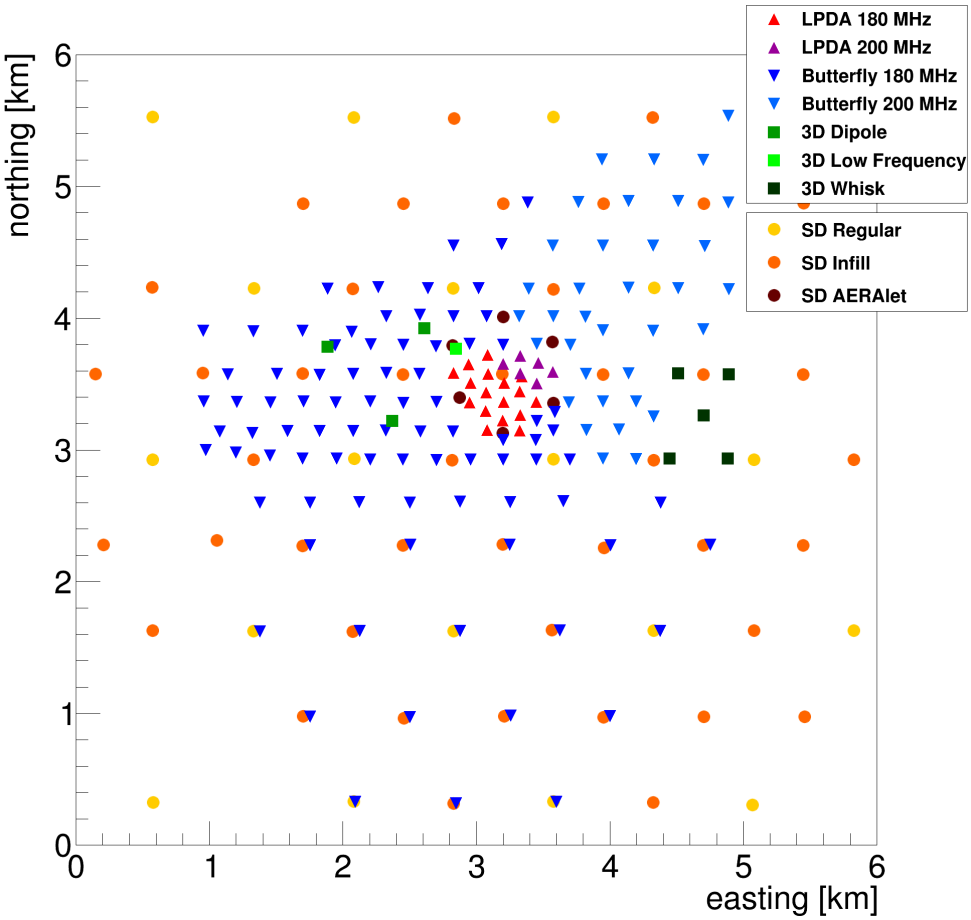

Figure 6.1: Map of the AERA array. Shown are the different antenna and hardware types for the RDS and the different grid spacings for the SDS. More explanation is given in the text.

(bandwidth: 1.5 MHz - 6 MHz), three 3D-dipole antennas and five 3D whisk antennas (on top of existing phase II RDS) have been built up as prototype stations to explore potential future extensions. Finally, 25 additional RDS were constructed in February 2015 with phase III, extending the existing array to the south with grid distances of 375 m and 750 m. The RDS with the latter spacing are each located in close vicinity to an Infill SDS.

The RDS of phase I and II add up to an area of roughly 6 km^2, which is now approximately doubled by the addition of phase III. This also enables a more efficient detection of very inclined air showers and due to the different grid spacings AERA can cover an energy range from 10^{17} eV up to 10^{19} eV. Simulations have shown, that several thousand events should be observable in this regime and with the current size of AERA. Furthermore, six SDS, the so-called AERAlet, have been deployed on a 433 m grid in the center of AERA to lower the energy threshold of the SD even further in this region [150].

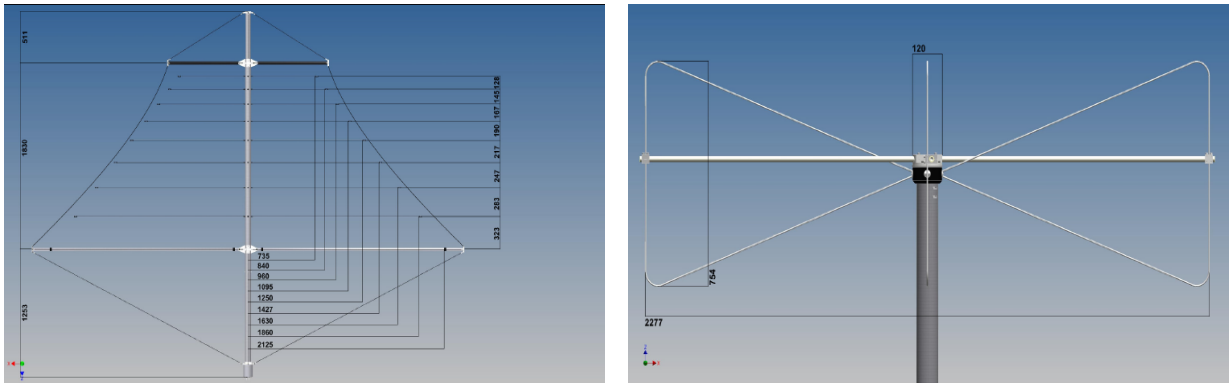

(a) (b)

Figure 6.2: Engineer drawing of a LPDA (a) and a Butterfly antenna (b), dimensions in mm. From [117].

Figure 6.1 shows a map of the RDS of AERA and some of the SDS in the Infill region. The RDS are flagged with respect to the used antenna and hardware type. Their differences will be explained in Section 6.3. From this point on we refer to the RDS flagged with 'LPDA 180 MHz' and 'Butterfly 180 MHz', if we talk about externally triggered RDS. Accordingly, when mentioning scintillator triggerd RDS, we are refering to the 'LPDA 200 MHz' and 'Butterfly 200 MHz' RDS. The prototype stations, '3D Dipole', '3D Low Frequency' and '3D Whisk' will not be discussed any further in this thesis. The SDS are marked accordingly to their grid spacing: Regular (1500 m), Infill (750 m) and AERAlet (433 m).

6.3 Station layout

In this section the essential parts of a RDS will shortly be introduced. This includes the radio antenna, analog signal chain and digital front-end electronics as well as the other environmental parts.

The most prominent feature of a RDS is obviously its radio antenna. For AERA two different types have been used so far, which share a design frequency from 30 - 80 MHz. For the phase I RDS a Logarithmic Periodic Dipole Antenna (LPDA) was chosen, which achieves its broad band sensitivity by the combination of dipoles with varying lenght, i.e. resonance frequencies. The possibility for a dual polarization measurement is achieved by solely aligning two of these dipole structures perpendicular to each other. This antenna type has already been successfully used in both prototype setups near the BLS with only a change in the dipole material moving from aluminium rods to wires for stability reasons in between. Figure 6.2a shows the final design, which was adopted slightly towards a better producibility and handling during the deployment [151].

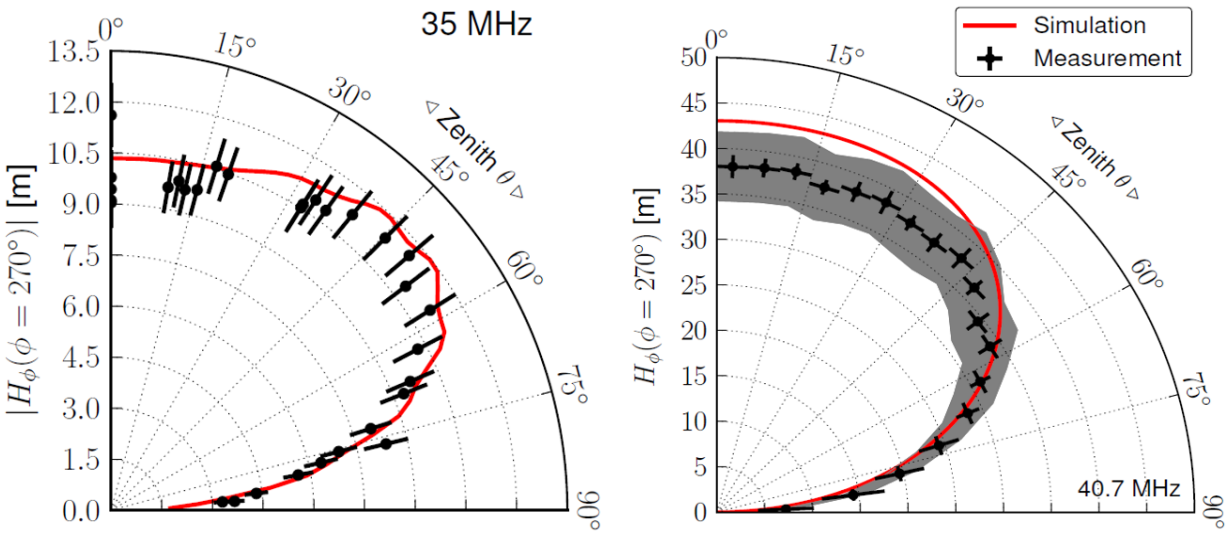

Figure 6.3: Simulation (red line) and measurement (black points) of the zenith dependence of the magnitude of the vector effective length for a LPDA at 35 MHz (left) and a butterfly antenna at 40.7 MHz (right). From [117].

The RDS of phase II and III are equipped with a so-called "Bow-Tie" or "Butterfly" antenna, which has already been used by CODALEMA and the prototype setup at the CLF. Its active element consists of two triangular wire arms made of 6 mm aluminium rods, which not only reduces weight, but leads to a very small amount of working surface for wind load. Also here the dual polarization is created by the perpendicular combination of two antenna elements, which are mounted to each other in a central nut as can be seen in Fig. 6.2b. To further increase the mechanical robustness and avoid oscillation and bending, an additional support structure made of fiberglass compounds is attached to each wire arm.

In addition to lab measurements both, antennas have also been calibrated after the deployment in the AERA field, to account i.a. for the non-negligable influence of the ground conditions. This was done by attaching a calibrated reference antenna to either a balloon or a GPS-guided octocopter, which were steered around the antenna. The reference antenna then emits signals at a fixed, but adjustable frequency, which can be measured in the AERA RDS and is analyzed with a vector network analyzer. Taking into account the actual distance of the emitter, one can achieve a three-dimensional sensitivity pattern of the considered antenna. Figure 6.3 shows the vector effective length determined by simulations and measurements for a LPDA and a Butterfly antenna for a given frequency as a function of zenith angle. Clearly visible is the more stable behaviour of the Butterfly for more or less the whole zenith range. Additionally, a loss of sensitivity towards the horizon, which is common for both antennas can be seen.

The antennas have been aligned in a dedicated campaign with one arm oriented parallel to the direction of the magnetic field at AERA, which is $\sim 2.5°$ East with respect to

Figure 6.4: Pictures of a phase I station with the LPDA (left) and a phase II/III station with the Butterfly antenna (right) in the Argentinean pampa.

the geographic North) and the other arm mounted perpendicular (see [152]). For a more detailed description of the electrical and mechanical properties as well as the calibration procedure of both antenna types see [74, 117, 153].

Both antennas have an integrated low-noise amplifier (LNA), which is used for a first amplification of the received signal and the limiting of the antenna bandwidth to the design frequency. Afterwards, the signal is guided into the electronics box, where it is further amplified and filtered by a filter-amplifier board again in the range from 30 MHz to 80 MHz, so it can be sampled in the first Nyquist domain. The frequency-dependent gain and group delay of the LNA and the filter-amplifier board have been determined by lab measurements and can be corrected for during the data reconstruction (c.f. 7.4). Depending on the front-end electronics the signal is digitized using flash analog-to-digital converters with a sampling frequency of 180 MHz and 12 bits depths for the externally triggered setup or 200 MHz and 14 bit depths for the scintillator triggered RDS respectively. A real-time trigger decision is made in a field programmable gate array (FPGA) based on pulse shape parameters and in case of a positive response, the voltage traces are stored in the station memory. Another, this time digital, bandpass filter is applied here.

A weather-proof box provides the housing for the station electronics, not only protecting them from environmental influences, but also shielding the antenna from noise generated by the electronics itself. For the phase I RDS this box was placed separately, while for phase II and III it is mounted directly onto the antenna pole. In both cases, the box is shadowed by the solar panel of the photovoltaic system, which provides the power for the autonomous operation of the RDS in combination with buffer batteries. A charge controller regulates and monitors the power transfer from the panels to the batteries. Due to a lower power consumption of the phase II communication system, the size of the solar panels and batteries could be reduced.

A seperate pole, mounted to the antenna pole, holds the communication antenna and the GPS receiver (see Fig. 6.5a). A central processing unit (CPU) in the front-end electronics handles the communication with the DAQ. The GPS receiver, which provides the timing for the measurement, yields an accuracy of $\sim 10 - 20$ ns [154]. This can be improved by the usage of a 'beacon' antenna. The correction procedure will be explained in Section 6.4.3. The whole RDS is surrounded by a non-conducting fence to protect it from 'advances' by the Argentinean wildlife. Figure 6.4 shows photographies of fully deployed RDS of both types inside the AERA field.

6.4 Additional components

Beside the installation of the 153 RDS some further infrastructure for maintenance, data acquistion and monitoring of environmental conditions has been created at the AERA site in the last years.

6.4.1 Data aqcuisition and triggering

The Central Radio Station (CRS), a solar powered, 40 feet shipping container (see Fig. 6.5b), was set up next to the phase I RDS and hosts one of the DAQ systems of AERA with the other one being located at the Coihueco FD building. The phase I RDS were read-out using an optical fibre system, which is directly connected to the CRS [155]. Since phase II all RDS have been equipped with a commercial 5.7 GHz wireless system with the eastern part of the array sending to the CRS, which then transfers the data-stream to Coihueco, if neccessary, while the western part directly sends their packages there.

Several trigger possibilities have been implemented to force the read-out of the RDS:

- The externally triggered RDS have the possibility to receive an **external trigger** from the CDAS. This trigger can result from the measurement of an air shower by the SD, which includes the Infill and AERAlet, when the estimated core position is close to AERA. Additionally, also the FD including HEAT can send a readout request. These stations have been equipped with a large ring buffer memory, which can store the measured data for up to seven seconds. This is neccessary to brige the time, which is needed for the CDAS to build these triggers. If an external trigger is formed, all externally triggered RDS, which are online at that time, will send their data to the DAQ.

(a) **(b)**

Figure 6.5: Pictures of a wireless communication antenna and a GPS receiver as used for phase II (a) and the CRS container with solar panels (b). The pole with the weather station, the electric field mill and the lightning protection tower are visible as well.

- To answer one of the major physics questions of AERA, that is whether an independent operation of radio detectors is feasible, also several **self-trigger** algorithms have been implemented into the station as well as the DAQ software. On station level, cosmic ray pulses are identified by an analysis of the pulse shape and different threshold schemes. An example can be found in Fig. 6.6. On DAQ level the trigger is formed either by calculations of physical time-differences [157] (externally triggered RDS) or based on amplitude-ratios of the two antenna polarizations (scintillator triggered RDS). Only the data from the triggered RDS are requested by the DAQ.

- A **scintillator trigger** is build, if the scintillators of the scintillator triggered RDS fulfill specific criteria e.g. a combination of threshold crossings. A conjunction of scintillator trigger and self-trigger is possible for these RDS as well. Also in this case only the triggered stations are readout.

- All RDS are read-out every 100 seconds. This interval has been increased on 26.06.2014 from 10 seconds beforehand to reduce the amount of data. These **periodic trigger** data are used to monitor the present radio background conditions as well as the current state of the RDS. Furthermore, they can be used as representation of the current noise situation for simulations.

- An additional trigger has been implemented for a special timing calibration method (c.f. Section 8.4). The **airplane trigger** tracks the trajectory of airplanes over the AERA field by their ADB-S signal and opens the self-trigger algorithm to this direction of the sky as otherwise those events would be rejected by the cone-algorithm.

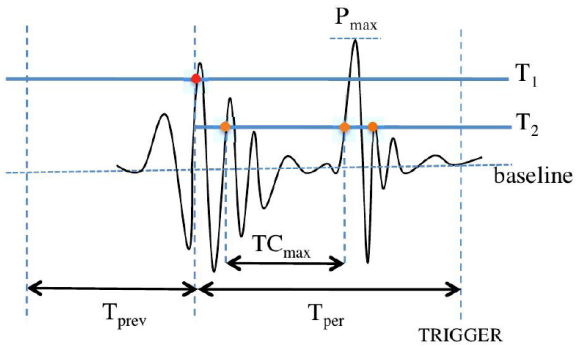

Figure 6.6: Illustration of a exemplary self-trigger scheme for the AERA RDS. From [156].

All processed data are accessable on a dedicated server in Argentina for immediate reconstruction and monitoring analyses. The produced ADST output, $\mathcal{O}(50$ MB/day), is transfered to Europe via network, while the full sample of raw data is frequently exchanged on disk due to its large amount, $\mathcal{O}(10$ GB/day).

6.4.2 Weather station and eField mill

As will be discussed in Chapter 9, the weather conditions and especially the atmospheric electric field can have a significant influence on the detection of the radio emission from air showers. Therefore, a good monitoring system is mandatory for a physical interpretation of the detector data, i.e. flagging not usable periods or correcting data based on the measured atmospheric parameters. A dedicated weather station was set up at the CRS in 2010 during the phase I deployment (see Fig. 6.7) [158]. It provides continuous monitoring of temperature, pressure, wind speed and hygrometry as well as the atmospheric electric field. The latter one is measured with a rate of 1 Hz using a field mill based on plate capacitors, while the rest of the parameters is read out once every 110 seconds with a commercial weather sensor. The data are stored locally at the detector site, but transfered daily to the AERA database, where they can be accessed e.g. for a visulization on the Auger monitoring website (c.f. Section 7.5) or for the use in data analysis. To further complement these measurements an additional weather station has been deployed inside the western part of the AERA field. Here, the electric field is measured once per second, while the weather data is read-out every five minutes. Also these data are stored in the AERA database.

6.4.3 Beacon

The accuracy of the station timing is very important for many physical analysis. Especially for interferometric applications a precision of ~ 1 ns is required. As already mentioned the

Figure 6.7: Picture of the weather station deployed on top of the CRS. Weather sensor (top) and field mill (bottom).

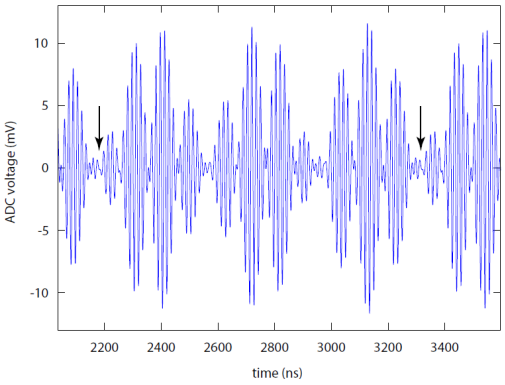

Figure 6.8: Voltage trace of the beacon beat after digital filtering has been applied. The period of the beat ($\sim$ 1.1 µs) is indicated by the arrows. From [159].

accuracy for current, synchronized GPS clocks is on the order of 10 ns, which is additionally biased by time drifts of the same order on the time scale of several hours. Thus, another method for the synchronisation of the different GPS clocks is needed.

Originally developed for the LOPES experiment [160], also AERA uses a so-called beacon reference antenna. It is built of a horizontally aligned dipole, mounted at the Coihueco fluoresence site and therefore roughly 3 km away from the first RDS. A signal generator mixes four sine wave signals, which are then emitted as a continuous wave. The chosen frequencies inside the AERA bandwidth are 37.8 MHz, 46.6 MHz, 58.8 MHz and 71.2 MHz. The first two have been switched to 61.5 MHz and 68.5 MHz on 15th August 2012. Due to their discrete nature, they can be filtered without further problems for triggering purposes in the DAQ as well as during the data analysis after the timing correction has been applied.

The characteristic beat of the superimposed waves repeats approximately every 1.1 μs and can be isolated from the recorded trace by digital filtering (see Fig. 6.8). From the timing information of the beacon pulse and the GPS measurement of the RDS the propagation time can be calculated. Thus, for a relative timing calibration an arbitrary station is chosen as reference to determine the offset of the expected time difference to the other stations, which then can be corrected for during the analysis process. The best way to determine the offsets, a cross-correlation analysis, would be too time consuming for the processing of large amounts of data. Therefore, a more simple approach is applied, which uses the phase differences of the sine waves. In the current version the measured phases are compared to reference values, which have been calculated by averaging over several hours of triggered AERA events.

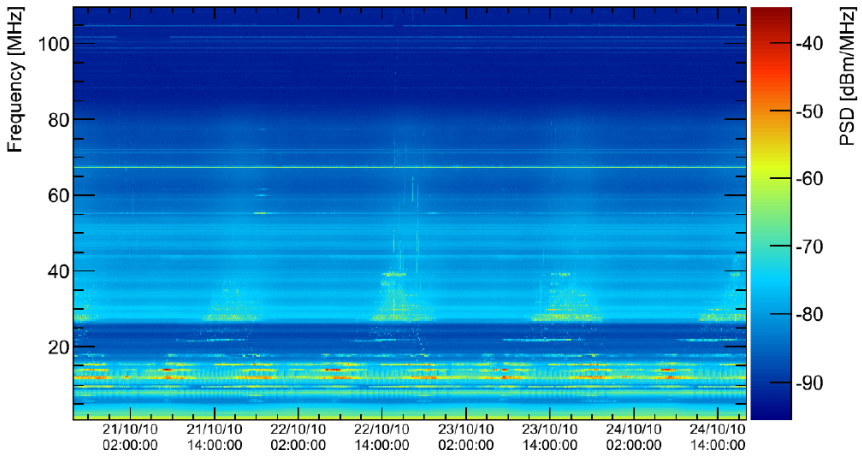

Figure 6.9: Dynamic spectrum for four days at the AERA site recorded with the reference LPDA. Shown is the power spectral density measured with the spectrum analyzer as a function of local time. From [161].

By applying this correction not only the GPS drifts can be corrected, but also an event-by-event time calibration with an accuracy of better than 2 ns can be achieved. Furthermore, an additional offset between the RDS of different antenna types was found using an alternative airplane approach. A full description of the beacon and airplane methods is described in [159].

6.5 Radio background

One of the major challenges, especially for the self-triggering of radio detectors, is the discrimination between air shower pulses and signals produced by the urban environment. As already shortly discussed in Section 4.1, there are several sources for these man-made interferences. To identify and monitor these sources a rotatable LPDA (mounted horizontally) and a reference LPDA without station electronics, but directly connected to a spectrum analyzer have been installed. Additionally, the phase I stations have been measuring several month using a simple threshold trigger to test the present background. Using these three methods a multitude of noise sources could been found.

Figure 6.9 shows the dynamic spectrum recorded for four days at the AERA site. Several narrowband-transmitters, visible as horizontal continuous lines, can be observed in the region below 20 MHz and above 100 MHz. Those transmitters are filtered out by the multiple stages of bandpass filters in the analog and digital chain in the AERA RDS. However, additional strong emitters at 55 MHz and 67 MHz are located inside the bandwidth of AERA and thus not filtered out directly. This holds also for the signals of the beacon. Here,

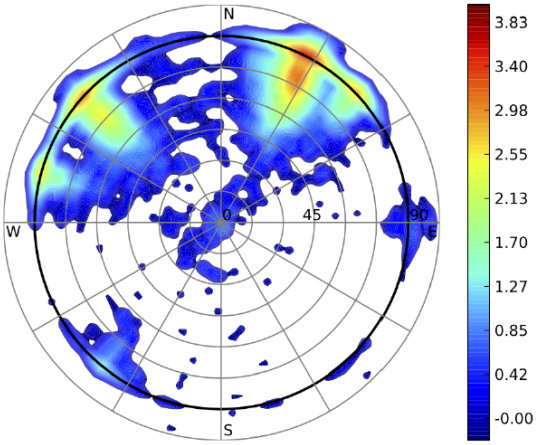

Figure 6.10: Polar skyplots of reconstructed self-triggered event directions for 8 hours of data in December 2010. The color scale is $\log_{10}$ (event density) [a.u.]. From [161].

several digital notch filters are implemented to remove these signals from the traces. This procedure is only used during the trigger procedure though. If the event is considered as candidate, the unfiltered trace is stored.

Furthermore, the spectrum displays some smaller regions, which yield a recognizably increased noise level only for discrete periods and thus indicate the emission of transient noise pulses. A directional analysis has shown that most of these transients can be traced back to hot-spots (e.g. transformer stations or power lines) in the vicinity of AERA (c.f. Fig. 6.10). These regions can be excluded afterwards in the DAQ with a fast directional reconstruction during the trigger building.

Another type of noise interference shows a certain periodicity. As already presented in [162] a majority of self-triggered events occured with a frequency of 50 Hz, which corresponds to the frequency of the high-voltage grid in Argentina. This behaviour is restricted by applying a veto algorithm in the station electronics.

However, the most dominant contribution in the case of broadband radio background is the emission from our Galaxy, especially the Galactic center. Studies of the root mean square of periodic triggered station traces have shown a recurrent variation, which is also visible in the dynamic spectrum in Fig. 6.9, especially in the region between 30 and 40 MHz. It was found that this oscillation is in phase if considered as function of Local Siderial Time. This leads to the conclusion that the transit of the Galactic Center over the AERA field is the main contribution to the noise floor.

CHAPTER 7

Data analysis with the Offline Framework

7.1 Structure

The Offline software framework of the Pierre Auger Observatory was designed as infrastructure for many computational purposes related to data acquisition by the observatory [163]. It is implemented in such a way, that collaborators can add their own algorithms and structures to fulfil their own analytical needs. Being able to read multiple input formats, e.g. detector data or simulation input, and yielding the opportunity of user-contributed configuration files, the framework provides a variety of applications. The three main structures of the framework are shown in Fig. 7.1.

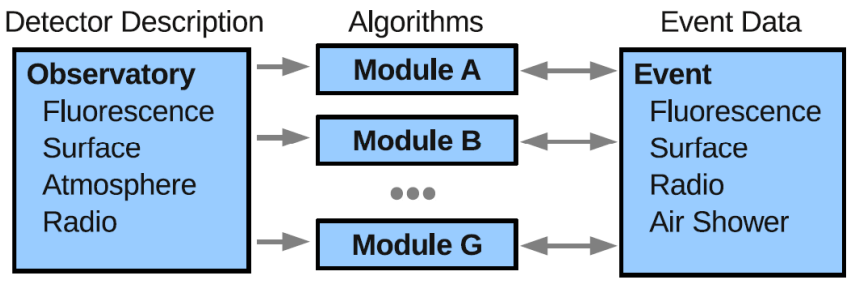

Figure 7.1: The main structures of the Offline Framework [164].

The modules are the processing backbone of the analysis framework, which incorporate the algorithms for specific purposes. They are sequentially ordered with respect to their analytical aim and can easily be exchanged or rearranged in different applications. Additionally, the input parameters for each individual module can be interchanged via a XML configuration. The event class is designed to carry all the relevant information coming from the input file or derived during the reconstruction. These are for example the traces measured by the individual detectors, but also properties of the air shower event like the incoming direction or the reconstructed energy. Therefore, the modules can read, but also modify the information in the event class. On the other side, the detector class holds the configuration of the observatory at measurement time, e.g. detector positions or atmospheric conditions, and is for this reason only readable from the module side. The whole detector information are stored either inside of XML card files or in a central database, which is of special interest for the radio reconstruction (see Section 7.4).

Beside the aim of performing the analysis measured by the Pierre Auger Observatory, the $\overline{\text{Off}}\underline{\text{line}}$ framework provides the opportunity to display the results of the reconstructions in the so-called *EventBrowser*. It can be used to show information for the different detectors as well as array views with the participating detector stations. In addition, several detector specific properties like pixel maps of the FD or station traces of the RD in time- and frequency domain can be viewed. Figure 7.2 shows an example event in the RD tab of the EventBrowser.

7.2 The RdObserver application

The RdObserver was created to provide a common application in the $\overline{\text{Off}}\underline{\text{line}}$ framework for the production of high-level analysis files from the data collected with AERA. It has been developed as part of this thesis in several stages and versions, which will be discussed in Section 8.1, each of them focusing on specific aspects of the data quality. In this section the components of the RdObserver as of version v1r3, which was used for the first full reconstruction of the externally triggered data of AERA Phase 1 and 2, will be discussed.

The module sequence can mainly be split into six different parts, which will be introduced below in more detail (module names in `true-type`). A schematic overview of the module sequence is shown in Fig. 7.3. The full module sequence can be found in Appendix A.

In the beginning of the module sequence a specified input file with merged data from the four different detector types (SD, FD, muon and radio) is read in by the `EventFileReader`. For further information on the merging processes and the different file formats see Section 7.6. To save processing time a subsequent event pre-selection is performed in the `RdEventPreSelector`. This selection is based on simple criteria, which can be taken from

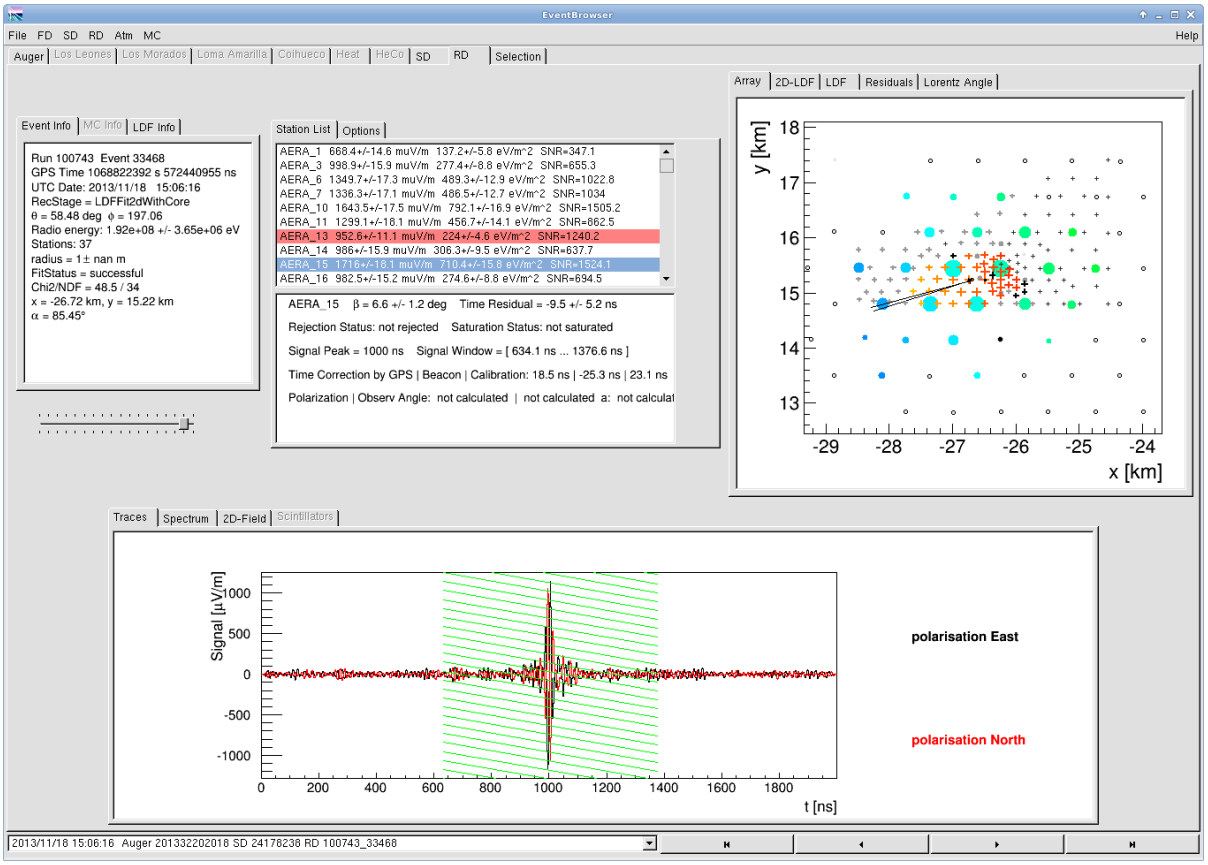

Figure 7.2: EventBrowser view of an example event in the RD tab. Shown are the event information frame (top left), station list with signal amplitudes and station information frame (top middle), array view (top right) and time-domain trace of the selected station with the corresponding signal search window (bottom).

the input data without any further processing. Here, a minimum of three RDS in the event is required to enable the possibilty for a successful direction reconstruction and only externally triggered events are selected.

The next part is dedicated to the reconstruction of the data coming from the SD. The modules used were mostly incorporated from the already existing *SdInfillDataReconstruction* standard application of Offline, which is adopted for the special requirements of data from the SD stations inside the infill array with the reducted grid size of 750 m. For a detailed overview on the SD reconstruction see [138, 165]. The directional reconstruction is done within the `SdPlaneFit` module followed by a combined fit of the lateral distribution of the particles at ground level and the position of the shower core in the `LDFFitter`. A good estimation of these two quantities, shower direction and core position, is necessary as they are used as seed for the now following reconstruction of radio data.

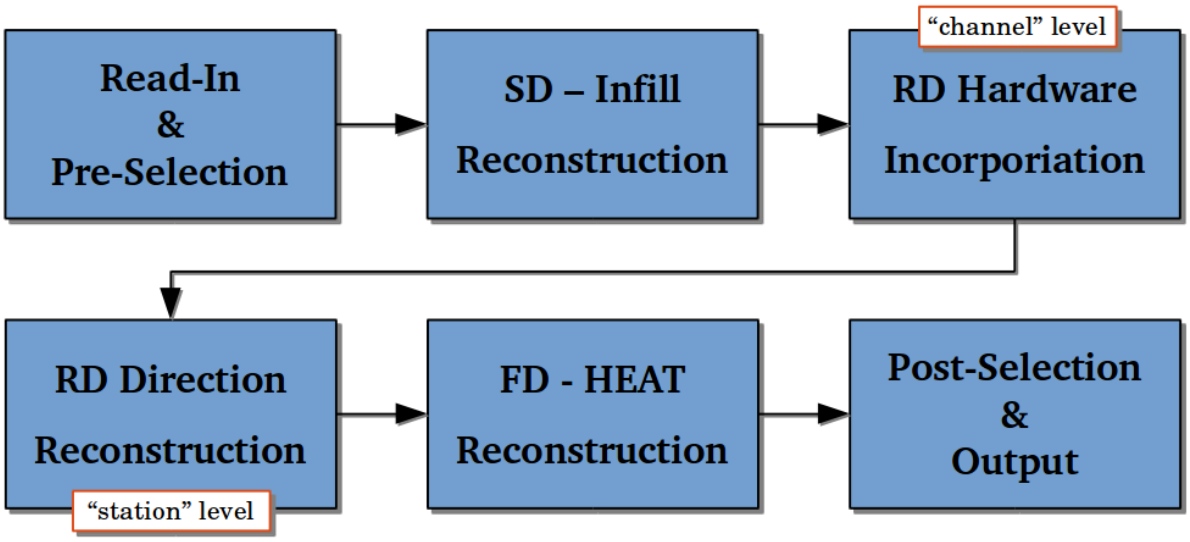

Figure 7.3: Schematic overview of the different parts in the RdObserver module sequence.

The radio part itself is can be split in two seperate sections. The first one is mainly dedicated to the incorporation of hardware responses as well as timing corrections (channel level), whereas the second part consists of the actual signal and directional reconstruction (station level) applying several selection algorithms.

The first module in the radio part is the `RdEventInitializer`. The shower direction and the core position for the radio event are set to the values determined by the SD reconstruction as mentioned above to provide a good starting value for the directional reconstruction and especially the incorporation of the antenna pattern later on. Also the signal and noise windows are defined. The noise window is fixed to the region from 2000 ns to 5000 ns inside the trace, whereas the signal search window is set relative to the event time deduced by the SD reconstruction. The time-settings for the signal search window are topic of the analysis in Section 8.3.

In the `RdStationPositionCorrection` the trace start times of the individual RDS are corrected according to their measured station position. The `RdStationRejector` rejects RDS by a user-defined list, which currently only consists of the RDS with a 3D antenna. For the near future also a rejection by a database of bad periods for individual RDS is under development. The measured ADC counts are converted into a voltage by the `RdChannelADCToVoltageConverter` using calibration values from the detector database. A set of channels for each polarization is selected for each RDS in the `RdChannelSelector` regarding if a channel is saturated or not. A constant baseline is removed by the `RdChannelPedestalRemover`.

An important step is performed in the `RdChannelResponseIncorporator`, which is the incorporation of the measured response functions of the individual hardware components of

each RDS. These values are again taken from the detector database. Further improvement of the timing is achieved by applying the beacon correction in the `RdChannelBeaconTimingCalibrator` as discussed in Section 6.4.3. After that, the beacon signal itself can be removed by the `RdChannelBeaconSuppressor`, which is done by suppressing the individual bins of the beacon frequencies in the measured spectrum of each RDS by a factor of 10^{-20}. Timing offsets for individual RDS have been determined by a method using airplanes over the AERA array [166] and are corrected for in the `RdStationTimingCalibrator`.

Finally, a check is performed if the defined signal window is fully contained in the trace and corrected in the `RdStationTimeWindowConsolidator` if necessary. This is especially important for very inclined events as well as events with large uncertainties on the SD shower core, which are then transfered into a large signal window. The `RdChannelTimeSeriesTaperer` applies a Hann window function with a width of 1% of the total channel trace to avoid clipping effects. In the `RdChannelBandstopFilter` an algorithm for the reduction of RFI noise pulses is applied, which is described in more detail in Section 8.5. Upsampling of the channel trace by a factor of 4 is done in the `RdChannelUpsampler`. This is possible due to the Nyquist-Shannon-Theorem, which states the possibilty for an exact reconstruction of a measured signal if the sampling frequency of the detector is larger than the doubled bandwidth of the signal:

$$f_{\text{sampling}} \geq 2 \cdot \Delta f_{\text{bandwidth}} \tag{7.1}$$

This holds for AERA as the externally triggered RDS are sampling with $f_{\text{sampling}} = 180$ MHz, while the design bandwidth is only $\Delta f_{\text{bandwidth}} = 50$ MHz. The `RdChannelRiseTimeCalculator` performs a calculation of the signal rise time in the channel traces. This quantity has been studied in [167] and can be used as seperator between CR and noise events. Nevertheless, this cut has not reached a mature state right now and therefore, only the calculated values are stored for a potetial later use in a high level analysis.

The `RdAntennaChannelToStationConverter` starts the directional reconstruction part of the RdObserver. Here, the calibrated traces of the individual channels are transfered to the station level, i.e. the real three-dimensional electric field vector, by unfolding the influece of the antenna pattern from the measured signal. The direction reconstructed with the SD is used as reference for the antenna pattern, which provides a sufficient accuracy with respect to the slowly varying gain of the antenna pattern. The calculation of the actual signal properties is performed in the `RdStationSignalReconstructor`. Using a Hilbert envelope the time of the pulse maximum and the signal-to-noise ratio (SNR) are calculated on the combination of the horizontal field components, i.e. North-South and East-West. This is done to negate the impact of the time uncertainty in the vertical component of the field vector, which arises especially for inclined events. If the SNR exceeds a value of $\text{SNR}_{\text{RDS}} > 10$, the specific station is a "signal station" and considered for the further reconstruction steps on the radio signal afterwards.

A first one of these is done in the `RdStationEFieldVectorCalculator`. Also here the core position and direction reconstructed with the SD is used, now to calculate the angle between the measured electric field vector and the vector of the Lorentz force, $\beta_{\measuredangle F_L}$. It is a good measure to distinguish CR from noise pulses that show a more or less random distribution of $\beta_{\measuredangle F_L}$. CR pulses under normal conditions should go according to the polarization expectations with only minor deviations $\mathcal{O}(10°)$ due to the charge-excess fraction of $a \approx 14\%$. However, a more sophisticated analysis still has to be performed and thus, a rather conservative cut of $\beta_{\measuredangle F_L} < 55°$ is used to reject individual stations from the reconstruction process. This is of major importance for the analysis performed in Chapter 9 as otherwise it rejects many of the events used in the polarization study.

After this rejection based on the measured pulse two additional modules are added to select or reject stations based on geometrical properties. The `RdTopDownStationSelector` is placed inside an iterative loop with the `RdPlaneFit`. Starting with the minimum number of three stations required for a directional fit, further stations are added with each iteration according to their distance to the shower axis going from near to far. Then the `RdPlaneFit` performs a fit of the arrival direction and the core position is estimated using a barycenter algorithm. Afterwards, the module checks if the χ^2-probability of the previous fit exceeds a certain level, which in case of the RdObserver is set to 5%. If so or if the fit was not successful at all the last added station is rejected permanently, otherwise it is kept as signal station. Then the loop continues with the next-closest station until all stations have been considered.

Additionally, two further algorithms are applied in the `RdClusterFinder` based on the geometrical pattern of the full remaining set of signal stations in the event. They are explained in more detail in Section 8.3 and will therefore be skipped here. Afterwards a final fit is done with another call of the `RdPlaneFit` to finalize the directional reconstruction.

The `RdStationRiseTimeCalculator` performs the same calculations as his namesake on channel level, but also here no cut based on the achieved parameters is applied yet. The main part of the `RdEventPostSelector` in the RdObserver is the coincidence check based on the angular deviation and the distance between axis and core of the SD and the RD reconstruction. These checks and the chosen parameters are discussed in Section 8.3.

The next two modules are both used for the reconstruction of the radio LDF. The `RdLDF-MultiFitter` performs a one-dimensional fit using two different exponential functions. However, as already discussed in Section 4.4 this one-dimensional approach is not sufficient due to several aspects of the radio emission. Therefore, the `Rd2dLDFFitter` uses the double Gaussian function as of Eq. 4.29. If an event is successfully fitted the radio energy emitted by the extensive air shower can be estimated. For events with more than four RDS also a fit of the core position is performed.

The following FD part is optional, i.e. even if the reconstruction of the FD data is not successful the event will still be processed further. The modules used are mainly adopted from the FD data reconstruction application. Some detailed information on the reconstruction procedure can be found in [168]. Additionally, some modificiations have been applied to be able to perform a combined reconstruction with the HEAT data. The major step here is the creation of a so-called *virtual eye* "HeCo", which is done in the `FdEyeMerger`. For further details on the modified HEAT reconstruction see [169].

The `RdStationTimeSeriesWindowCutter` cuts the traces of all the stations in the event to a configurable size. For the RdObserver this has been specified to 2000 ns around the reconstructed position of the pulse maximum. This is mainly done to save disk space when storing the event as the traces occupy the largest fraction of data for a radio event. The `RdStationTimeSeriesTaperer` is applied once more to avoid clipping effects at the edges of the trace with the same 1% Hann window like on channel level.

The last modules in the sequence are dedicated to the creation of the output files. All the parts needed for a simulation of the event with CoREAS are written by the `RdREASSimPreparator`. The `EventFileExporter` directly extracts the original event from the input file and saves it again in the Offline format. This enables a repeated reconstruction for specific sets of event, e.g. the full RdObserver sample, without the need to reprocess the complete amount of raw data. Finally, the `RecDataWriter` creates the ADST file, which holds all the information and reconstruction quantities of the event. These files can be used for high-level analysis or to display the events with the EventBrowser.

7.3 The RdSimulationObserver application

The RdSimulationObserver application is basically the counterpart to the RdObserver, which is used for the detector simulation and reconstruction of simulated events. As the main reconstruction parts are identical to the ones in the RdObserver, this section will be focused on the additional modules for the processing of the simulation files in the RD and SD part. The full module sequence can be found in Appendix B.

Before the reconstruction is started, the particle as well as the radio signal have to be created from the simulation input. Therefore, the `RdStationAssociator` associates the simulated radio pulses to the real detector stations. To account for uncertainties of the directional reconstruction a possible offset between simulated and real position of up to 5m is tolerated. The `EventGenerator` then creates the event and detector structure for the complete air shower setting the event time and the core position to the one from the radio shower.

For the SD detector simulation part the `CachedShowerRegenerator` is more or less the correspondent to the `RdStationAssociator`. Afterwards the response of the detector as well as the different trigger levels are simulated and finally the complete event is build. For a more detailed description on the SD simulation see [170].

The RD detector simulation part starts with `RdAntennaStationToChannelConverter`, which performs the inverse operation of the `RdAntennaChannelToStationConverter` to convert the electric field vector on station level back to traces for the individual channels. Also the `RdChannelResponseImcorporator` is configured by an additional flag to apply the inverse response when called for the first time per event, thus going backwards in the hardware chain from the physics antenna to the front-end electronics. The `RdChannelResampler` then resamples the simulation data to the sampling rate used in the experimental setup and the `RdChannelTimeSeriesClipper` clips the trace to the amount of samples as normally taken by the detector. Finally, the `RdChannelVoltageToADCConverter` converts the voltage at the entrance of the electronics to the corresponding ADC counts, which then leads to input data equal to the one measured for a real CR event.

Optionally, noise can be added to the traces with the `RdChannelNoiseImporter`. This module offers several possibilites to select samples from an external noise library. For the simulations in Chapter 9 a dedicated library was created, which contains all the periodic triggered events in a time period of ten minutes around the reconstruced events of the dataset used for the simulation. These traces represent the specific noise floor at the time of the event. For each event one noise trace is randomly chosen out of this interval and added to the signal trace with the corresponding length.

Afterwards the normal RdObserver reconstruction as discussed in the previous section is attached, except for some minor modificiations. As there is no need for a timing correction using the beacon signal or the generic offsets the `RdStationPositionCorrection`, `RdChannelBeaconTimingCalibrator`, `RdChannelBeaconSuppressor` and `RdStationTimingCalibrator` were removed from the sequence. Furthermore, the creation of the output files by the `RdREASSimPreparator` and the `EventFileExporter` have been taken out. A FD detector simulation and reconstruction are not included yet.

7.4 Time-Dependent Detector Description

A RDS is a very complex structure, which is composed out of many different hardware components (see Section 6.3). These components and their corresponding response properties do not just vary in between stations due to the general station layout in the different deployment stages of AERA, but vary between the items of one part like LNA, which are separately calibrated for each piece. When damaged or not working during the lifetime of

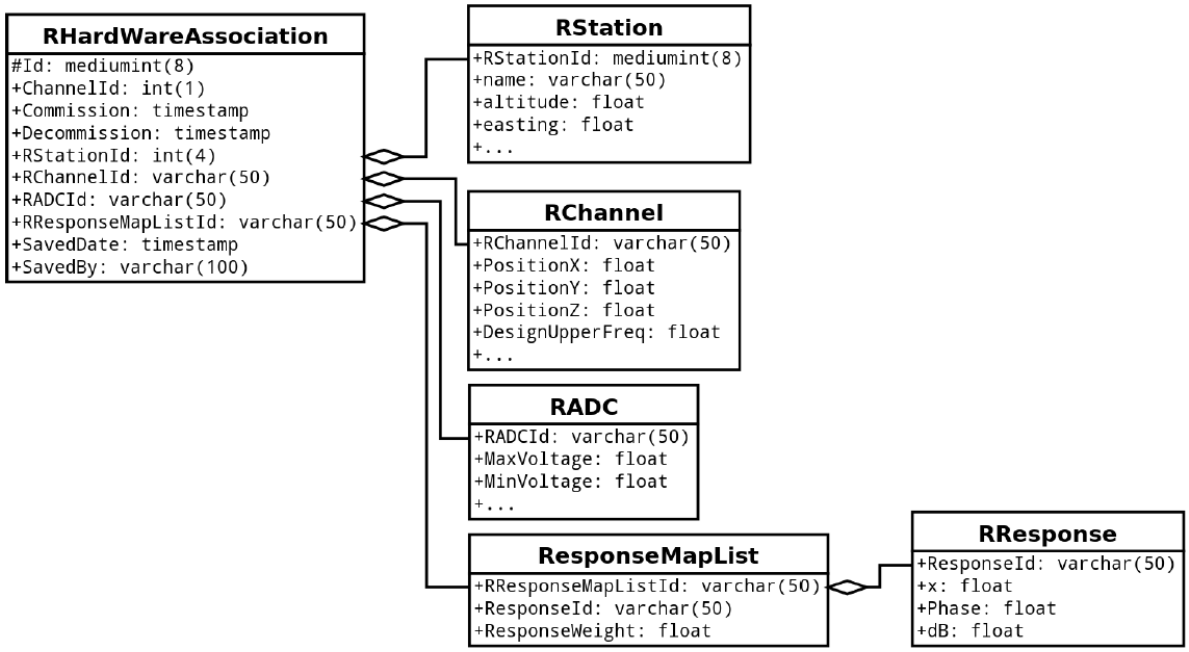

Figure 7.4: Schematic representation of the MySQL™ tables, columns and their dependencies.

the experiment single parts of a RDS are replaced. Therefore one needs a highly flexible and moreover time-dependent description of the array as a whole and each individual RDS.

As part of this thesis the structure of a MySQL™ database with several joined tables was developed to fulfil this purpose and to be able to give a representation of a specific RDS at a given time on demand (e.g. for the data reconstruction).

The database is split into the following tables:

- The table **RHardWareAssociation** is the main component of the database as it combines all the necessary informations for one specific RDS. It holds the following values: ChannelId in Station, commission and decommission time, RStationId, RChannelId, RADCId and ResponseMapListId. The last four entries are used as identifiers to get the corresponding information from the **RStation**, **RChannel**, **RADC** and **ResponseMapList** tables. Whenever the hardware of a RDS is changed, the channels, where the changes have been made, get decommissioned and a new one with the identifiers of the newly deployed hardware is commissioned. Therefore, only one configuration per RDS and channel is valid at a given time. This information can now be used to e.g. fill the *RDetector* information in of Offline.

- The table **RStation** contains the informations which mostly describe the physical detector on station level like name, position (in altitude, easting, northing) and number of channels.

- In contrast to that the table **RChannel** holds the information to describe the detector on channel level like channel type (e.g. high or low gain), design frequency, orientation and most important the antenna type.

- The table **RADC** stores the minimum and maximual voltages as well as sampling frequency and bit depth for the installed ADCs per channel.

- To be able to correct for the impact of the hardware on the measured signal one has to incorporate the response of all the relevant parts in the signal chain like LNAs and filters. The table **RResponse** holds the calibration data for a specific component with the respective amplitude (dB) and phase for a given frequency (x). This means that we have multiple entries (one per frequency) using the same identifier (ResponseId).

- These identifiers are then grouped into one RResponseMapListId inside the table **ResponseMapList** with a corresponding weighting factor for each ResponseId allowing for example to apply the response of a cable with its length. This RResponseMapListId is again the identifier for the corresponding station and channel inside the **RHardWareAssociation** table.

A schematic representation of the detector related tables and their dependencies can be found in Fig. 7.4. Additional tables are stored in the same database which hold more utility-based informations for the reconstruction:

- **BeaconFreq** and **BeaconRefPhase** contain the beacon frequencies with a commission and decommission date and the corresponding reference phases for each individual RDS (c.f. Section 6.4.3). These data are used e.g. for the timing calibration purposes during the RdObserver reconstruction (see Section 8.4).

- **WindowDefinition** contains the default Signal- and NoiseWindowStart and -stop values with comission and decommission date for a specific RDS hardware type. This values are not used right now during the RdObserver reconstruction process, but are taken from the user-specified `RdEventInitializer` configuration.

- **utm_data** contains the UTM ellipsoid, zone and band for the position of the Pierre Auger Observatory. Those values are used for position calculations inside the reconstruction.

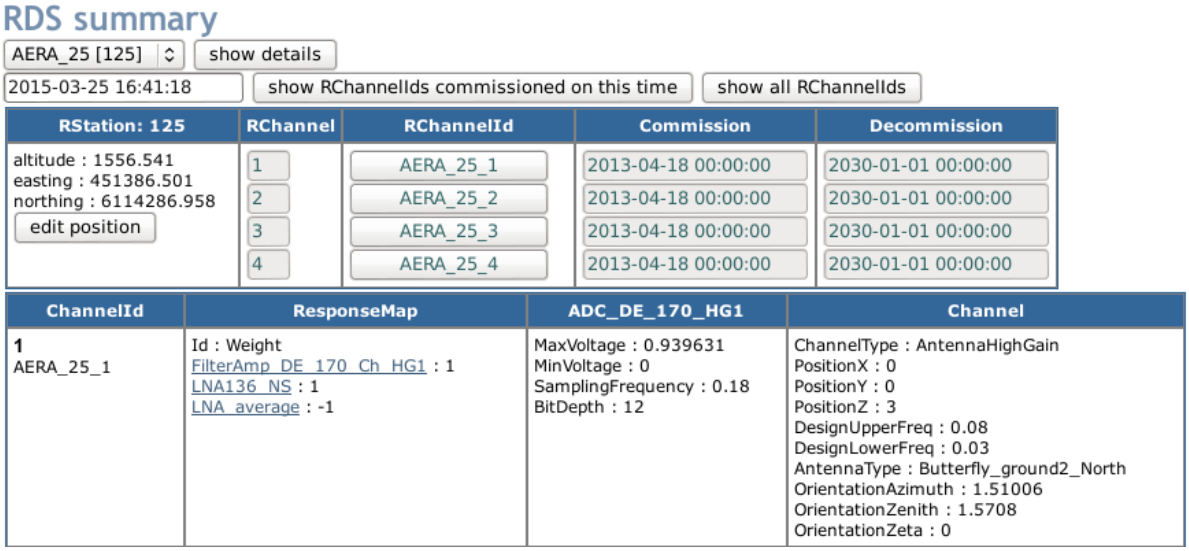

Figure 7.5: Screenshot of the RDS page of the time-dependent detector web-interface.

7.5 Monitoring Web-Interface

A web-interface has been developed to be able to display and edit the content of the time-dependent detector database [171]. It is integrated into the standard Auger monitoring in the RDS section of the AERA part.[1] A screenshot of the main page can be found in Fig. 7.5. It can be used to display the configuration of individual RDS for a given date or for the whole lifetime of the station. Additionally, a list of the ADCs can be shown or the response functions for a given hardware part (LNA or filter amplifier) can be plotted including amplitude and phase, see Fig. 7.6a.

If a RDS hardware is changed, this can be committed to the database by editing the specific channel data directly or by creating a new channel using the *copy channel* functionality. In this case a new name as well as the standard channel fields can be assigned. Afterwards the user can specify the ADC and ResponseMap, which are present in the channel.

Additionally, a display for the data measured by the AERA weather stations has been developed as part of this thesis and has been integrated into the monitoring.[2] Here, all the relevant quantities like e.g. wind speed, pressure, humidity and atmospheric electric field can be viewed against time. Figure 7.6b shows a plot of the atmospheric electric field measured with both AERA weather stations (WS-AERA and WS-CRS).

[1] `http://mon.auger.uni-wuppertal.de/pro/AERA/RDS/`
[2] `http://mon.auger.uni-wuppertal.de/pro/AERA/WeatherStation/`

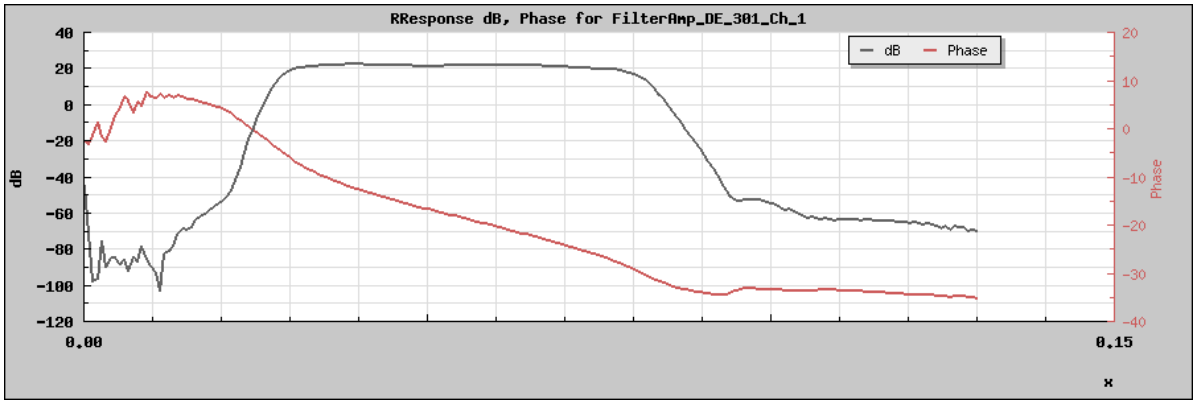

(a)

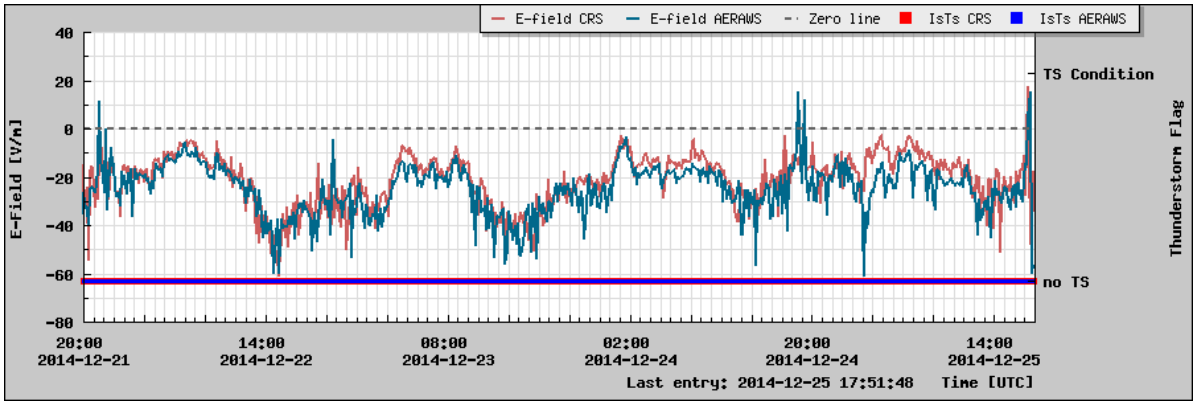

(b)

Figure 7.6: Gain in dB and phase in radians versus frequency in GHz for an example LNA (a) and atmospheric electric field versus time (b) as pictured in the Auger Monitoring.

7.6 Automated production

The input for the RdObserver reconstruction on the dedicated server in Argentina is created in several steps on a daily basis. First the data coming from the baseline detectors, the so-called ad-files, are merged with data from the muon detector leading to xad-files. Those are merged once more, now with the radio data using the recently developed `AERAROOTIO`-library [172] and named xrad-files afterwards. All three different file types (ad, xad and xrad) are stored in the `IoAuger` format, which is the standard data format for the Pierre Auger Observatory. Having all the required data inside of one data file already at the input level of Offline is a major improvement to previous reconstructions as it saves a lot of computational time as well as memory and storage space which would be needed for an intermediate merging step.

Afterwards the reconstruction with the RdObserver is initialized. First a check is performed, if a xrad-file has been processed before. This is done to guarantee a robust procedure as there might be a delay in processing due to problems during the data transfer, merging or reconstruction e.g. caused by power-cuts. For the automated production a time interval from 15 to 5 days prior to the current date is checked via the existance of the log file. If the file for one day is not available, the `EventFileReader.xml` and the `bootstrap.xml` are modified according to the xrad input filename and the directory for the output of the `REASSimPreparator` files. Then the actual reconstruction is started and the terminal output is written to a log file. The machinery is set up to process up to 14 reconstructions in parallel.

The produced output files are transfered to the central storage place on a ftp-server in Europe resulting in *daily available, fully reconstructed datafiles* for the collaboration.

CHAPTER 8

Improvement of the RdObserver

The RdObserver is the current standard reconstruction for externally (e.g. by SD or FD) triggered radio data (c.f. Section 7.2) in Offline. It is used for the daily and continuous processing of data measured with AERA producing a dataset for high-quality analysis. In this chapter the different versions of the RdObserver up to the current state, the major improvements, which have been applied, and their main goal will be discussed. Finally, some results of the first full AERA reconstruction will be presented.

8.1 Versions

The general structure and most of the modules of the RdObserver have already been discussed in Section 7.2 in sufficient detail, therefore this section will give a short overview over the different versions of the RdObserver in terms of quality improvement. A summary of the versions up to now with their corresponding revision in the Offline repository and the main changes can be found in Tab. 8.1.

At the very beginning of data taking with AERA the reconstruction of RD and SD data were executed separately. The search for coincidences was then performed afterwards using shower and timing parameters of SD events in the region of the RD array. In this context the radio part was mainly focused on an efficient selection of cosmic ray candiates to be

version	svn revision	focus / changes
v1r0	r.25467	• efficient CR event reconstruction • iterative direction reconstruction • SD / RD coincidence check (direction & core)
v1r1	r.27074	• increased purity of reconstructed sample • modified signal search windows • timing and position correction • single fit reconstruction using SD seed • top-down selection and cluster finding
v1r2	r.26979	• corrected detector database
v1r3	r.27304	• corrected antenna pattern usage

Table 8.1: Overview of different RdObserver versions, their Offline svn revisions as well as focus and changes.

able to gain as much experience as possible with the collected data neglecting a significant contribution of noise events in the sample. The limited bandwidth for the transfer of data to Europe resulted in the need for an optimized way of storing the reconstructed information. For this reason i.a. a compromise had to be made to trade the length of the stored trace for an increased upsampling factor, i.e. an improved representation of the evolution of the recorded signal. In addition, also some other parameters with respect to the reduction of the influence of noise, like a Hann-window for the signal region, have been optimized and applied.

The RdObserver v1r0 is the first attempt of a standardized radio reconstruction in a concurrent, hybrid approach using also SD parameters. After the hardware corrections have been applied, the reconstruction of the shower direction is done in an iterative way. Starting with the direction obtained by the SD reconstruction the antenna pattern is applied to the channel traces and afterwards the trace on station level is constructed. which is then used to perform a plane wave direction fit to the data. This is done in a loop until a certain level of convergence with respect to the direction of the last iteration is reached or the number of calls expires a previously defined limit. If convergence is reached, the event moves on to the post selection stage, which includes a coincidence check based on the shower direction and core position of SD and RD, otherwise it is rejected. The focus for this version is to select as many CR candidate events as possible, i.e. a high efficiency, neglecting the amount of noise events in the sample. Therefore, all thresholds on selection parameters are set very generous, e.g. a large signal search window of ± 3 µs around the signal or a maximum allowed distance of 5 km between the SD and RD core position.

Based on this starting point a lot of analyses have been performed in between versions v1r0 and v1r1 to increase the quality of the reconstruction as well as the purity of the

dataset. A new method to reduce the signal search window and two new algorithms for the selection of stations were implemented into Offline (see Section 8.3). Additionally, due to the non-stringend post selection cuts in v1r0 many noise events with a random direction coincidence entered the reconstructed sample, creating a large background for high-level analysis. This is reduced by refining these cuts to more reasonable values (see Section 8.3). Major improvement regarding the reconstruction quality was achieved by applying corrections to obtain a more precise station timing (see Section 8.4) and a new and time-efficient method of RFI suppression, to minimize the influence of noise pulses (see Section 8.5).

The most recent versions did not experience a large overhaul in the general reconstruction logic, but more in the environmental part of Offline. Version v1r2 was released after a major update of the time-dependent detector database, which solved a problem concerning ringing in the recorded traces after the reconstruction, while v1r3 includes a bugfix for the correct application of the antenna pattern leading to a more accurate treatment of the channel traces and their derived quantities. This version was used for a complete reconstruction of the externally triggered dataset of phase II, of which results are shown in Section 8.6.

8.2 Purity Analysis

The following sections will be dedicated to specific parts of the RdObserver, which have been investigated regarding their influence on the reconstruction mainly in the step going from v1r0 to v1r1. The analyses have mostly been performed in such a way, that the reconstruction was done several times for a given dataset with a modified configuration or module sequence. Afterwards, the resulting sample was divided into cosmic ray candidates and noise events by manually checking every single event. The decision was based on several criteria like pulse shape, spectrum, core positions, station clusters, etc. Using these subsets one can perform a rudimentary separation check for different reconstruction parameters and also estimate a purity of the dataset for the current configuration:

$$\text{purity } \rho = \frac{\#\text{ events}_{\text{ CR cand.}}}{\#\text{ events}_{\text{ total}}} \tag{8.1}$$

Applying this to the RdObserver v1r0 dataset for the period from 01.01.2014, 12:00 to 15.01.2014, 12:00 one finds 61 CR candidates in a total of 163 reconstructed events leading to a purity of $\rho \sim 37.4\%$, which will be used as the reference value from here on. A summary of the achieved purity with the intermediate improvement steps of the RdObserver, which will be explained in the following subsections, can be found in Tab. 8.2.

version / modifications	**total events**	**CR cand.**	**purity ρ [%]**
RdObserver v1r0	163	61	37
change to single direction fit + modified signal search windows + top down + cluster algorithm	187	108	58
previous + cut $\Delta_{\text{axis/core}} < 2000$ m	154	108	70
previous + online bandstop filter	141	113	80

Table 8.2: Summary of dataset purity for different improvement steps of the RdObserver

8.3 Station and Event Selection

One of the main contributions to the impurity of the RdObserver v1r0 dataset can easily be identified as the wide signal search window (± 6 µs), which was set to the same fixed part of the trace for each RDS. The large allowed difference of the SD and RD core position results in a huge probability of selecting a noise pulse measured in the RD, which by chance is reconstructed with the same incoming direction as a CR event measured with the SD. To get rid of these events one can make use of the fact, that the well-known and established SD reconstruction is done prior to the RD part. Therefore, for the RdObserver v1r1 an additional functionality was implemented into the `RdEventInitializer` to take the SD shower geometry and calculate an expected signal arrival time for each individual RDS in the event. A generic search window of $-100 / +150$ ns is added around this expected signal arrival time to cover the whole duration of the emitted radio pulse even for RDS further away from the core, while significantly reducing the chance of a noise pulse to be in that region. In addition, a timing uncertainty resulting from the SD core position uncertainty is added, thus creating an event-based and direction-dependent total search window size. A general offset in the GPS timestamps between SD and RD was found in a decoupled analysis [173] and estimated to be $\Delta t_{\text{GPS}} \approx 610$ ns. This value is taken into account when estimating the expected signal arrival time for the RDS. Figure 8.1 gives a schematic overview of the new definition of the signal window.

Figure 8.2 shows a station trace for an event ($\theta \sim 45°$), once reconstructed with RdObserver v1r0 and once with the RdObserver v1r1 using the modifications mentioned before. The green shaded area indicates the signal search window for this RDS. One can see, that the window for the RdObserver v1r1 is quantitatively reduced for this station by roughly a factor 15 with the radio pulse being centered in the middle.

A top-down selection algorithm was added to the reconstruction inside the `RdTopDownStationSelector` module. It is placed in an iterative loop which also contains the `RdPlaneFit` module to perform a reconstruction after every selection step. When called for the first

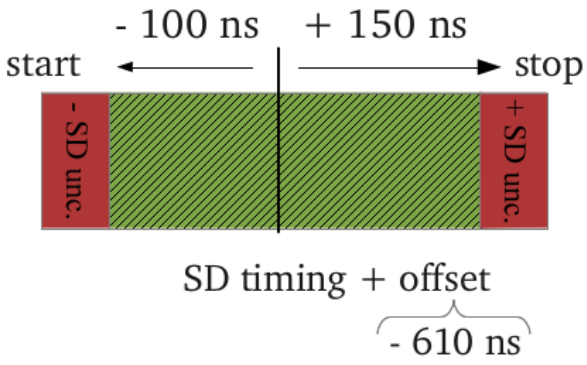

Figure 8.1: Schematic overview of the new definition of the signal window and the quantites involved.

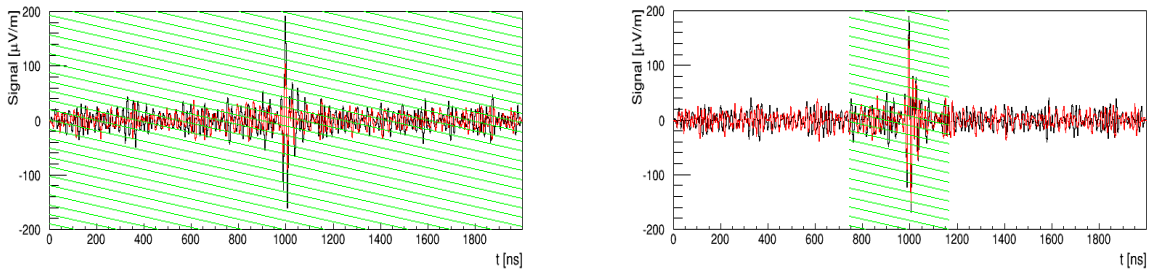

(a) **(b)**

Figure 8.2: Trace for an example event (100787.582301) from the RdObserver v1r0 (a) and v1r1 (b). The applied signal search window is shown with the green shading.

time in the module sequence, the algorithm sorts and selects the RDS of the current event according to their distance to a given reference geometry, i.e. core position and axis. In case of the RdObserver the geometry of the SD reconstruction is used as reference. Then it enables a xml-specified number of RDS for the next reconstruction step. Once this is done and the iterative loop calls the top-module for the next time it will check if the preceding fit was successful and additionally if and how the quality of the fit has changed.

Being (at least partially) externally triggered and limiting the region in the trace where to search for a signal should per definition yield a rather high purity within the pulse selection. Nevertheless, there is still a non negligable chance of having a random RFI pulse right at the point in time where you would expect a CR pulse for the corresponding event. Figure 8.3 shows two examples of transient noise in the dataset of v1r0, one with a huge difference between the reconstructed core position of SD and RD respectively, the other one with a large separation in between the individual RDS. To get rid of these events one needs another selection criteria based on clustering and positioning of stations which have a signal above the chosen SNR threshold. These two criteria have been implemented in

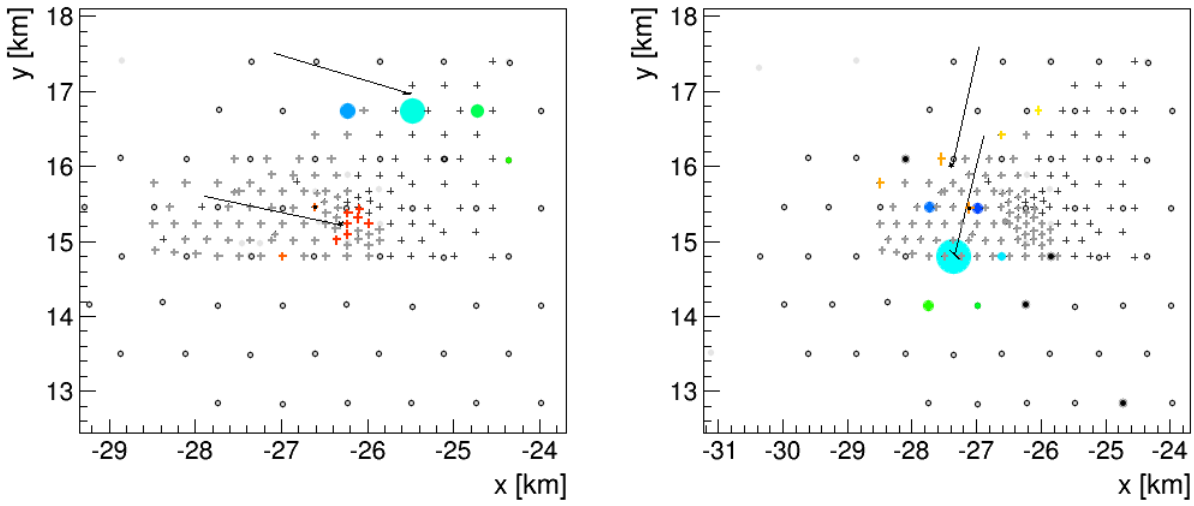

Figure 8.3: Array view for two example transient noise events with a huge difference between the SD and RD core position (a) and a huge separation between individual RDS used in the reconstruction (colored crosses) (b) from the RdObserver v1r0.

the `RdClusterFinder` module. First, an algorithm is applied to the signal stations, which forms clusters of stations according their difference in distance to the SD shower axis. This is done by looping over the distance sorted list until a maximum discontinuity is reached, which is currently set to 500 m. Using only this algorithm already yields some good results in clearance of noise events.

Nevertheless, there are specific non-physical geometries (e.g. stations in line with breaks in between), which would still pass this cut. Therefore, an additional algorithm has been implemented, which checks the geometrical distance between signal stations. This method has been adopted from the SD reconstruction, introducing the characteristic of "loneliness". A signal station is considered as lonely, if either no other signal station is in the distance of 400 m or at most one signal station is inside a radius of 800 m. These parameters have been chosen according to the 375 grid. The varying grid spacings make this algorithm not as efficient for the RD as for the SD, though.

Applying these three modifications to the reconstruction a purity of $\rho \sim 57.8$ % is reached with 108 CR candiate events in a total set of 187 events, which is already an improvement by a factor of 1.5 compared to the RdObserver v1r0.

However, due to the noisy environment with respect to RFI pulses (c.f. Section 6.5) there is still a pretty high chance of measuring an interference right at that time, where the CR pulse is expected. Thus, an additional criteria is necessary to distinguish CR events in SD

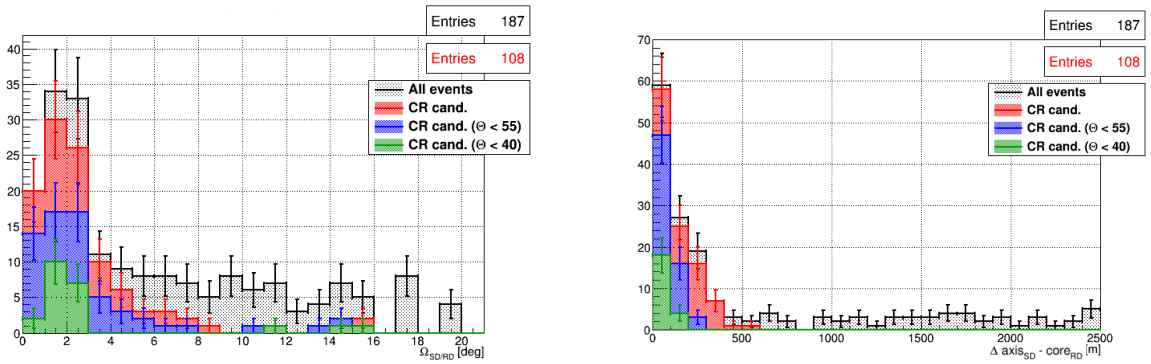

(a) **(b)**

Figure 8.4: Comparison of geometrical shower quantities for CR candidate and noise events. Angular deviation between the reconstructed direction from SD and RD (a) and the distance of the RD core from the SD axis (b). Colors indicate different zenith ranges.

and RD from coincident RD-background. This is done by checking the geometry of the shower, i.e. the deviations of the shower axes. Figure 8.4 shows the distributions for these two quantities in the dataset of January 2014. One can see, that the angular deviation does neither provide a clear separation between CR candiate and noise events nor shows any zenith dependence at all. Therefore, keeping the current cut value for the directional reconstruction of $\Omega_{\mathrm{SD/RD}} < 20°$ is a suitable choice for coincident showers.

Whereas, the difference between the reconstructed shower axis of SD and the core of RD naturally seems to be a clear indicator if an event originates from a random coincidence with a noise pulse. In the used data sample there is no CR candidate event with $\Delta_{\mathrm{axis/core}} > 600$ m. But to be on the safe side even for highly inclined showers it was decided that $\Delta_{\mathrm{axis/core}} < 2000$ m is a good measure to avoid a lot of noise events, while not throwing away CR candidates. Taking this value as a cut one reduces the dataset by 33 events, going from 187 down to 154 events in total. With 108 CR candidate events the purity in the dataset is $\rho \sim 70.1$ %. Beside that, there is a clear zenith dependence (c.f. Fig. 8.4), so the aim of a future study might be a parametrized cut with respect to the incoming direction of the shower to lower the threshold and further increase the data purity.

8.4 Timing Corrections and pulse selection

One of the major requirements for a high-quality shower reconstruction is an excellent knowledge of the position of the detector, i.e. the antenna, as well as the time when the pulse was detected. A GPS measurement campaign was performed for all 124 RDS deployed in phase II leading to a position accuracy of $\Delta_{\mathrm{RDS}} < 0.05$ m [166]. Radio signals

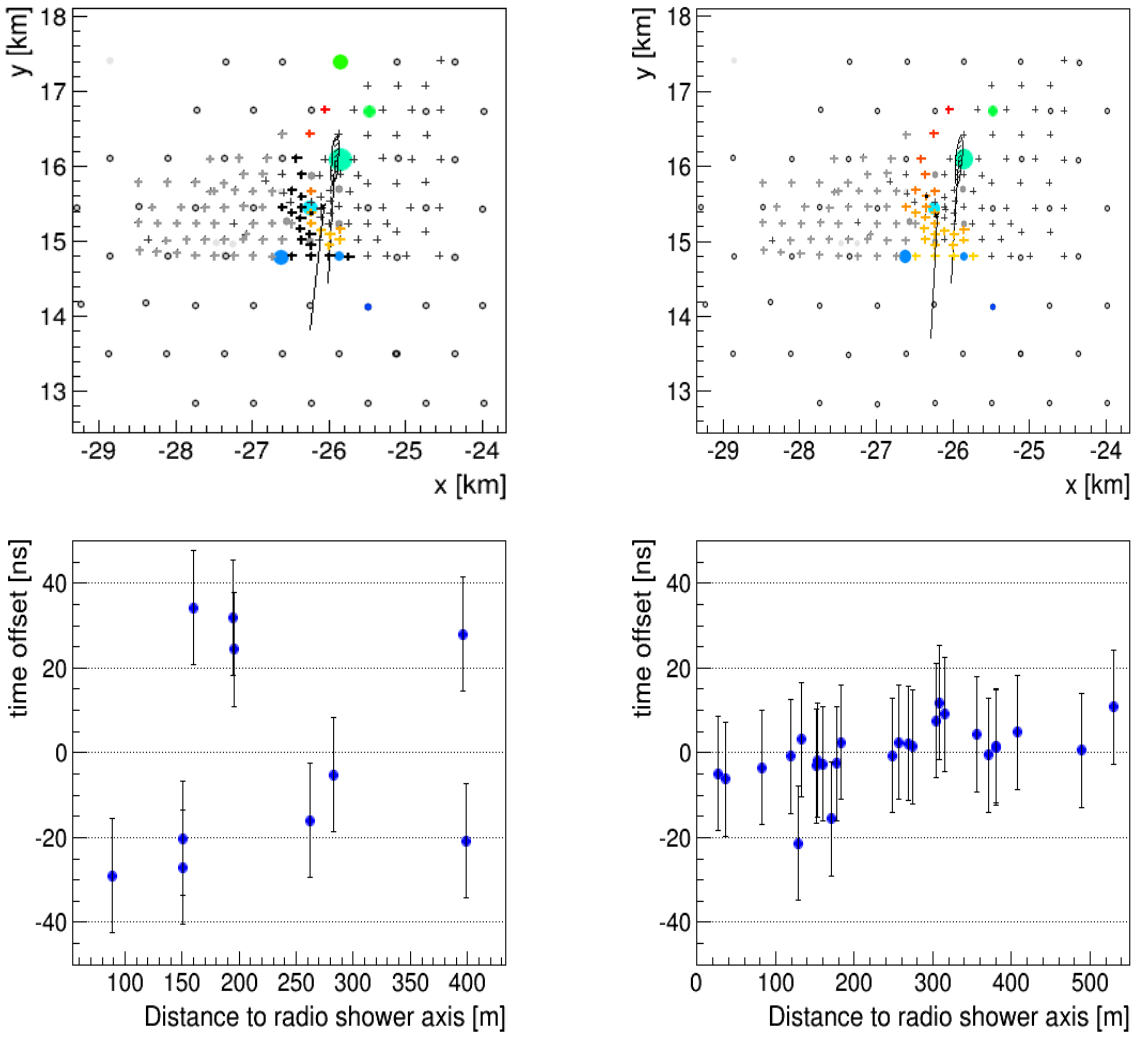

Figure 8.5: Array view (top) and fit residuals (bottom) for an example event (ID 100820.569235) from the RdObserver without (a) and with (b) the GPS and beacon corrections applied to the reconstruction.

in the design frequency of AERA emitted by airplanes are used for an absolute timing calibration of the RDS. Knowing the tracetory and time of the airplane using its transmitted ADS-B information one can calculate the offset between expected and measured signal time which then can be used to re-calibrate the timing inside the reconstruction chain [166]. Additionally a continuous relative calibration is performed using the beacon technology (c.f. Section 6.4.3). Applying these three correction methods one can achieve a significant improvement in the quality of the direction fit as well as in the mean number of stations per event. Figure 8.5 shows the EventBrowser array view and the fit residuals for an example event from the RdObserver. Applying the corrections mentioned above not only

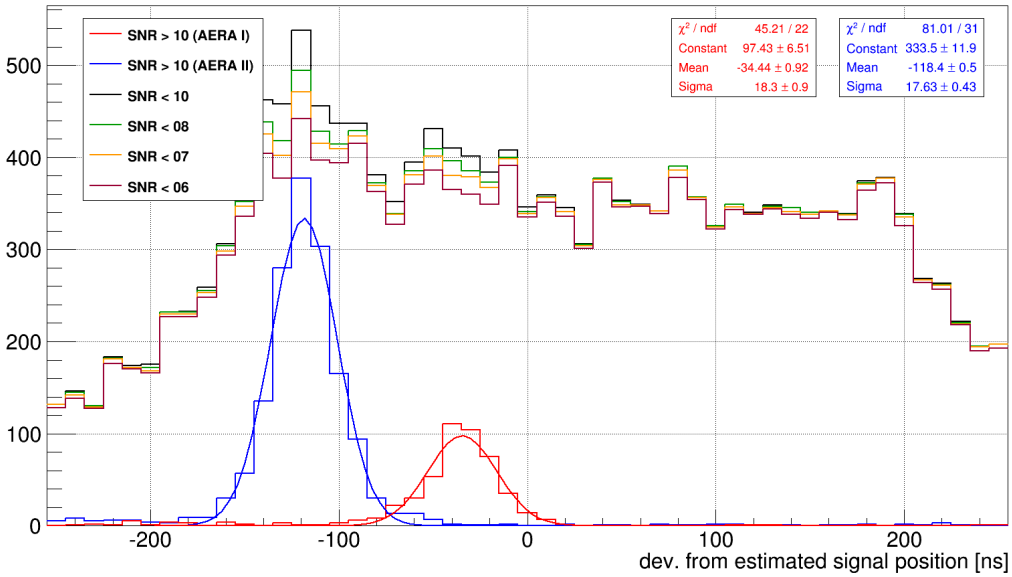

Figure 8.6: Deviation of reconstructed signal position of indivual RDS from the estimated time by the SD reconstruction. Shown are the distributions for the signal stations of phase I and phase II RDS as well as for different sub-threshold SNRs in one month of data taking with the RdObserver v1r0.

increases the number of stations used for the reconstruction from 10 to 26, but also yields a $\chi^2 \,/\, ndf = 7 \,/\, 23$ for the directional fit instead of $\chi^2 \,/\, ndf = 34.5 \,/\, 7$ beforehand. This improved quality holds for almost all the events in the dataset.

All the corrections described in this and the previous section also reflect in the total accuracy of the pulse timing and the resulting quality of the directional fit. Figure 8.6 shows the position of the selected pulse of individual RDS with respect to the estimated time from the SD in the RdObserver v1r0 reconstruction for one month of data taking. It is clearly visible that not only the pulse timings differ a lot from the estimated arrival time, but also show completly separated distributions for the two different types of RDS. For the phase I RDS a mean of $\bar{t} = -34$ ns is found, while the phase II RDS yield a deviation of $\bar{t} = -118$ ns. This separation is a result of several issues related to the RDS timing. A first and major part was related to a unit-error and therefore misinterpretation of the phase in the RDS response information for the phase I stations. This problem was fixed with the transistion to database version `AERA_2_A`, which resulted in a significantly improved agreement between the phase I and II timings. Furthermore, the absolute timing calibration among the RDS as discussed before was not yet performed.

Applying this correction as well as adding information from the GPS and beacon corrections and tuning the general offset between SD and RD (see Section 8.3) leads to an excellent agreement between estimated and measured pulse timing as shown in Fig. 8.7. Here, a mean

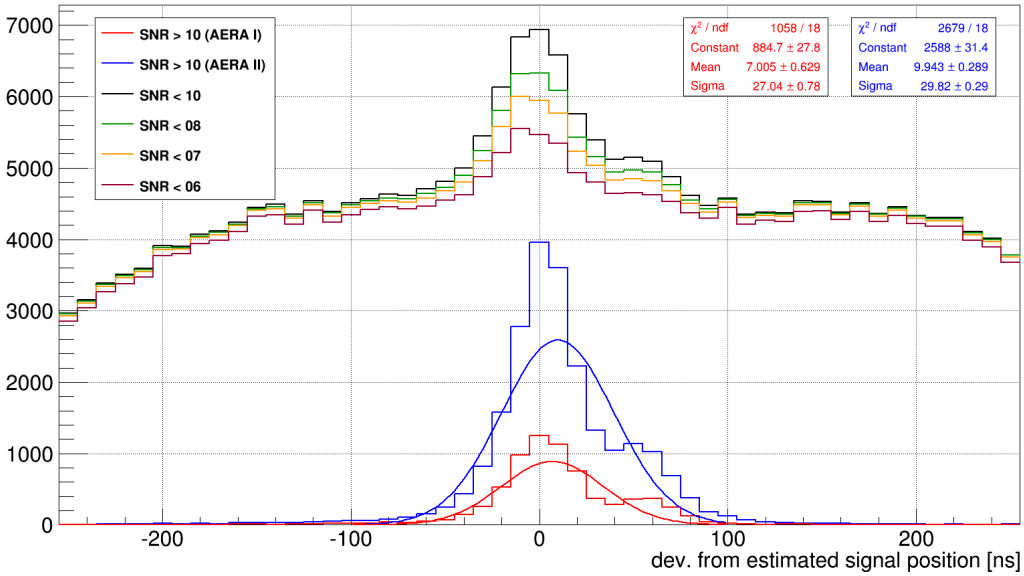

Figure 8.7: Same as 8.6, but for the full phase II dataset of the RdObserver v1r3 including all the timing corrections.

of $\bar{t} < 10$ ns is found for both types of RDS. The remaining shift is caused by a deviation from the gaussian shape at $\bar{t} \approx 50$ ns. This whole excess results from events measured in the early phase of phase II prior December 2013. Therefore, it is most likely originating from a yet unidentified change in the RDS trigger or data taking software. However, as all the RDS show the same consistent shift for this whole period, which is still inside the chosen signal search window, they will not affect the directional reconstruction for these events and thus do not have to be excluded from further analyses. When removing them for the purpose of this timing analysis, a corrected mean deviation from the signal expectation of $\bar{t} \approx 2 \pm 0.2$ ns is found.

Furthermore, the distribution of signal positions of non-signal RDS for several sub-threshold SNRs is shown in Figure 8.7. A clear excess can be seen in the signal region even for RDS down to a SNR < 6. In general, this means that by choosing a SNR > 10, potential signal stations might be cut out and therefore additional information e.g. for the directional reconstruction or the LDF fit will not be available. Figure 8.8 shows the fractional increase in the number of RDS for the transition between different SNRs for the full RdObserver v1r3 phase II dataset. Here, the reduced dataset as mentioned above is used to provide a clearer picture. As can be seen a gain of roughly 10% can be achieved in the region around the estimated signal time by solely decreasing the SNR from 10 to 8. If even reduced to a SNR < 6 a gain of almost 25% would be possible. However, despite increasing the chance of adding further signal stations, this also rises the probability of catching a random coincidence of a noise pulse. Therefore, the currently chosen selection of SNR > 10 will be

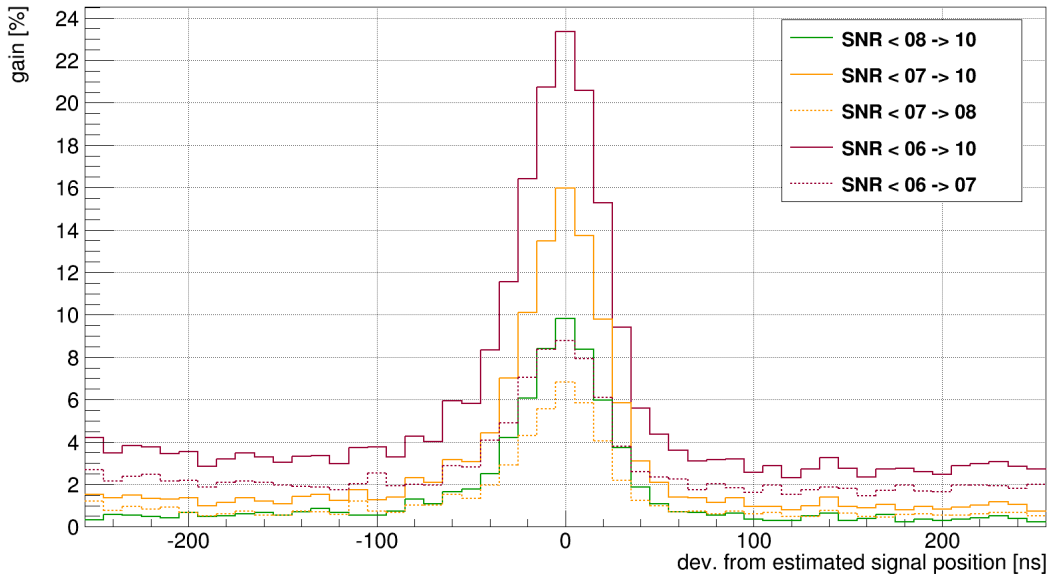

Figure 8.8: Percentaged gain in number of useable RDS for different SNRs in the full RdObserver v1r3 phase II dataset.

kept until this issue has been studied to greater detail. In addition, the obtained results show that there is potential to decrease the signal search window even further.

As already discussed the applied antenna pattern, which currently results from simulations, is an important parameter also for the timing accuracy. Beside the general influence of its uncertainties also directional effects may come into play here. Figure 8.9 shows the deviation from the estimated signal position for the phase I and II RDS in the reduced RdObserver v1r3 dataset subdivided by the azimuthal arrival direction of the event. While the phase I RDS show only a minor discrepancy of $|\bar{t}| < 4$ ns among the different directions, a larger deviation can be found for the phase II RDS. Here, a deviation of $\bar{t} = -12$ ns is found for events coming from the North ($67.5° < \phi < 112.5°$), which shifts to $\bar{t} = +5$ ns for events arriving from the South. A possible explanation beside the different antenna types could be the electronics box, which is directly attached to the antenna pole for AERA II RDS and is oriented to the magnetic North. It was shown, that the electronics box has a significant influence on the antenna pattern, which might still not be fully covered by the simulations [117]. Furthermore, also physical processes originating from the different emission mechanisms, which have a varying strength with respect to the shower arrival direction, might result in a shift in the arrival time of the radio emission in contrast to the shower particles. However, this effect will not be able to explain the full difference of deviations and should especially be measured consistently with both types of RDS. Although, the total impact of this issue should be of minor importance for the current reconstruction and adjacent analyses, it should be kept in mind and re-checked as soon as field calibration data for the individual RDS become available.

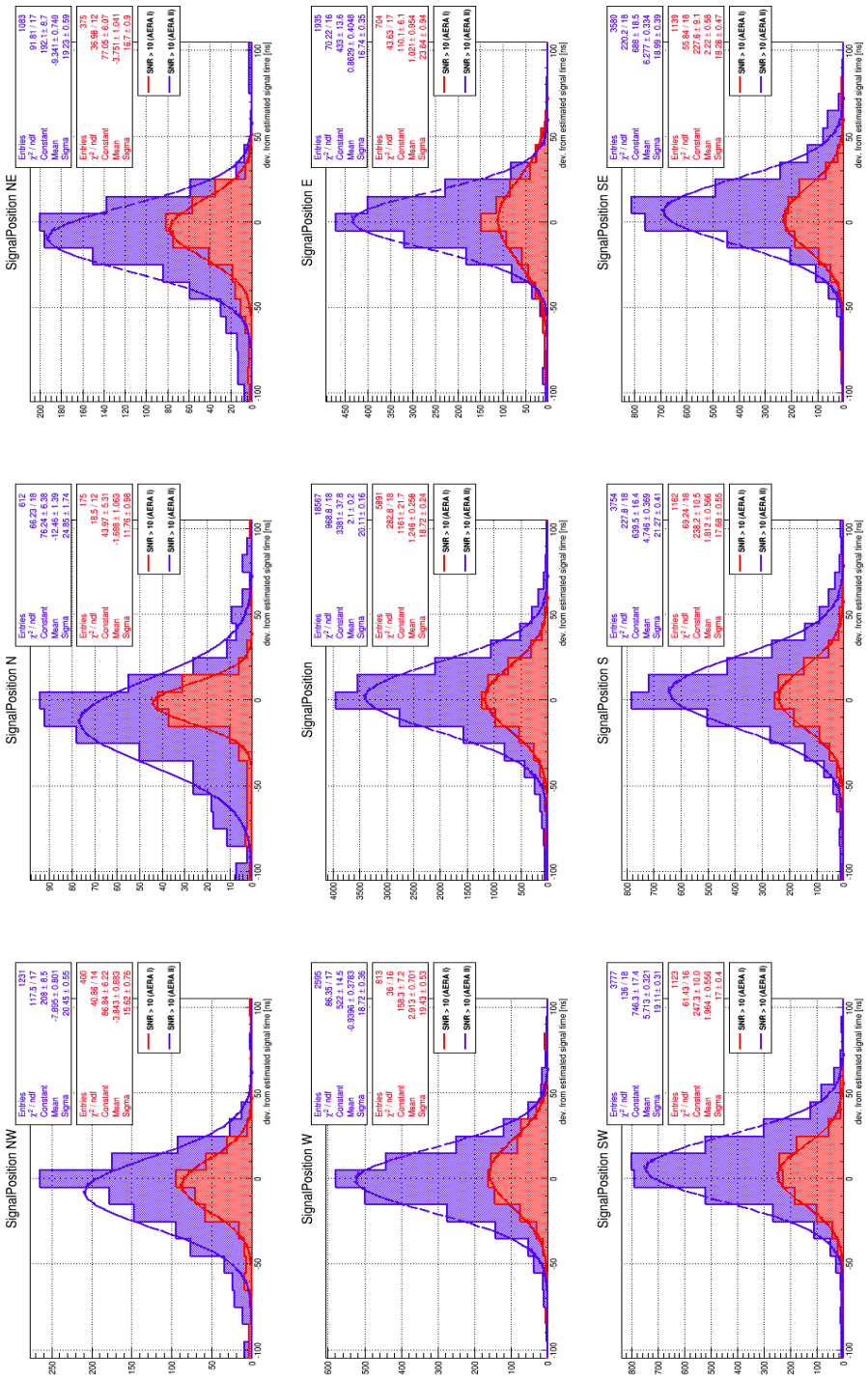

Figure 8.9: Deviation from the estimated signal position of individual RDS in the reduced RdObserver v1r3 phase II dataset for different azimuthal arrival directions. Center shows cumulative distribution.

8.5 RFI Suppression

As already mentioned before, the environment of AERA, although deployed in a rural area, is not completly radio-quiet and therefore the measured traces suffer from RFI pulses even if they contain a real CR pulse. This makes an efficient RFI suppression mandatory. Beside the efforts already realized in the RDS hardware also inside of Offline several methods to suppress RFI have been implemented. Nevertheless, some very promising approaches like a sine-wave suppression for mono-frequent interferences have shown to work very well, but also to be very time-consuming. This makes them, at least with the current data rate, not sufficient for an application in the daily production of the RdObserver.

The `RdChannelBandstopFilter` module is used to cut away the beacon frequencies after the timing corrections have been applied. Collecting the information on the frequencies

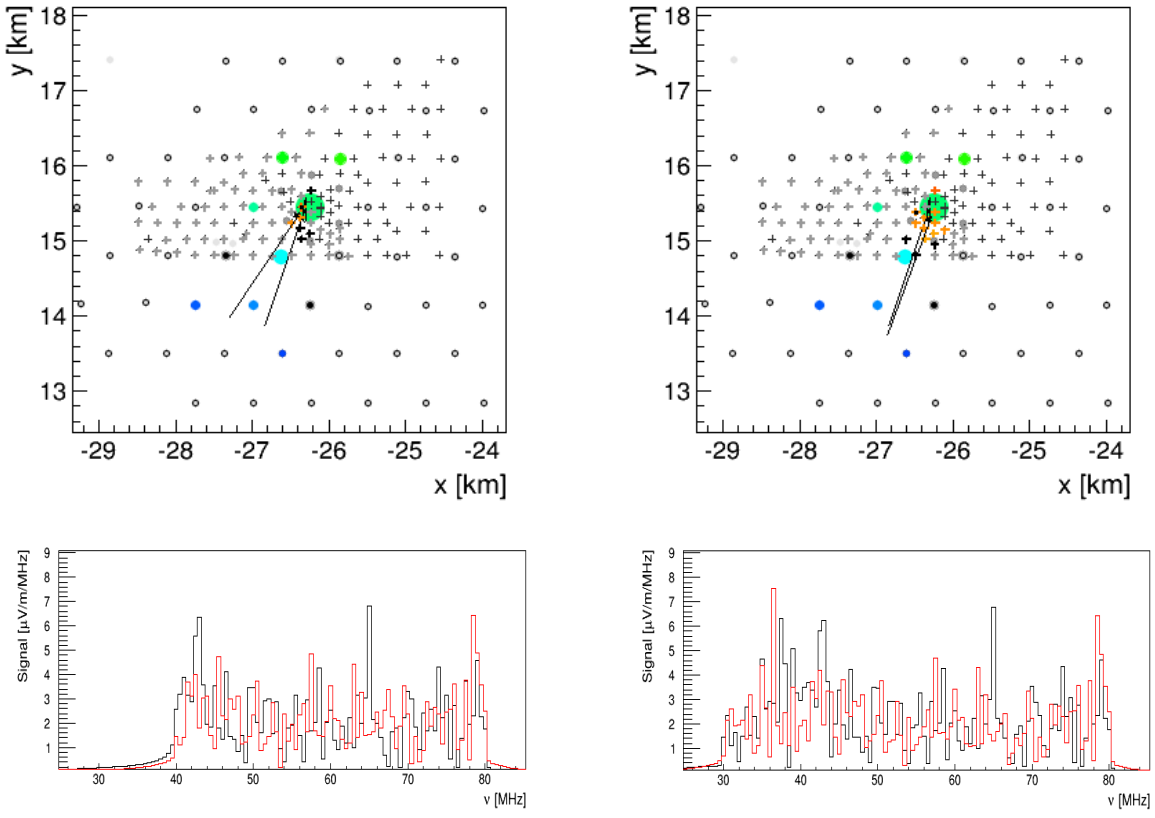

Figure 8.10: Array view (top) and spectrum of RDS # 15 (bottom) for an example event (ID 100820.534078) from the RdObserver with the fixed (a) and the online (b) bandstop filter algorithm applied to the reconstruction.

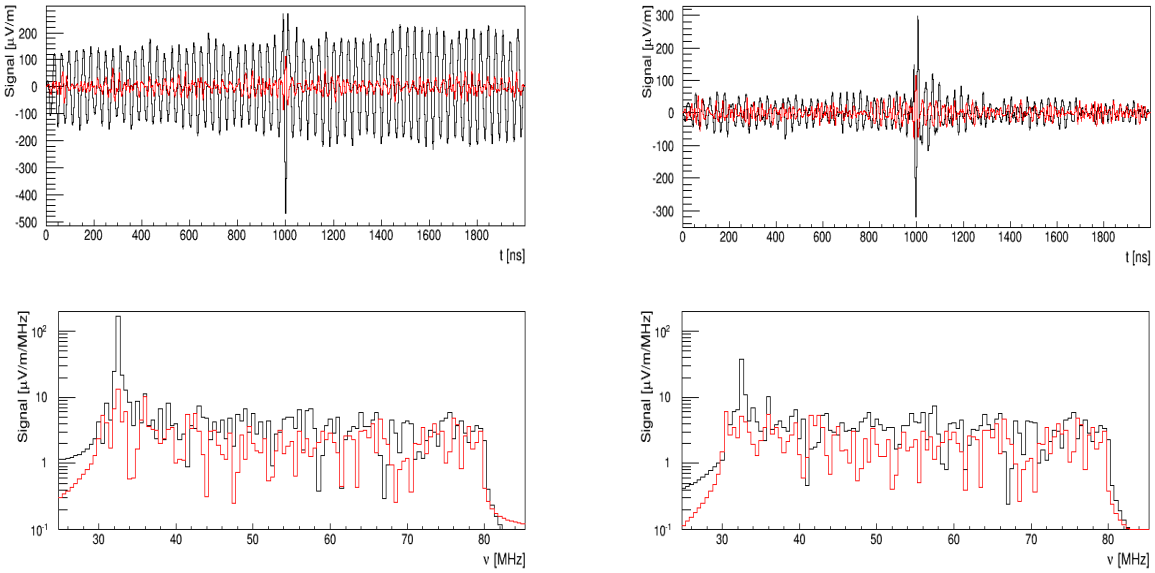

Figure 8.11: Trace (top) and spectrum (bottom) of RDS AERA 019 for an example event (ID 100816.101300) from the RdObserver without (a) and with (b) the online bandstop filter algorithm applied to the reconstruction.

either from the database or from the xml configuration, it sets the corresponding bins in the RDS spectrum to zero. Therefore, one could also use this module for the removal of RFI, but a problem arises from this consideration. The occuring RFI are neither constant in time nor in frequency, so a fixed bandstop filter would have to cut away a large band of the design frequency for a long period of time to achieve a successful removal. This would lead to significant modification of the radio pulse in the time series of the RDS trace, which then can influence the directional reconstruction.

Therefore, a rather simple algorithm was implemented into the same module to dynamically distinguish and cut RFI in the frequency domain of the trace. As the frequency spectrum of a CR pulse is expected to be rather flat in the design frequency of AERA from 30 to 80 MHz every other contribution yielding a significant peak is very likely coming from RFI. The module takes the frequency spectrum for each channel trace of each RDS available in the current event and calculates a statistical benchmark (median (default) or mean) of it. Afterwards, it checks if the actual value of one frequency bin exceeds the calculated benchmark by a user-defined deviation and if so, sets the corresponding bin to zero, i.e. applying a kind of online bandstop filter. Even if several noise pulses are contained in the trace of one event, each of them is only located in a very narrow band of the frequency spectrum. Therefore, cutting away these few bins will not destroy the shape of the pulse or modify the reconstructed pulse power of the cosmic ray signal by a significant amount.

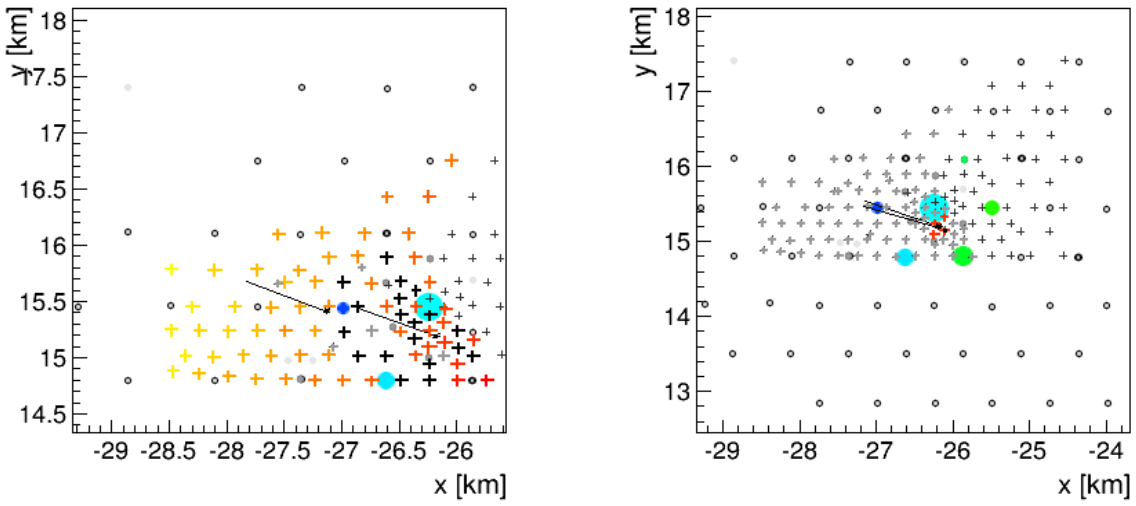

Figure 8.12: Array view for an example event (ID 100816.101300) from the RdObserver without (a) and with (b) the online bandstop filter algorithm applied to the reconstruction.

Figure 8.10 shows the array view and the spectra of a specific RDS for an example event from the RdObserver, which contained a large RFI contribution in the regime between 30 to 40 MHz. One can see that using the online bandstop filter improves the accuracy of the reconstruction as well as increases the number of stations which are used for the directional reconstruction. Additionally, that the spectrum in the signal region can be conserved, while all the information would be lost for a fixed bandstop filter.

Additionally, several events were found, which have a very strong RFI pulse inside the trace causing it to dominate the direction reconstruction. As the direction of the noise pulse is randomly coinciding with the SD event, which triggered the radio readout, it will also pass the post selection criteria. Nevertheless, those events would be thrown away in a high quality selection although they contain a real CR pulse. Figure 8.11 shows the traces and spectra for one of these events which could be recovered. When no suppression is used, there is a clearly visible superposition of a sinusoidal RFI moving over the array and sitting on top of the CR pulse. Note, that the trace shown is measured with the RDS closest to the core, so the real signal will get buried in the increased noise level when moving further outwards. When the online bandstop filter algorithm is applied, the RFI is more or less completly removed from the trace and the CR pulse is reconstructed. This is even more clearly in the array view in Fig. 8.12 showing that now only stations around the shower core are used, while before the whole array was illuminated. The recovery of events is also reflected in an increased purity of $\rho \sim 80.1$ %, from 113 CR candidate events within a total dataset of 141 events.

8.6 Results from RdObserver v1r3

A first, complete reconstruction of the full set of data measured with the externally triggered RDS in phase II was performed with the RdObserver v1r3. The considered period of data taking starts 4th June 2013 going up to 2nd March 2015 yielding a total of 5303 reconstructed events. Figure 8.13 shows the development of the number of reconstructed events for the full set, which to some extend also can be interpreted as uptime of the detector. As can be seen, most of the measurement time yields a rather constant rate on the order of ten events per day, which will be discussed later. The holes in the distribution are caused by different reasons. On the one hand, down-times of the RD DAQ due to power-cuts at the Coihueco FD or due to maintenance work leads to a lack of data. On the other hand, also the SD experienced some problems due to power or communciation issues, which are not necessarily correlated in time to the RD ones. Thus, no data is available for the merging process and no reconstruction can be performed. In general, these periods, especially the ones related to power-cuts, are on the order of 1-2 days, however some down-times lasted for almost one week. Beside that, several days are found, which show an increased number of successfully reconstructed events up to more than 40 events per day. This excess is most likely caused by strong, atmospheric electric fields, which will increase the amount of radiation emitted by the air shower and therefore the detection efficiency. This effect will be discussed in greater detail in Chapter 9.

In the following some basic plots will give an overview of the main shower and station quantities in the dataset and their meaning and possible further improvements will be discussed. Figure 8.14a shows the position of the shower core estimated by the SD reconstruction. The dashed line indicates roughly the area of the externally triggered RDS, the red star marks the position of the CRS. Clearly visible is an excess of events in the region of AERA24 due to the higher acceptance for air showers with lower energies in the denser grid. Beside that the expected almost flat distribution for the whole array is found, which falls off at the borders. As discussed in Section 7.2 there are two modules, which perform a fit of the core position for the radio data. However, both methods are limited in some way. While the barycenter calculation only gives a crude estimation and is insensitive to shower cores outside the geometry of the participating stations, the fit using the two-dimensional LDF can only be performed for events with five or more RDS, which does not hold for a large fraction of events. For the moment the SD calculation should yield the more reliable estimator for the core position.

The angular distribution of the measured events is shown as a skymap in Fig. 8.14b with the direction of the magnetic field vector noted as black star. East corresponds to an azimuth angle of $\phi = 0°$ going counter-clockwise from there on. The radial axis shows the zenith range from $\theta = 0°$ (center) to $\theta = 90°$ (outside). The resulting plot is an overlay of three effects. First, the dominance of the geomagnetic emission process leads to a signifcant North-South asymmetry of the incoming shower direction with a maximum at $\phi = 270°$.

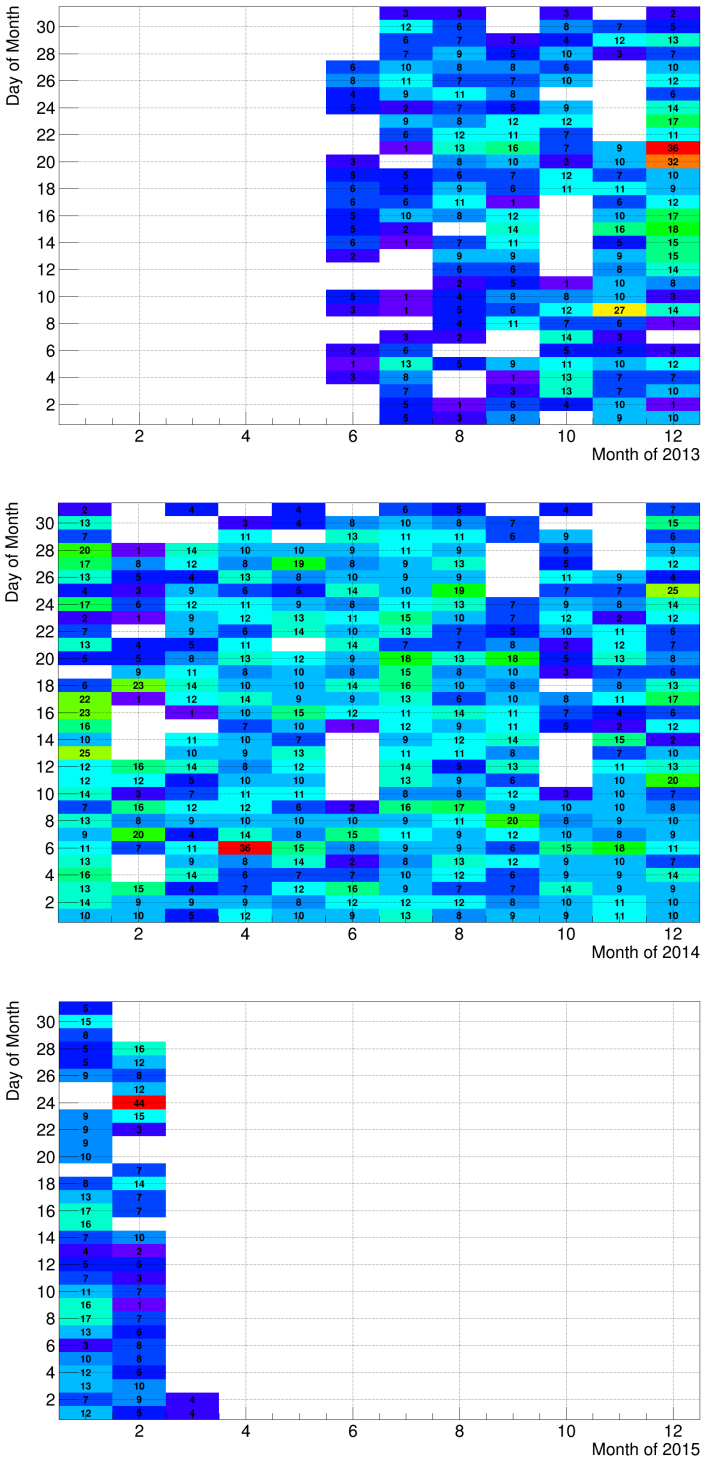

Figure 8.13: Yearly maps (2013-2015) of the rate of reconstructed events for the full RdObserver v1r3 dataset.

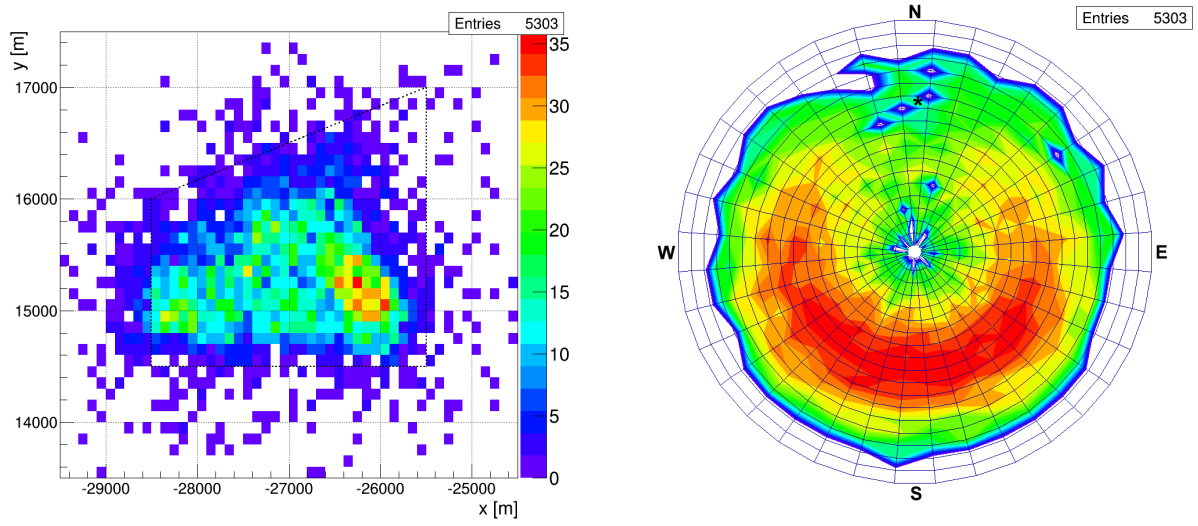

(a) **(b)**

Figure 8.14: SD core positions (a) and RD arrival directions (b) in the RdObserver v1r3 dataset.

Additionally, a radial fall-off can be observed for higher zenith angles, which originates from the loss of sensitivity towards the horizon due to the antenna gain pattern, while for vertical events the smaller footprint increases the energy threshold.

The orthogonal distance between the shower axis determined by the SD and the RD core position is shown in Fig. 8.15a and shows a good agreement of the directional reconstructions. An exponential function is fitted to the data, which can describe the distribution quite well up to distances of $\Delta \sim 800$ m. As already discussed in Section 8.3 there is still a small zenith dependence for this parameter, which might lead to some outliers above 1000 m. Apart from that the majority of events above that value are most likely random coincidences of SD with a noise pulse measured in the RD. Figure 8.15b shows the angular deviation between the directional reconstruction of the RD and the SD. Fitting a rayleigh distribution yields an expectation value of $\langle \Omega_{\mathrm{SD/RD}} \rangle = \sigma \cdot \sqrt{\pi/2} \approx 0.85°$.

The shower energy measured reconstructed from the individual detectors is plotted in Fig. 8.16a. Due to the lower grid spacing in the Infill array the energy distribution of the SD starts already at $\sim 10^{16.5}$ eV and reaches its maximum at $10^{17.5}$ eV, which is the point of 100% trigger efficiency. The measurements by the FD show the same shape, but are of course limited in statistics by the 10% duty cycle of the detector. The selected data sample requires a successful SD reconstruction. A sample requiring only FD and RD reconstruction might result in a different energy distribution. This would require major changes in the reconstruction chain, though. The shower energy for the RDS calculated from the radiated energy determined by the two-dimenstion LDF fit using Eq. 4.32 also agrees in the general

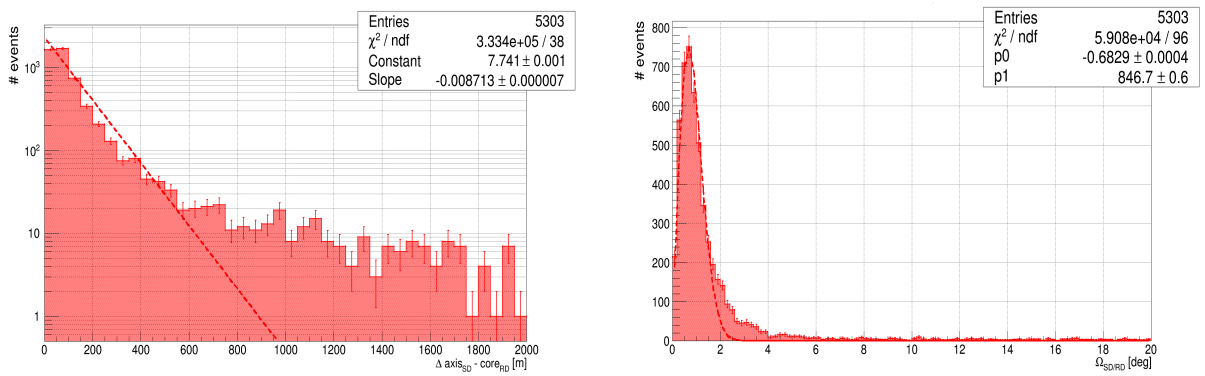

(a) **(b)**

Figure 8.15: Distance between SD shower axis and RD core position (a) and angular deviation between SD and RD shower axis (b) in the RdObserver v1r3 dataset.

form, but shows some additional features at both ends of the distribution. The lack of events in the regime below 10^{17} eV as well as the slight offset with respect to the SD in the next decade of energy might both be accounted to the uncertainties on the LFD fit of the RD. For events with less than five RDS, which will be the major part at the lowest energies, the fit shows a rather poor quality and thus also the derived energy quantities lack accuracy. In addition, the distribution for the RD extends much further to higher energies up to almost 10^{20} eV. Also this can be a result of some not successful fitting approaches, but might at least partiallly be related to an increase of the radio emission due to the influece of atmospheric conditions, which will be discussed in the next chapter. The highest currently measured coincedent event has an energy of $E_{\mathrm{SD}} = 3.23 \pm 0.10 \pm 0.29 \times 10^{19}$ eV.

Finally, Fig. 8.16b shows the number of events per day measured with the externally triggered RDS in coincidence with the SD. Fitting a Gaussian function a mean value of 9.3 events per day is found. However, this distribution is influenced by two effects. On the one hand, the entries in the histrogram are not weighted by measurement time per day. Thus, days where the RD array was not measuring for the full 24 hours will shift the mean to lower values. On the other hand, as already stated above, abnormal atmospheric electric field conditions, e.g. during thunderstorms, will mostly lead to an increased sensitivity for the detection of radio emission from air showers with lower energies and thus to an increased number of events. With both effects going into opposite directions, it is assumed without further calculations that the determined mean value is a good measure within the given uncertainties for the event rate of the externally triggered RDS.

Figure 8.17 shows some impressions for an example event of the full RdObserver v1r3 dataset. All these informations are directly accessable from the ADST files and can be viewed in the EventBrowser. The event was reconstructed with a shower energy of $E_{\mathrm{SD}} = 3.32 \pm 0.21 \pm 0.20 \times 10^{18}$ eV, an arrival direction of $(\theta, \phi)_{\mathrm{RD}} = (58.5°, 197.1°)$

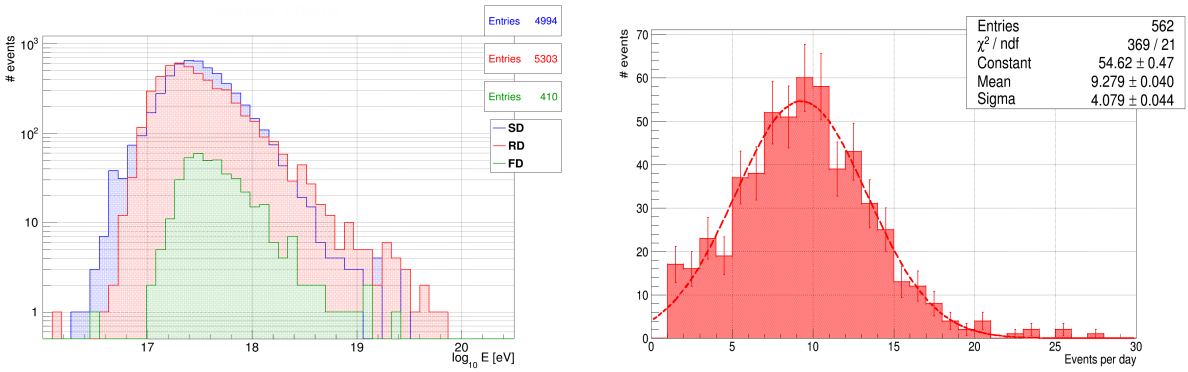

(a) **(b)**

Figure 8.16: Shower energy for the different detectors (a) and number of RD events per day (b) in the RdObserver v1r3 dataset.

and a core position in the central region of the antenna array. A total of 37 RDS have measured a signal above the SNR threshold as can be seen in the array view (top, left). The color-coding of the RDS (crosses) and SDS (circles) indicates the arrival time of the signal (c.f. Fig. 3.7) as the air shower moves across the array. The fitted two-dimensional radio LDF (top, right) is depicted in the $\vec{v} \times \vec{B}$- and $\vec{v} \times (\vec{v} \times \vec{B})$-frame for a better representation of the double gaussian shape (c.f. Fig. 4.14) and the measured amplitudes of the individual RDS (circles) are in nice agreement with the fit. The trace (bottom, left) of RDS # 57, which is the closest one to the shower core, shows a signal peak with an amplitude of roughly 1000 µV/m in both horizontal polarizations. The corresponding spectrum (bottom, right) yields the expected flat behaviour throughout the whole design frequency. The dip around 67 MHz in the East-West polarization (black) is caused by the constant removal of a well-known RFI source by the `RdChannelBandstopFilter` in a band of roughly 2 MHz.

8.7 Planned improvements

As shown in the last sections the RdObserver has reached a very good level of event selection efficiency and purity, which resulted in the first complete coincident dataset for AERA. Nevertheless, several things still need to be implemented and modified to further improve the reconstruction quality.

- *cut on β-angle*: As discussed in Section 7.2 up to now a rather conservative cut on the angle between the measured and the expected electric field vector at a given station of $\beta < 55°$ is applied during the reconstruction. This value is neither very restrictive nor physically relevant with the current accurate knowledge of the charge excess fraction at the measurement site. Figure 8.18 shows the distribution of β for

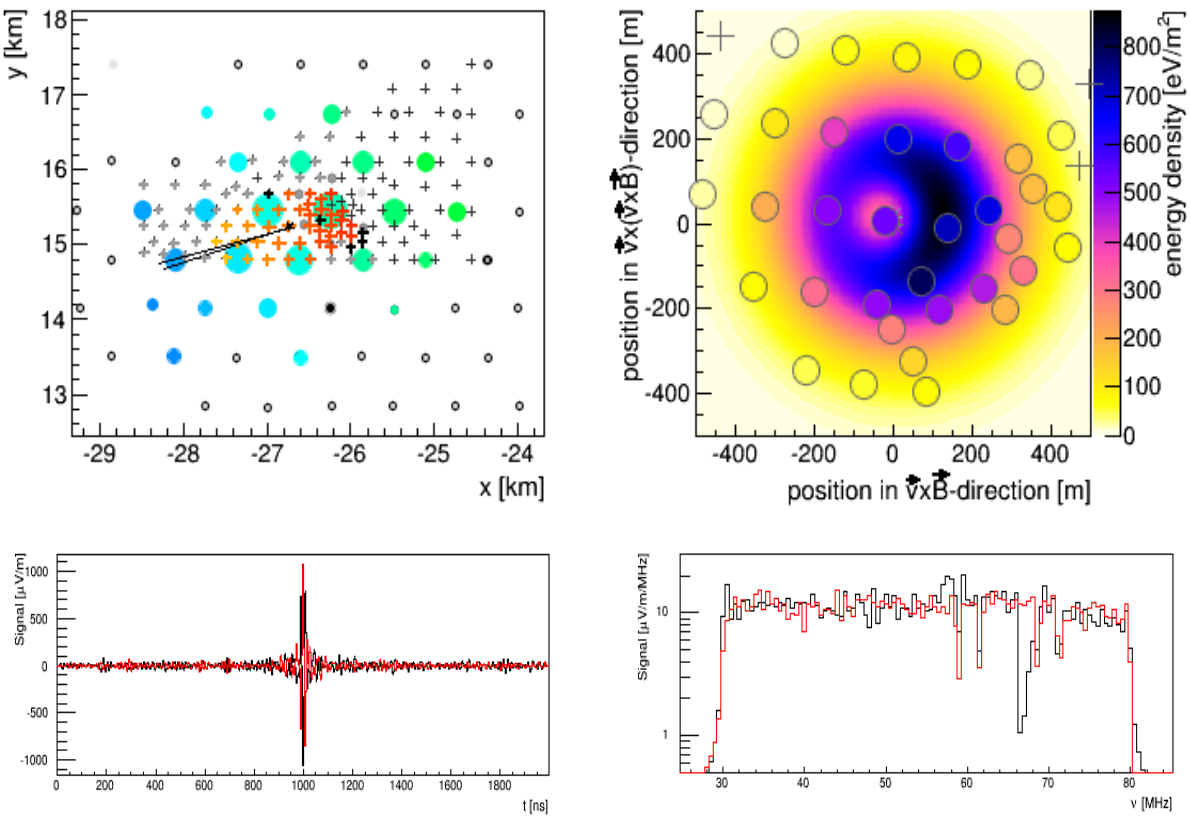

Figure 8.17: Array view (top, left), two-dimensional LDF (top, right), trace of RDS # 57 (bottom, left) and spectrum of RDS # 57 (bottom, right) for an example event (ID 100743.33468) from the RdObserver v1r3 dataset.

the RdObserver v1r3 dataset. Already with the current reconstruction almost 80% of the selected RDS have $\beta < 20°$ and thus a more strict cut around this value should improve the dataset. Nevertheless, due to the continuous distribution of angles a detailed and probably more refined analysis and selection is necessary. A deviation from the expected emission behaviour caused e.g. by varying atmospheric conditions as discussed in Chapter 9 is expected. Analysing these events requires a released cut on β.

- *coincidence criteria:* The same conservative approach has yet been applied for the classification of a "coincident" event of the RD and the SD. As discussed in Section 8.3 there is still room to further tighten up both criteria, angular deviation and axis-core distance, maybe with addititional modifications like a zenith dependent treatment.

- *hyperbolic wave fit:* The wavefront of the radio emission was found to be best described by a hyperbola as discussed in Section 4.1. Up to now a plane wave fit is performed in the RdObserver as none of the previously trialed enhanced descriptions, spherical

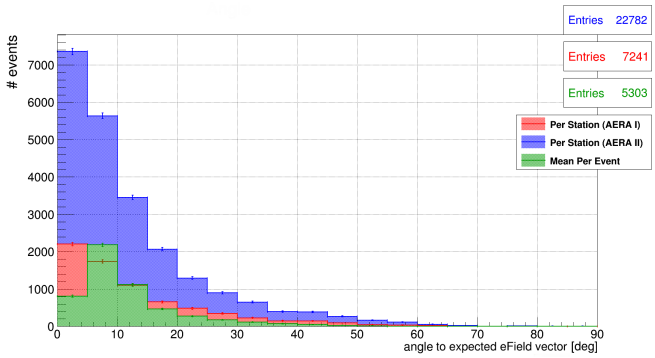

Figure 8.18: Calculation of the angle between the measured and the expected electric field vector for a charge-excess fraction of $a = 14\%$ with the RdObserver v1r3 dataset. Shown are the distributions for individual stations of the different phases as well as the mean per event.

or conical, succeeded to match the data to a fair amount. Thus, after a sufficient parametrization is found and tested this new model will be used for the directional fit process. This should not only increase the accurcy of the direction reconstruction, but will improve many other parameters and analysis as well as it is used as input there.

- *bad period and weather database:* The operation of a highly complex detector always yields the possibilty for a malfunctioning of some components like the station electronics, the communication or the antenna itself, which would require a special treatment for data coming from the affected stations or even a full rejection. To be able to deal with this already during the reconstruction a special database for the storage of those so-called "bad periods" is under development. Additionally, an interface to use the information collected by the two weather stations in the RD array is needed to provide a further tool for the recognition of non-standard data taking periods.

- *reconstruction for inclined events:* As presented e.g. in [174] the footprint for inclined air showers ($\theta > 70°$) can become very large even in the lower energy regime. To cope with the special requirements for the interpretation of those showers like a modified two-dimensional LDF a horizontal reconstruction is currently under development and will be used for the first full processing of the new AERA149 data.

- *merging of externally and scintillator triggered stations:* Up to now the RdObserver has only been optimized for the externally triggered RDS of AERA. Nevertheless, also a huge amount of data has been collected with the scintillator triggered stations in the eastern part of the array. Thus, efforts are underway to merge these two datasets which will significantly increase the number of events available for reconstruction. Nevertheless, a lot of detailed analysis needs to be performed to achieve this goal like

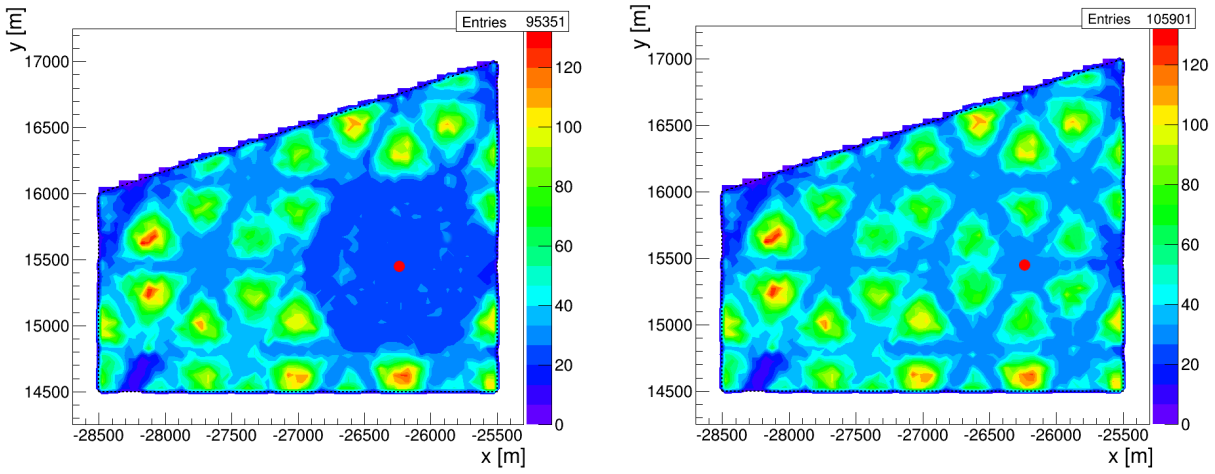

(a) **(b)**

Figure 8.19: Distribution of core positions for the SD-Infill reconstruction before (a) and after (b) the trigger correction. The red dot indicates the position of the tank 'Kathy Turner', which is part of the Infill as well as of the AERAlet.

developing a method for the cross-calibration of timing as well as amplitude of the two different RDS types.

8.8 Analysis Sidekicks

While checking the data for the improvement of the RdObserver reconstruction, also two non radio-related issues were found and investigated. They will be discussed very briefly in this section:

- **AERAlet trigger:** As discussed in Section 6.4.1 another trigger was implemented, which can force the read-out of the externally triggered RDS independently of the standard SD by a trigger coming from the AERAlet, a hexagon of SDS on a 433 m grid inside the antenna array. Unfortunately this forced some problems inside the merging procedure of the CDAS when events were triggered by both configurations, the AERAlet as well as the normal SD. In that case, the AERAlet trigger was handled earlier due to the communcication via the optical fiber instead of the wireless comms. The data were not longer available to be incorporated in the standard data stream. This lead to a signifcant lack of events in that region, which can be seen e.g. in the distribution of reconstructed core positions as shown in Fig. 8.19a. After noticing, this issue could be fixed and the data for this period of time have been remerged to include also the AERAlet SDS. The new data-set now shows the expected core

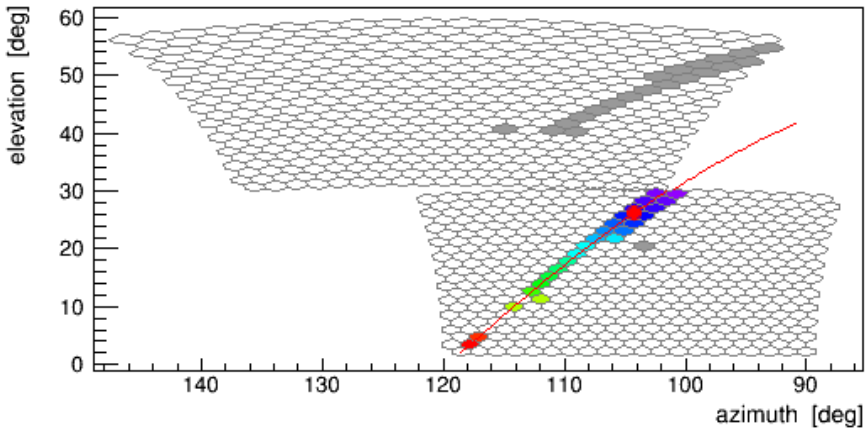

Figure 8.20: Camera view of the combined FD-HEAT reconstruction for an event with the wrong tilt-mode monitoring.

distribution as shown in Fig. 8.19b. Note that the inhomogeneity is caused by the increased trigger efficiency in the middle of the triangles formed by the SDS.

- **HEAT tilt monitoring:** For the FD shift from end of February to beginning of March 2014 the FD-HEAT reconstruction showed some strange patterns in the camera view of Coihueco and HEAT. This means that the triggered pixels did not form a continuous track for the combined virtual-eye, but were more likely duplicated in the HEAT eye. It was found, that for this shift the HEAT telescope buildings were operated in *down* mode, but due to a bug in the event building were interpreted as looking *up*. Figure 8.20 shows an example event, which is influenced by this problem. Therefore, HEAT data for this period should not be used for analysis until corrected.

CHAPTER 9

Radio Emission in Strong Atmospheric Electric Fields

9.1 Motivation

On the way towards being a true alternative to the mature detection methods of cosmic rays, the radio technique has to be carefully studied with respect to possible influences regarding the determination of the relevant shower parameters like depth of the shower maximum, arrival direction or shower energy. Especially for the latter one, which is normally directly connected to the amount of radio emission, the atmospheric electric field can have a huge influence as discussed in Section 4.5. It was already shown by LOPES measurements [131] as well as by detailed REAS simulations [101] that this effect is indeed very well measurable.

Additionally, due to the superposition of the different particle responses to the magnetic and the electric field during the shower development, a change in the polarization pattern of the emission is expected. Figure 9.1 shows the different influence of the corresponding forces. In case of a horizontal magnetic field in North-South direction and a vertical electric field in z direction, an observer on the East-West axis can not distinguish between the type of field as for the deflection for both will be perpendicular to the EW-z plane and the emission will be polarized in that plane. In constrast, an observer on the North-South axis will measure a polarization parallel to the East-West axis for the magnetic field case, while in an electric

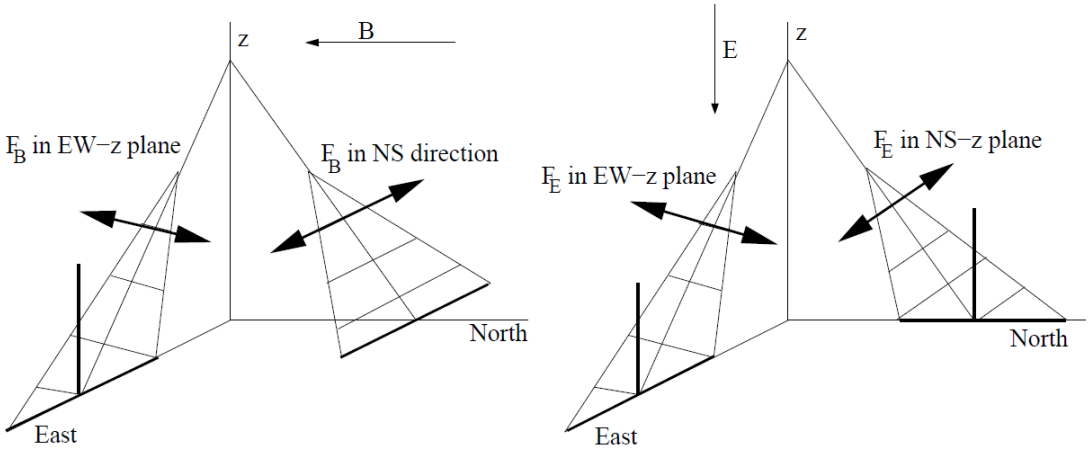

Figure 9.1: Schematic view of the direction of the magnetic (left) and electric (right) force and their influence on the polarization properties. Particle deflection is indicated by the arrows, the thick lines represent the pulse polarization. From [101].

field the pulse will be polarized in the NS-z plane. Thus, for emission created in both fields, the resulting contributions will appear in different polariation directions [101].

Furthermore, the general polarization pattern will be altered as a result of the charge-excess in the shower. In the presence of a strong electric field, this excess respectively the spatial separation can be massively increased, which will lead to a significant change in the amount of radially polarized emission. This effect has recently been confirmed by simulations and measurements by LOFAR [175].

In this chapter, an analysis of the intensity and the polarization of radio emission measured with AERA during strong atmospheric electric fields will be presented. First, the selection criteria will be explained, which are applied to the different datasets to achieve a sufficient data quality. Then the general atmospheric situation at the AERA site will be investigated using ground measurements of the two weather stations to derive characteristics for strong fields. The varying intensity of the emission is studied by a comparison of the reconstructed radio energy with the shower energy reconstructed by the SD as well as the radio energy from CoREAS simulations. The same simulations are used for the study of polarization patterns in comparison to those in the measured data afterwards. Finally, the results of dedicated simulations of single events recorded during strong field including an atmospheric electric field will be shown.

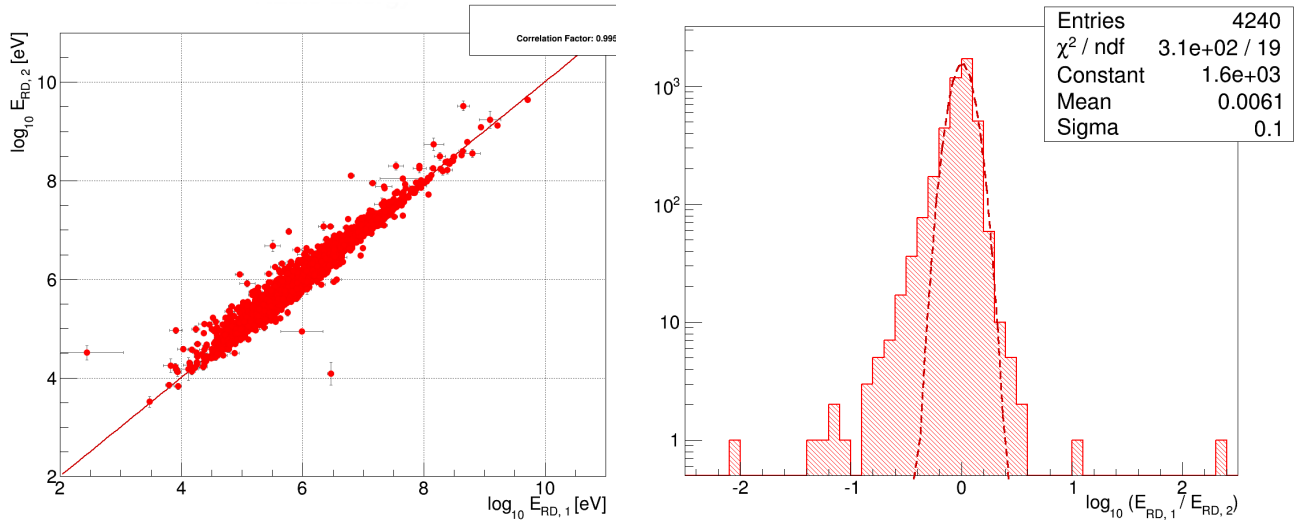

(a) (b)

Figure 9.2: Comparison of the estimated radio energy for proton and iron simulations. Correlation plot (a) and ratio with gaussian fit (b).

9.2 Data Selection

For this analysis the whole set of data taken with the externally triggered setup of AERA from the 4th June 2013 up to the 2nd March 2015 is used. They have been reconstructed with the RdObserver v1r3 applying the basic selection criteria described in Section 8.3 yielding a set of 5303 events. Some plots showing the basic parameters of this dataset have been presented in Section 8.6. This sample will be refered to as measured dataset.

All events were additionally simulated with CORSIKA 7.400 [77] using the hadronic interaction models FLUKA 2011.2b [176] (low energy) and QGSJETII-04 [42] (high energy). A particle thinning factor of 10^{-6} was applied and the CoREAS plugin [109] was used for the generation of the radio emission. The simulated shower parameters core, direction and energy were taken from the SD reconstruction of the corresponding event. Two full shower simulations were performed, one with a proton and one with an iron nuclei as primary particle. The iron simulations were done with a particle tracking (i.e. e^+ and e^-) down to kinetic energies of 150 keV. For the proton simulation a cut on the single particle energy of 511 keV, which corresponds to a Lorentz factor of $\gamma = 2$, was applied. To estimate the influence of this cut a smaller subset of the iron simulations were re-done with the same setting and some first tests have shown that signal amplitudes are less than 5% lower when using the γ-cut [177].

These simulated events were reconstructed with the RdObserverSimulation, once without and once with the addition of noise using traces from a selected period of ten minutes around each reconstructed event (c.f. Section 7.3). Figure 9.2a shows the correlation of the estimated radio energy for the proton and the iron simulations of the same event (if both could be successfully reconstructed). It is clearly visible, that the difference between the two different primaries is on a negligible level with only few outliers. Fitting a Gaussian function to the distribution of energy ratios yiels a sigma of 0.1 (c.f. Fig. 9.2b). Therefore, from this point on only one simulation will be used in the analysis to release an additional layer of complexity in the presentation of the collected results. The iron primary is chosen due to the higher number of successfully reconstructed events. It will be mentioned as simulated dataset. If noise was added during the RdSimulationObserver, this will be marked seperately.

For both, data and simulation, an additional reconstruction of the shower polarization is performed during the reconstruction. The underlying algorithms and quantities have already been explained in Section 4.3.2. Several cuts are applied to all datasets to provide a sufficient quality of the shower reconstruction as well as the parameters used for this analysis, especially the fit of the two-dimensional radio LDF. They will be disucssed in the following.

The SD reconstruction and especially the included fitting of the particle LDF is optimized for zenith angles below 55°. Although an additional horizontal directional reconstruction algorithm is used in the RdObserver, there is no horizontal LDF yet. The same actually holds for the RD reconstruction as well as also the radio LDF is not yet applicable to horizontal air showers [178]. Therefore, all events with a zenith angle above 55° are excluded from the analysis as in both cases the energy is directly determined from the LDF fits. As can be seen in Fig. 9.3 this reduces the total number of events by roughtly 23%.

Two additional cuts are targeted at the shower geometry. The first one is rejecting events, which have an angular deviation between the reconstructed SD and RD shower direction of $\Omega_{\mathrm{SD/RD}} > 3°$. This is just to ensure an appropriate reconstruction of the shower direction for both detectors, which is of course important for the reconstruction of the signal amplitude, especially for the radio part with the directional dependence of the antenna gain. The second cut requires both reconstructed shower cores to be confined inside the area of the externally triggered RDS of AERA124 (c.f. Fig. 6.1). This geometrical constraint is mainly important for the RD reconstruction again as especially for low RDS multiplicities the radio LDF can hardly be fitted if outside the antenna array.

A more or less natural mathematical cut is already applied during the reconstruction as only for events with five or more RDS a sophisticated fit of the RD core position can be performed during the LDF fit. Otherwise the core position is calculated by a barycenter reconstruction of the participating RDS. Thus, only events with five or more RDS are included in the analysis.

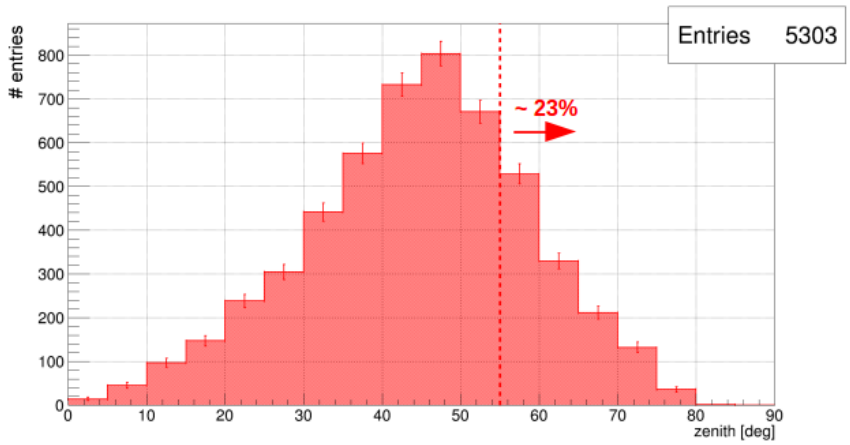

Figure 9.3: Zenith distribution as reconstructed with the SD and the RD for the measured dataset. The red line indicates the zenith cut at 55°.

As the shower energy determined by SD as well as the emitted radio energy from the RD are one set of parameters, which are correlated in Section 9.4 a good quality of these parameters is mandatory. Firstly, events which have no reconstruction of either SD or RD energy are excluded. By construction there is possibility that a negative energy is reconstructed from the radio LDF, which has no physical meaning and therefore is a reflection of a poor quality of fit, which leads to an exclusion of these events.

Additionally, a check on the quality of the fitted emitted radio energy is performed. Here, we apply a cut on the ratio of energy uncertainty to energy as estimator for the goodness of fit. This means that all events are rejected where $E_{\mathrm{RD,\,err.}}/E_{\mathrm{RD}} < 20\%$. Figure 9.4 shows the distributions of the ratio of the error on the RD energy and the RD energy with respect to the number of stations in the event for the measured and the simulated dataset. One can see that for the measured dataset the mean ratio is below the 20% margin events with eight or more RDS. Therefore, this cut is mostly efficient for lower station multiplicities. For the simulated dataset the ratio is well below 10% as $E_{\mathrm{RD,\,err.}}$ is underestimated due to the lack of noise. For the simulated dataset with noise the shape is similar to the one of the measured dataset, but slightly shifted upwards. After all, this kind of conservative cut value is used to guarantee a sufficient accuracy on the estimated radio energy.

Another constraint on the fit quality is performed by cutting on the σ parameter of the radio LDF fit, which is representing the width of the large Gaussian function (c.f. Section 4.4). Events with $\sigma_{\mathrm{LDF}} > 300$ m are rejected to avoid unphysically broad LDFs. Those are most likely to appear for events with only few stations, but can also appear at higher station multiplicities, if several stations close to the shower axis have a similar level of amplitudes. Additionally, also events are rejected, where σ_{LDF} converged at the parameter limits, which is also a sign for non successful and therefore non physical fit.

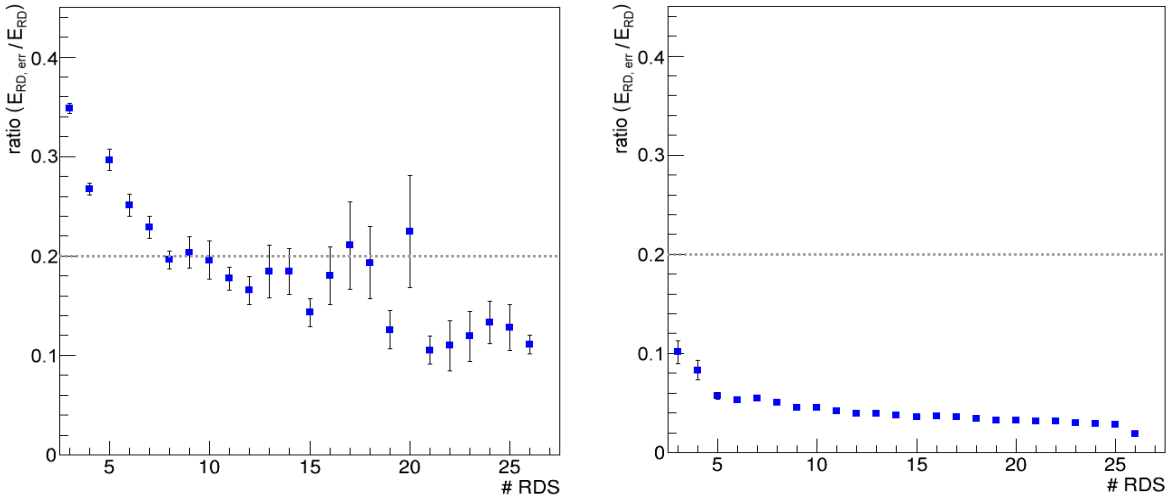

htb] **(a)** **(b)**

Figure 9.4: Ratio of RD Energy error to RD Energy versus number of RDS for the measured (a) and the simulated dataset (b).

	measured dataset	**simulation**	**simulation + noise**
total # events	5303	4688	3905
$\theta > 55°$	1236	866	735
$\Omega_{\mathrm{SD/RD}} > 3°$	562	107	355
Core not confined	1524	898	813
# RDS < 5	3170	40	1521
$E_{\mathrm{RD}} \leq 0$	481	16	69
$E_{\mathrm{RD,\,err.}}/E_{\mathrm{RD}} > 20\%$	3445	8	3038
$\sigma_{\mathrm{LDF}} > 300$ m	867	240	707
σ_{LDF} at ParLimit	304	16	54
no WS data	644	574	493
# events left	450	416	213

Table 9.1: Overview of the number of events per dataset, which are rejected due to the different cuts in the analysis.

Finally, all events are excluded, which do not have any database entry for the atmospheric electric field measurement in at least one of the weather stations for the specified time interval around the event time (see Section 9.3). Table 9.1 gives a summary on how many events have been rejected for what reason for all three datasets. The total number of reconstructed events of the measured and the simulated dataset differ by roughly 10%. This is mainly resulting from a rejection of events during the SD detector simulation part of

the RdSimulationObserver, when no SD trigger can be formed. The further discrepancy in numbers between the simulations with and without noise results from a lack of periodic triggered data, especially in the early stages of phase II, so no noise could be added during the reconstruction and the event is rejected. Cuts are not exclusive here, so a single event can be rejected for multiple reasons. Regarding the measured dataset, a large fraction of events is deselected by the number of RDS as well as by the cut on the error ratio. In a second instance, the geometrical cuts on the zenith angle and the core composition become efficient. For more than 10% no weather station data is available, which is mostly due to some larger downtimes in the period, where only one weather-station was deployed. The application of the prior mentioned cuts will be indicated either by the denotation full set (without cuts) or quality set (with cuts). When applied, the remaining sample is on the order of 10% of the original statistics for both, the measured and the simluated dataset.

9.3 Field Analysis

The measurement of the static electric field on ground level does not provide a sufficient estimator for the electric field in the emission region of the air shower as discussed in Section 4.5. However, it can be used to distinguish time periods with abnormal atmospheric conditions in the measurement region. For this purpose a time interval needs to be specified, which then indiciates the electric field situation. This time interval has to be chosen in such a way, that it contains the region of the atmosphere, which was traversed by the air shower. Therefore, the shower inclination and the cloud velocity have to be taken into account.

The two possible scenarios are shown in Fig. 9.5. In the first case the air shower with inclination θ traverses a charge region inside a cloud at height h_{cloud} moving towards the observer with velocity v_{cloud}. This will lead to a shift in the arrival time of the cloud above the observer of

$$\tau_{\text{shift}} = \tan(\theta)\frac{h_{\text{cloud}}}{v_{\text{cloud}}} \tag{9.1}$$

with respect to the event time. In the second scenario the cloud has already passed the observer and is moving away from it, when it is crossed by the air shower. As this simply corresponds to a shift of the reference frame the resulting shift τ_{shift} will be identical (disregarding the travel time of the air shower, which is negligible in this context). There is no distinct way to determine, which of the cases holds for each event and so every possibility has to be checked. Afterwards, the mean field strength ε is calculated by averaging over all available measurements of both weather stations. This might result in a mis-estimation of the true field strength, especially for cases, where not both periods show the same behaviour with respect to ε. However, as the primary interest is the definition of basic cut parameters for the influence of the external field on the radio emission, this might be the best possible valuation.

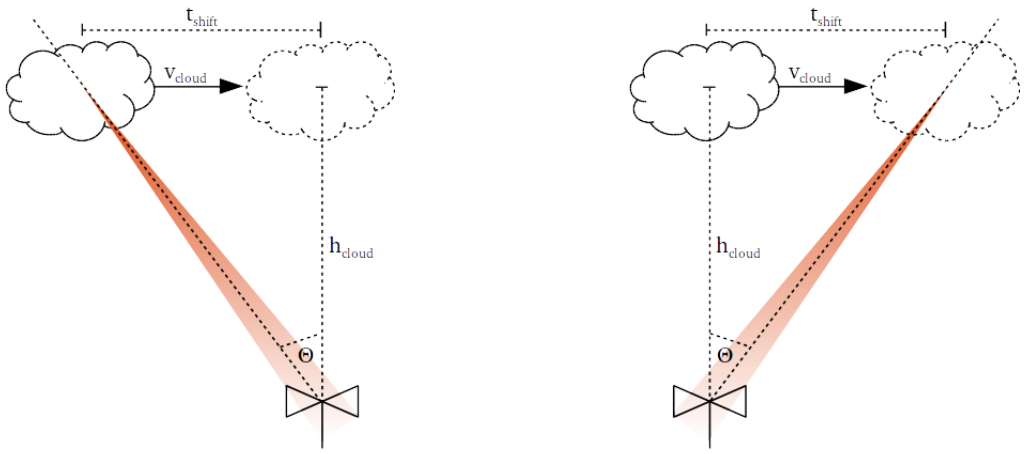

(a) **(b)**

Figure 9.5: Possible scenarios for the position and movement of the charged cloud region with respect to the air shower development. Cloud moving towards the observer (a) and away from it (b).

Figure 9.6 shows the electric field at ground level for one example event of the measured dataset with an inclination of $\theta \approx 40°$. Here, normal field conditions are found for the whole period around the event except for an interval of roughly 15 minutes appearing shortly after the detection of the air shower. The fields yields a fast increase to strengths of $\varepsilon \approx 300$ V/m, but is also decreasing in the same manner. Field variations of this type are not found that often and might either correspond to a far away thunderstorm region or even more likely to Nimbostratus clouds. Due to the algorithm mentioned above, this period is used for the field estimation, which actually has lead to an amplification of the radio emission (see latter).

The presented approach is based on the assumption, that a majority of the relevant cloud will directly pass on top of the observer, which will hold only for a smaller fraction of the sample. The remaining part will pass outside the observer. However, for strongly charged clouds there should still be a detectable increase in the field strength at ground level during the phase of the closest approximation. In this case, the determined field value will be weaker than the "true" one. In addition, there is yet no reliable way for the determination of h_{cloud} and v_{cloud} at the AERA site. Especially the strong fluctuations on the wind direction do not allow the use of the weather stations measurements for this purpose. Therefore, we define

$$v_{\text{cloud}} = 50 \text{ km/h}$$
$$h_{\text{cloud}} = 5 \text{ km},$$

which are well established average parameters for clouds in thunderstorm regions. The actual calculation of the electric field is then performed inside an interval $\Delta\tau$ around

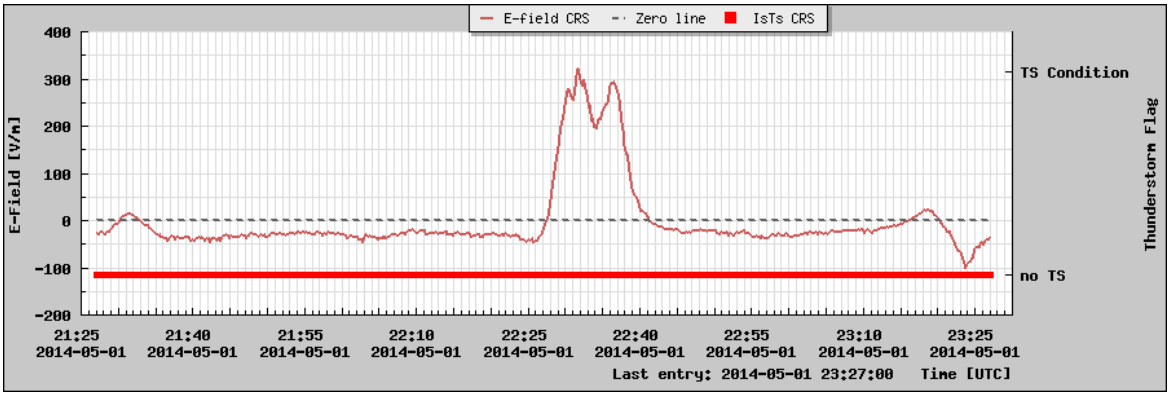

Figure 9.6: The atmospheric electric field on ground level for an example event with a short period of high field strength after the arrival of the air shower. The time of the event is at the center of the plotted interval.

$\pm\,\tau_{\text{shift}}$ using the averaging discussed beforehand. This interval is introduced to address the uncertainty of the cloud properties. On the other hand the extend of this interval has to be chosen such, that it is not affected to much by the quite rapid changes of field strengths during thunderstorms. Thus, the size of the averaging interval is set to

$$\Delta\tau = \pm\ 30\ \text{seconds},$$

which roughly corresponds to an opening angle of 10° at h_{cloud} above the array. An interval of this size should also be able to diminish the influence of the distance between the core position and the position of the weather stations.

Figure 9.7 shows the averaged field values as well as the corresponding standard deviation for the determined time interval for each event in the measured dataset. From the distribution of the mean values in Fig. 9.7a it is clearly visible, that most of the events have been measured during normal atmospheric conditions. However, there are events with field strengths up to several kV/m in both polarizations. A zoom on the same distribution, shown in Fig. 9.7b, reveals a mean electric field between $\varepsilon = -100$ V/m and $\varepsilon = +100$ V/m with an assymetric shift towards minor values of negative polarity. Thus, for presentation reasons, we will mostly use the absolute representation of the electric field value from this point on as shown in 9.7c, still providing information of the sign of the polarity in a seperate way.

The distribution of the associated standard deviations is depicted in Fig. 9.7d and shows the major population below $\sigma_\varepsilon = 20$ V/m, but also reaching values up to 5 kV/m. The mean value and the standard deviation for the same time period naturally yield a strong correlation as can be seen in the two-dimensional distribution for the full set in Fig. 9.8a.

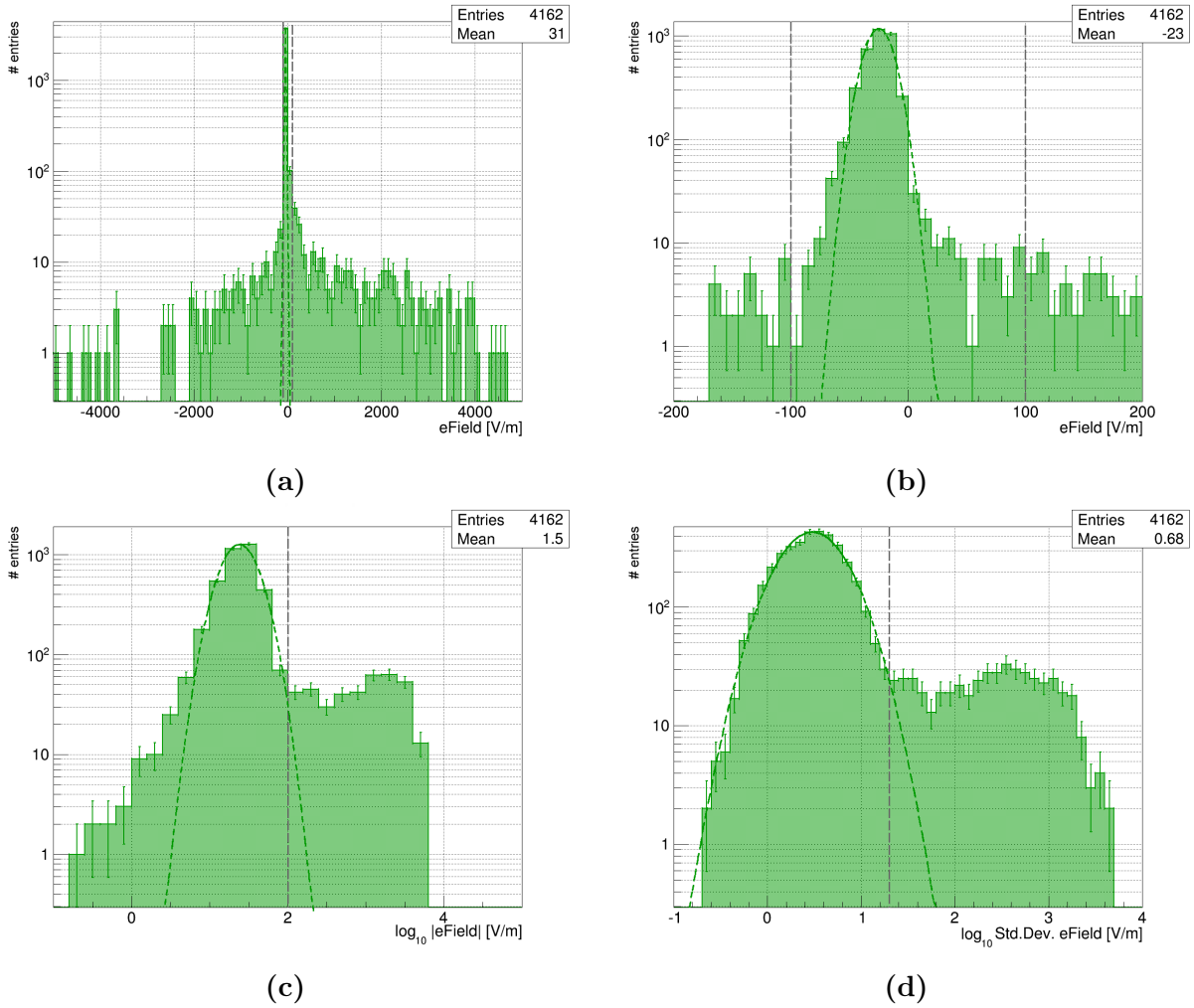

Figure 9.7: Measured atmospheric electric field for each event in the RdObserver v1r3 dataset, if weather station data are available. Mean value (a), zoom on the mean value (b), logarithm of absolute mean value (c) and logarithm of standard deviation (d) of the electric field averaged over a time interval of $\Delta\tau = 30$ seconds around the corrected event time and over both weather stations, if available. The dashed lines indicate the separation values for high electric fields.

However, there are few events, which only show a larger value in one of the two parameters. Therefore, we define cuts at

$$|\varepsilon_{\text{cut}}| \geq 100\,\text{V/m}$$
$$\sigma_{\varepsilon_{\text{cut}}} \geq 20\,\text{V/m}$$

as an indication for a strong atmospheric electric field. If one of these conditions is fulfilled, we will flag the event as recorded during thunderstorm conditions. This will be indicated

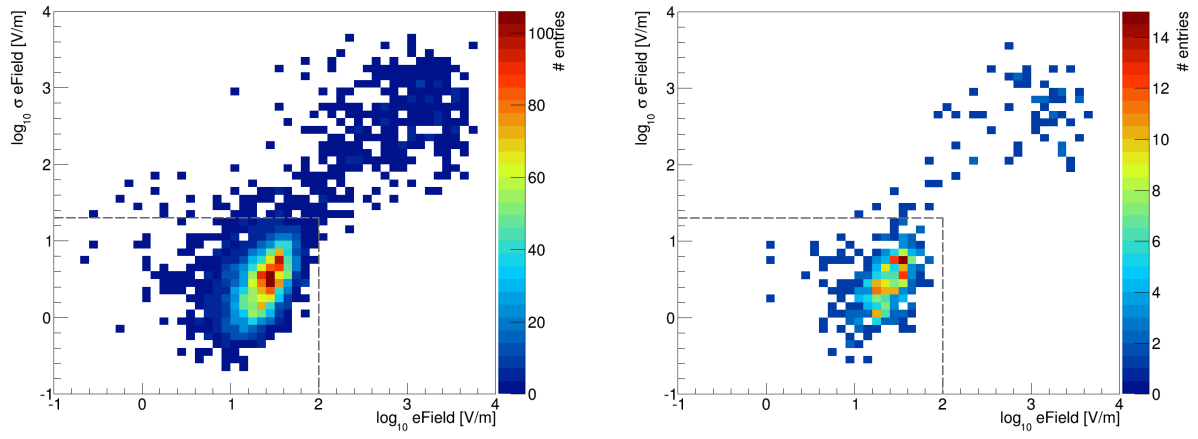

(a) **(b)**

Figure 9.8: Two-dimensional distribution of the logarithmic mean electric field and standard deviation for each event in the RdObserver v1r3 dataset, if field mill data are available. The full set (a) and the quality set (b) after the quality cuts are applied. The dashed lines indicate the separation values for high electric fields.

as *TS cond.* in the following analysis. Otherwise, in case of normal atmospheric conditions *no TS* will be used.

If plotted for the quality set, a weak separation can be found between the two regions as shown in Fig. 9.8b. This makes the further analysis a little bit more independent from the precise value of the determined cuts. A crude estimation using only the raw field measurements from the database yields a fraction of 3.3% of all entries with $\varepsilon > \varepsilon_{\text{cut}}$ for the CRS weather stations and 3.8% for the AERA weather station. So we can state, that the influence on the duty cycle due to periods of strong atmospheric electric fields is well below 4%.

9.4 Energy Analysis

While traversing a strong atmospheric electric field the amount of radiation, which is emitted in the radio regime can be heavily influenced. The most favourable configuration is such, that the shower particles experience a further acceleration and deflection, which will lead to a strong increase of the radio emission measured by the RDS of AERA. In contrast, there are of course also field configurations, which will cause a significant reduction of the radiated power or may not change it at all due to the superposition of different effects.

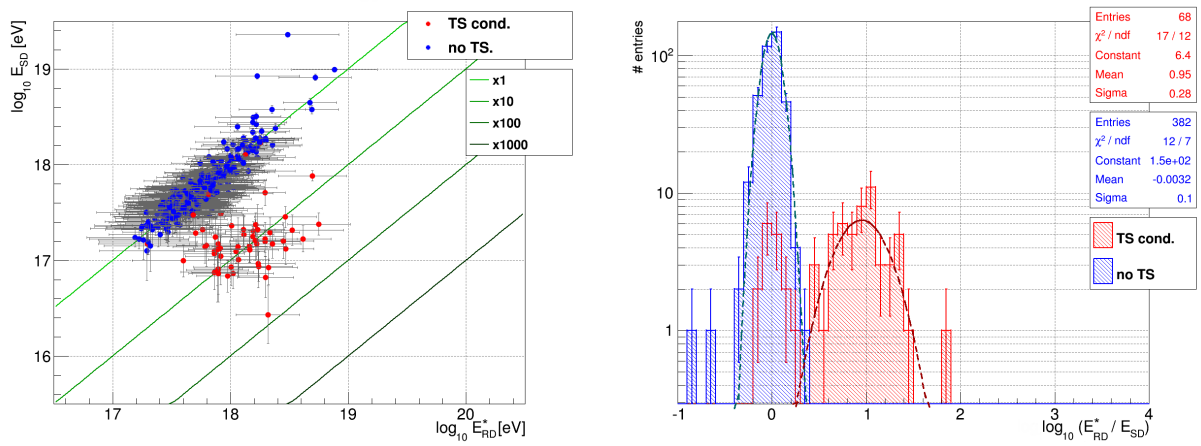

(a) **(b)**

Figure 9.9: Shower energies E^*_{RD} versus E_{SD} (a) and ratio $R(E^*_{\mathrm{RD}}/E_{\mathrm{SD}})$ (b) for the quality dataset. Events during TS cond. are marked in red, no TS in blue.

Concerning the different reconstructed energy values the following naming convention will be used: $E_{\mathrm{RD,\,data}}$ and $E_{\mathrm{RD,\,sim}}$ represent the radiated energy estimated from the two-dimensional fit of the radio LDF for the measured respectively the simulated dataset. Furthermore, E^*_{RD} yields the shower energy of the RD reconstruction calculated with the inverse of Eq. 4.32 using $S_{\mathrm{radio}} = E_{\mathrm{RD,\,data}}$ and E_{SD} denotes the shower energy reconstructed with the SD. Additionally, also the ratio of two energy values will be used, which is defined as

$$R = \log_{10} \frac{E_1}{E_2}, \tag{9.2}$$

thus $R = 2$ corresponds to an amplification of E_1 with respect to E_2 by a factor of 100.

In a first approach a comparison of the shower energies reconstructed by the two different techniques of the SD and the RD is performed. Figure 9.9a shows the distribution of E^*_{RD} versus E_{SD} for the quality dataset. The solid green lines indicate the function for a 1:1 (brightest) to 1:1000 (darkest) correlation. It can be seen, that the events recorded during normal atmospheric conditions are nicely correlated. The ratio plot in Fig. 9.9b yields a mean ratio $\bar{R}$ fully compatible with zero for a gaussian fit of this subset. Whereas, the thunderstorm events mostly show an energy $E^*_{\mathrm{RD}} > E_{\mathrm{SD}}$ with a fitted ratio of $\bar{R} = 0.95 \pm 0.28$, thus an amplification of one order of magnitude. A minor set of events classified as TS cond. can be found in the non-amplified region, which, beside low statistics, also follows a gaussian distribution. In this case a mis-identifaction of the atmospheric conditions is most likely, caused by some nearby strong field environment recorded by the field detector, but not traversed by the air shower. In addition, almost all of the thunderstorm events are located in the lower energy regime with $E_{\mathrm{SD}} < 10^{17.5}$ eV, some even going down to values below 10^{17} eV, which would under normal circumstances be well below the detection threshold of AERA. Thus, the amplification of the radio emission inside the thundercloud

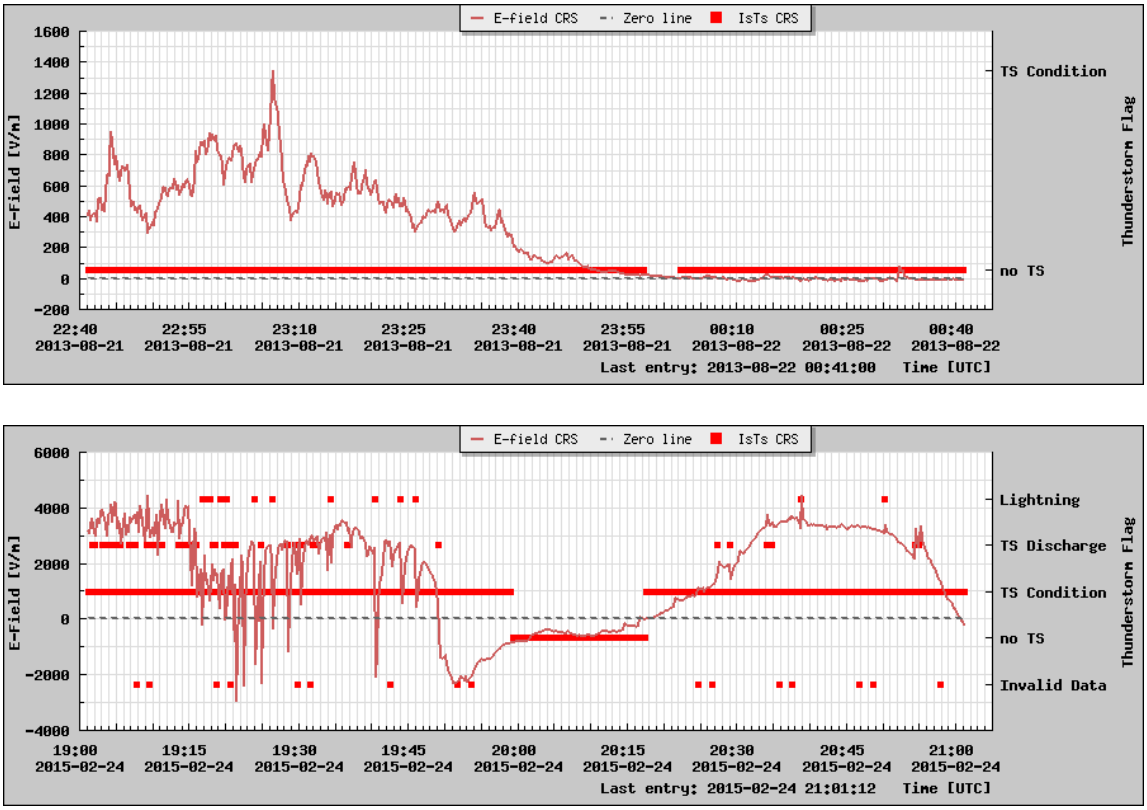

Figure 9.10: The atmospheric electric field on ground level for two outlier events with high field strength, but low emission amplification. The time of the event is at the center of the plotted interval.

leads to the detection of showers, which normally could not be measured. Also the opposite effect, i.e. an attenuation of the emitted radiation, should occur. However, these events will not be recorded as they fall below the radio threshold, although they should be detectable without the modification.

Therefore, this analysis has basically proven that the chosen values for ε_{cut} and $\sigma_{\varepsilon_{\text{cut}}}$ yield reasonable results and are therefore in first approximation a good estimator for the usabililty of data for high quality analysis.

Nevertheless, beside the general agreement, there are some outlier events, which do not follow the expectations respectively result from unfortunate charge region to shower geometries. Figure 9.10 shows the electric field measurements for two time intervals of ± 1 hour around two example events with a high field strength, but a low emission amplification. The first one is most likely timed at the end of a thunderstorm period. Here, the high field strength is decaying back to normal conditions in the minutes before the event time. This probably is related to the cloud front moving away from the array and therefore, the air shower, which might be coming from the opposite direction, does not traverse the charged layers

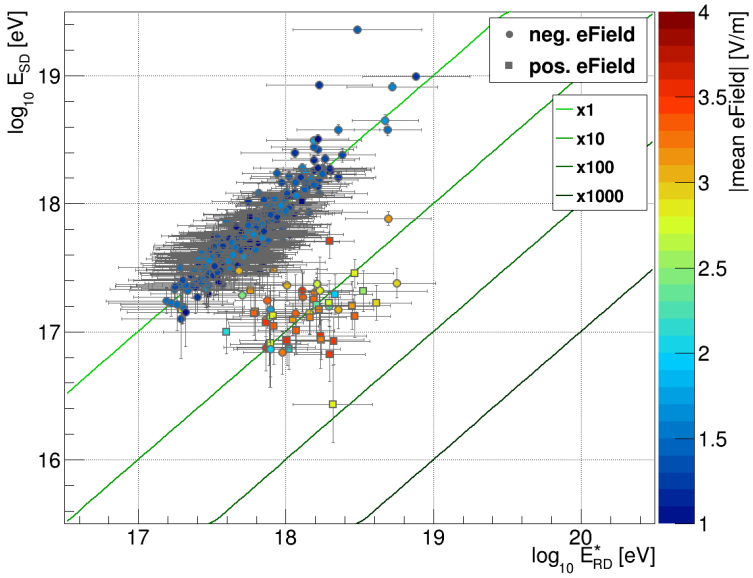

Figure 9.11: Shower energies E^*_{RD} versus E_{SD} for the quality dataset. Color-coding indicates the field strength measured by the weather stations, the marker style shows the field polarity (circle = negative, square = positive).

anymore. This assumption is supported by the measurement of the wind direction, which is pointing roughly southwards with $\phi_{\mathrm{wind}} \approx 270°$ in the period around the event, while the air shower arrives from a direction $\phi_{\mathrm{EAS}} = 141°$.

The second event depicted in Fig. 9.10 was also recorded with low amplification ratio, but shows some very high field strength before as well as after the event time even including several rapid changes of polarity, which is a clear indicator for lightning strikes. However, right at the time of the event the measured field strength becomes more moderate for a period of about 15 minutes, but not quite reaching normal conditions. This might result from two different thundercloud regions crossing the array close to each other, but with a large enough spatial separation to cause a drop of the electric field on ground level. Therefore, a shower traversing the atmosphere in between these two regions might surely experience some influence of a varied atmospheric fields, but its strength might not be high enough to modify the amount of radio emission.

Beside the general modification at high field strenghts, there might be additional effects due to the precise value as well as the polarity of the electric field. Figure 9.11 again shows the distribution of E^*_{RD} versus E_{SD} for the quality dataset, this time with the strength and the polarity of the atmospheric electric field in the time interval $\Delta\tau$ around the individual event time encoded in the marker color respectively marker style.

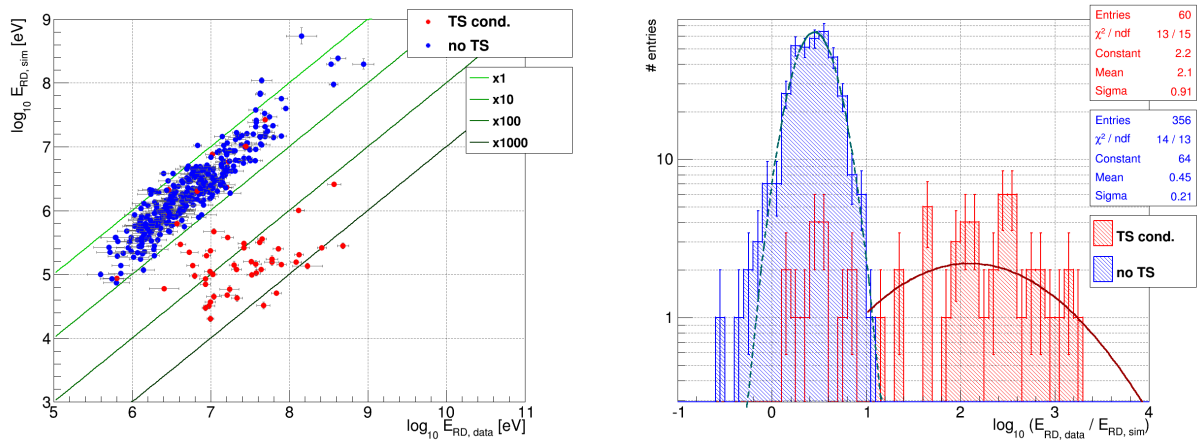

(a) **(b)**

Figure 9.12: Radiated energies $E_{\mathrm{RD,\,data}}$ versus $E_{\mathrm{RD,\,sim}}$ (a) and ratio $R(E_{\mathrm{RD,\,data}}/E_{\mathrm{RD,\,sim}})$ (b) for the quality dataset. Events during TS cond. are marked in red, no TS in blue.

At first glance, no general gradients with respect to field strength or polarity are visible. However, there are some substructures, which are worth to be discussed. In the low energy region $E_{\mathrm{SD}} < 10^{17}$ eV there is a clear excess of fields with a positive polarity, which also show a minor correlation of higher field strength resulting in a stronger amplification. The same holds for events in the region above an amplification factor of 10, where 19 out of 26 events have a positive polarity. Additionally, it seems that there is a slight gradient for these events in the negative E_{SD} direction, thus lower energetic events need a higher field strength to achieve the same amplification. Both observations agree with the expectations from the modeling of regions in thunderclouds, where the lower charge region is mainly of positive polarity and so an air shower, which traverses these cloud rather central, will experience the full effect of the present electric field.

Furthermore, there is a grouping of events with negative polarity around an amplification factor of 10 at energies of $E_{\mathrm{SD}} \approx 10^{17.2}$ eV. In this case the atmospheric field might result from a source not direct above the array, but further away and therefore, the measured field is not the one from the lower charge region, but rather the next following (mostly negative) charge layer, which is then "seen" from the side. This might also hold for the air shower due to geometrical reasons, which might not cross the central region of the thundercloud, but more likely passes by in the outer part and thus, will only experience a minor part of the emission amplification.

The same method can be used again, this time for a comparison of the RD itself, i.e. compare the measured dataset with the results from the simulations. Figure 9.12a shows the distribution of the measured radiated energy $E_{\mathrm{RD,\,data}}$ versus the simulated one $E_{\mathrm{RD,\,sim}}$ in the quality dataset. In general, the same behaviour is found as for the comparison of

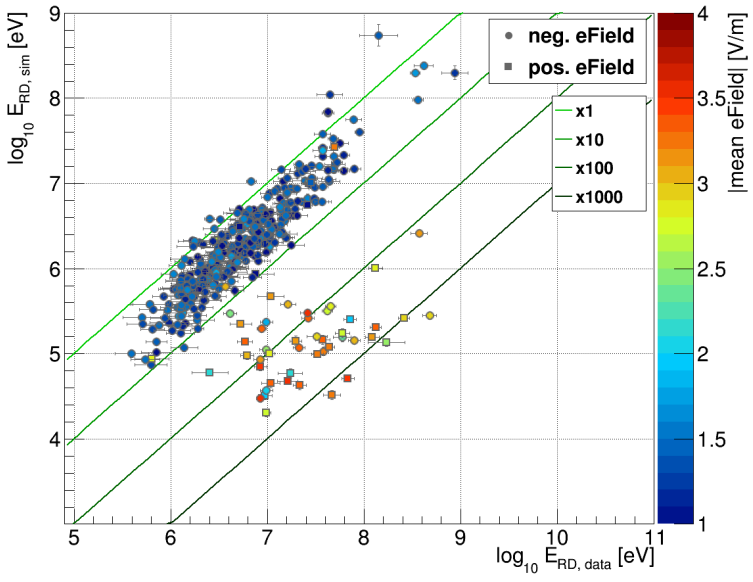

Figure 9.13: Radiated energies $E_{\mathrm{RD,\,data}}$ versus $E_{\mathrm{RD,\,sim}}$ for the quality dataset. Color-coding indicates the field strength measured by the weather stations, the marker style shows the field polarity (circle = negative, square = positive).

the shower eneriges, which is expected due to the direct proportionality by Eq. 4.32. The offset from a one-to-one correlation is caused by the absence of noise for this simulation dataset. As already mentioned before an additional RdSimulationObserver reconstruction including noise was also performed, however it turned out that none of the thunderstorm events could be successfully reconstructed. Although this is rather unfortunate for the sake of this analysis, it also shows that the presence of strong atmospheric electric fields leads to the detection of events, which normally would be below the detection threshold. For completeness it shall be mentioned, that the events of this sample measured under normal conditions yield a ratio, fully compatible with the expectation of 1. The thunderstorm events for the sample without noise are mostly located around an amplification of 10^2, which is in agreement with the squared amplification factor of the shower energy. However, also increased emission by a factor of 1000 is measured. The ratio distribution in Fig. 9.12b yields a fitted ratio of $\bar{R} = 2.1$ for the TS condition set, but including a much larger spread. Also here some thunderstorm events can be found in the low amplification region due to a mis-identifaction of the atmospheric electric field as discussed earlier.

The same distribution of radiated energy is shown once more in Fig. 9.13, again adding the information of the precise atmospheric electric field value and polarity. Similar to the shower energy, there is no visible structuring for the thunderstorm events. Also here, the events with the lowest amount of radiated energy were measured during periods of electric fields with positive polarity.

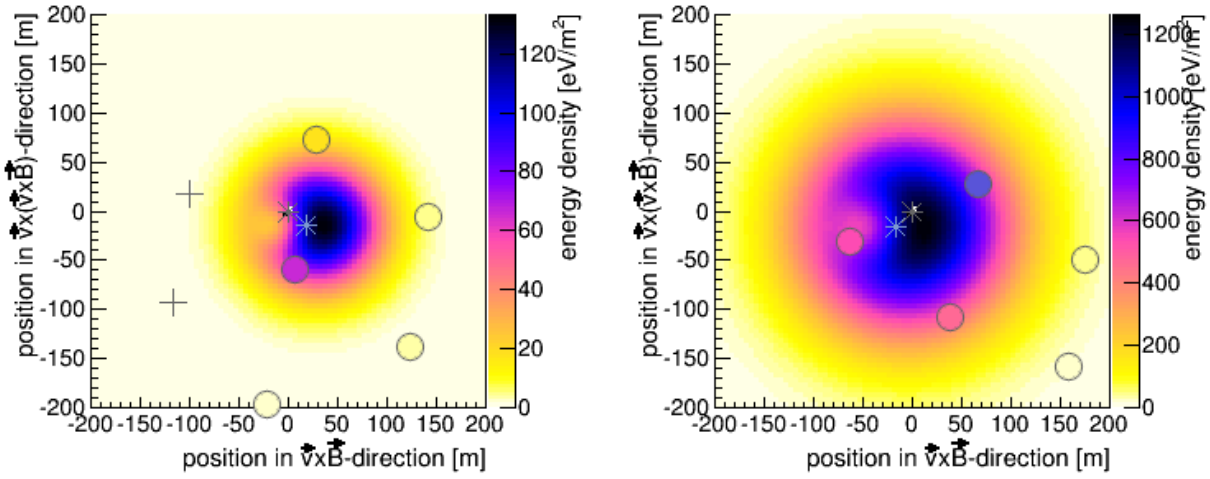

Figure 9.14: Two-dimensional radio LDFs for a pair of twin events with $\varepsilon_{1.1} \approx -22$ V/m (a) and $\varepsilon_{1.2} \approx -1595$ V/m (b). Note the different scale of the color axis.

ID	$\theta_{\mathrm{SD}}[^\circ]$	$\phi_{\mathrm{SD}}[^\circ]$	E_{SD}[eV]	ε[V/m]
Twin #1.1	27.1	237.9	$10^{17.27}$	-22
Twin #1.2	24.2	233.4	$10^{17.33}$	-1595
Twin #2.1	44.4	16.9	$10^{17.6}$	-16
Twin #2.2	42.0	13.0	$10^{17.6}$	610

Table 9.2: Shower parameters for the two pairs of example twin events.

An additional test on the influence of the atmospheric electric field can be performed by the investigation of event pairs in the measured dataset, which share approximately the same shower parameters, i.e. direction and energy. These events will be called "twin events" in the following. For this analysis an angular deviation of

$$\Omega_{\mathrm{twin}} < 5^\circ \tag{9.3}$$

and an energy difference of

$$|\log_{10}(E_{\mathrm{twin},1}) - \log_{10}(E_{\mathrm{twin},2})| < 0.1 \tag{9.4}$$

were chosen as twin criteria. One of the twins is measured during normal atmospheric conditions, while the other one is recorded during thunderstorm conditions. This allows a direct comparison of observables like the size of the radio LDF or the radiated energy.

Figures 9.14 and 9.15 show the two-dimensional LDFs for two pairs of twin events. The shower parameters are given in Table 9.2. The radiated energy for the first twin event

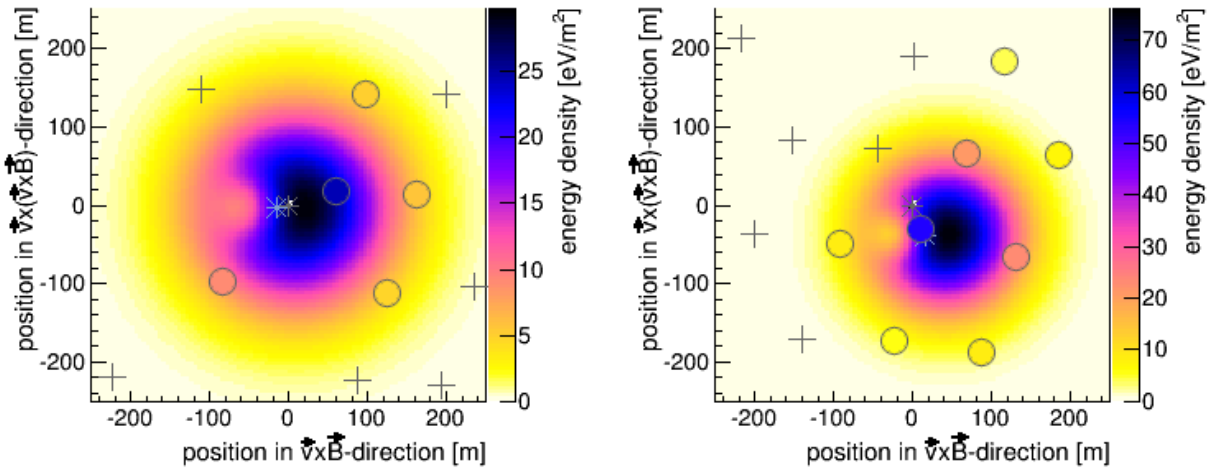

Figure 9.15: Two-dimensional radio LDFs for a pair of twin events with $\varepsilon_{2.1} \approx -16$ V/m (a) and $\varepsilon_{2.2} \approx 610$ V/m (b). Note the different scale of the color axis.

measured during normal conditions is $E_{\mathrm{RD,\ data,\ 1.1}} = 1.56 \times 10^6$ eV. The corresponding thunderstorm event yields a strong electric field with negative polarity, which results in a strong amplification of the radiated energy to $E_{\mathrm{RD,\ data,\ 1.2}} = 4.18 \times 10^7$ eV, thus roughly a factor 30 higher. This is also clearly visible in the dimension of the radio LDF, i.e. the size of the footprint. Please note that due to the different scales of the z-axis, the colors can not be compared one-to-one. Here, the black region (energy density $\sim 120\,\mathrm{eV/m^2}$) in the normal event corresponds more or less to the yellow one in the thunderstorm region. Therefore, the amplified emission results in an increase in the diameter of the footprint by a factor of ~ 7.

The thunderstorm event of the second twin was recorded during an electric field with positive polarity. Here, the event recorded under normal conditions yields a radiated energy of $E_{\mathrm{RD,\ data,\ 2.1}} = 2.01 \times 10^6$ eV, the thunderstorm event was measured with $E_{\mathrm{RD,\ data,\ 2.2}} = 2.75 \times 10^6$ eV. The amplification is not as big as in the previous case, but still exceeds the energy error bands with a factor of 1.4. This is also well outside the margin of fluctuations due to shower-to-shower variations. For the comparison of the LDFs we again take the central, black region of the normal twin, which has a diameter of roughly 100 m at an energy density $\sim 25\,\mathrm{eV/m^2}$. This corresponds to the light orange region for the thunderstorm twin with a diameter of 250 m. Thus, the footprint of the amplified event is enhanced by a factor of 2.5.

Unfortunately, the amount of available twin events with the required criteria is quite small, $\mathcal{O}(10)$. Therefore, a systematical study of the amplification with respect to radiated energy and footprint is not yet possible. Furthermore, a weakening of the twin criteria is

not recommended. Otherwise, the impact of the antenna pattern on the signal amplitude due to different shower geometries as well as the rather large errors on the shower energy of the SD reconstruction without calorimetric support of the FD might have a significant influence on the conclusion of the analysis. However, the general approach of this analysis can not only be used for this electric field study, but moreover for a well-founded estimation of detector accuracies like e.g. the energy resolution.

Another interesting parameter, especially in the context of the emission amplification inside thunderclouds, is the height of the shower maximum $h_{\max}$ as the main contribution to the emitted power results from this stage of the shower development. Therefore, the highest amplification is obviously reached, if the maximum is reached right inside the region of strong atmospheric fields. For the measured dataset an estimation of the depth of the shower maximum $X_{\max}$ is only available, if the event has also been measured by the FD, which is the case only for a handful of events for the quality dataset. For this reason, we use the information provided by the individual shower simulations, where the determination is performed automatically. To obtain the real height above ground, we use the geometrical distance to the shower maximum $R_{\max}$ and correct for the inclination of the shower, $h_{\max} = R_{\max} \cdot \cos\theta$.

Figure 9.16 shows the distribution of $h_{\max}$ as a function of the ratio of amplification $R(E_{\mathrm{RD,\,data}}/E_{\mathrm{RD,\,sim}})$. The strength and polarity of the atmospheric electric field are encoded in the marker color and style. First of all one can see, that the thunderstorm events mainly yield a $h_{\max}$ between 3.5 km and 6 km. This is in nice agreement with the position of the lower charge layer of thunderclouds, which has its maximum field strength between a height of 4 km to 5 km. There is a slight trend, that higher amplification ratios are reached for air showers, which develop their maximum at lower altitudes. These showers will already have produced a large number of electro-magnetic secondaries, when entering the strong field region. Therefore, they can produce a lot of additional emission even before the shower maximum is reached. However, no significant correlation between $h_{\max}$ and R can be found, but is also not expected due to the diverse configuration possibilites of thunderclouds. Generally speaking, the coincidence of shower maximum and maximum atmospheric field strength will for sure result in the largest amplification.

Please note, that the $h_{\max}$ used here corresponds to an air shower, which is not altered by atmospheric electric fields. The real height of the shower maximum will of course be at slightly lower altitudes due to the effects described in Section 4.5 (see also Section 9.6). Theoretically, the effect of the moving shower maximum should also be visible in measurements of the FD, either as simple shift in the amount of emitted light or even as divergence of the shower profile from the Gaisser-Hillas expectation, e.g. a plateau-like or linear behaviour close to the maximum. However, it is not very likely for such an event to be measured as it would first of all require the coincidence of a period with strong atmospheric electric fields and the 10% duty-cycle of the FD. In addition, the telescope measurements are most

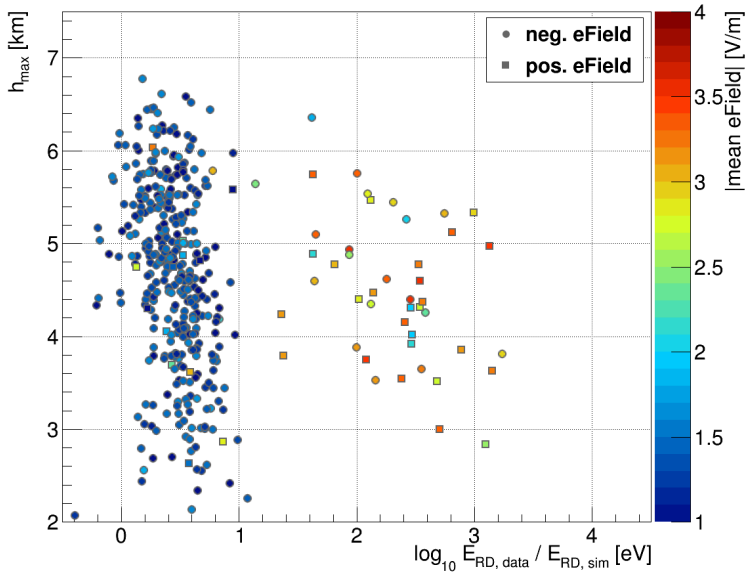

Figure 9.16: Ratio $R(E_{\mathrm{RD,\ data}}/E_{\mathrm{RD,\ sim}})$ versus the height of the shower maxmimum h_{max} determined from the shower simulation. Color-coding indicates the field strength measured by the weather stations, the marker style shows the field polarity.

efficient and accurate under cloudless conditions, which on the other side are needed for high field strengths. Therefore, such an analysis would be very ambitious.

9.5 Polarization Analysis

Due to the additional force acting on the shower particles, also the resulting polarization pattern of the emission can vary from the normal expectation. The underlying parameters and relations for the determination of the shower polarization have already been discussed in detail in Section 4.3. Using Eq.s 4.5 and 4.6 one can achieve an alternative representation of the polarization angle ψ, which then is defined as

$$\psi = \tan^{-1}\left(\frac{\sin\phi'}{\frac{\sin\alpha}{a} + \cos\phi'}\right) \tag{9.5}$$

for each observer of an air shower with the observer angle ϕ' defined as the angle between the vector pointing from the shower core towards the observer position and the $\vec{v}\times\vec{B}$-axis, α as the angle between the shower axis and the direction of the magnetic field vector and the charge-excess fraction a. This angle is equal to ψ_p, which was defined as angle of the semi-major axis of the polarization ellipse in Eq. 4.27. This one can be directly calculated from the Stokes parameters, i.e. deduced from the detector data itself. So given a sufficient

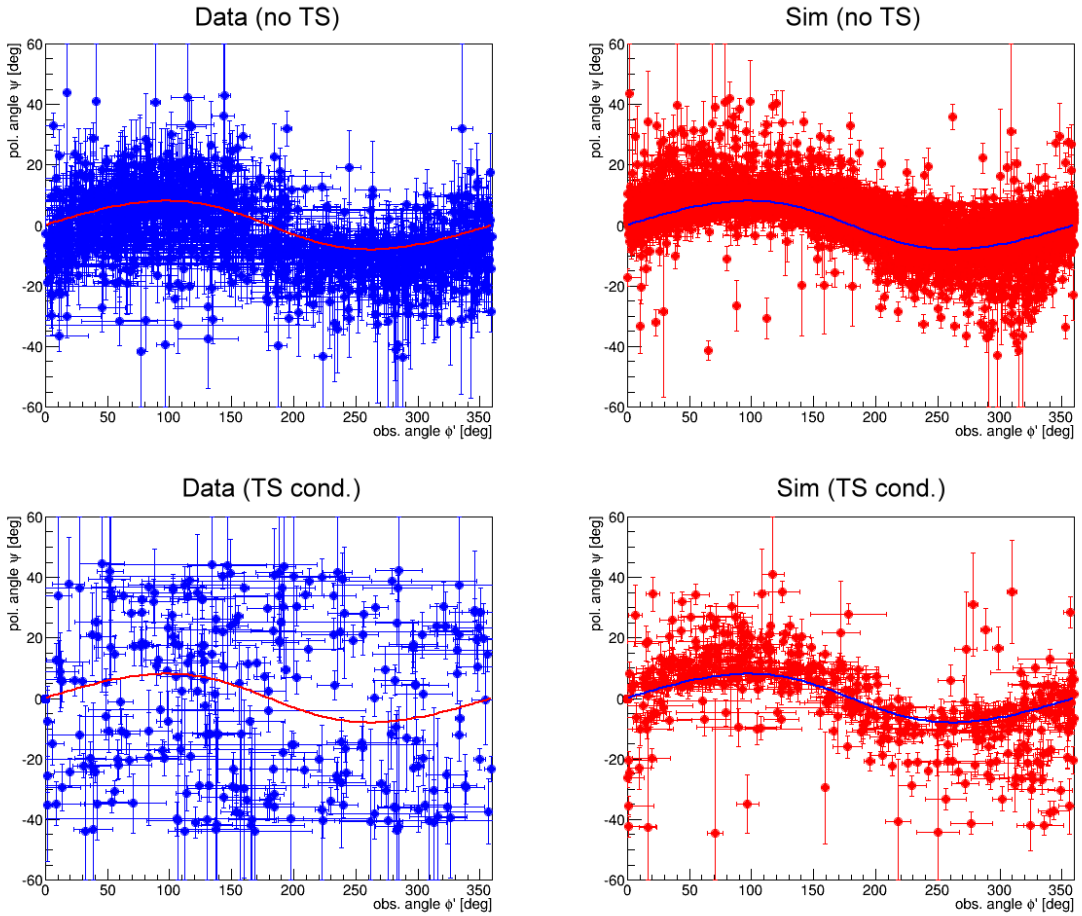

Figure 9.17: Polarization angle ψ as function of observer angle ϕ' for different subsets of events in the quality dataset. Measured dataset (blue) and simulated dataset (red) subdivided into no TS (top panels) and TS cond. events (bottom panels). The solid lines represent Eq. 9.5 with $\alpha = \pi/2$ and $a = 0.14$ and are drawn as guidance.

number of observers, Eq. 9.5 can be used to fit the charge-excess fraction a, allowing a direct conclusion on the contribution of the individual emission mechanisms.

As a first approach the polarization angles ψ of all RDS in the quality dataset of the measured and simulated data are presented in Fig. 9.17, subdivided into no TS and TS cond. events. As guidance the solid line represents Eq. 9.5 using a mean angle $\alpha = \pi/2$ and the experimentally confirmed charge-excess strength at the AERA site of $a = 0.14$. Both no TS samples clearly follow the expectations as well as the simulated TS cond. subset. However, the sample of events measured during thunderstorm conditions shows a complete random distribution, which is a first explicit indication for an alternation of the polarization pattern by a strong atmospheric electric field.

The uncertainty on the polarization angle σ_ψ is a combination of two individual contributions. The first component $\sigma_{\psi,\text{noise}}$ results from the influence of the radio background on the reconstruction of the Stokes parameters. It is already calculated during the RdSimulationObserver reconstruction by a noise addition method (c.f. Section 4.3.2). Additionally, there is a further component $\sigma_{\psi,\text{dir}}$ introduced by the uncertainty on the directional reconstruction of the incoming shower. This translates directly into an uncertainty in the angle α between the shower axis and the magnetic field, which then is used in the determination of the polarization angle. As up to now there is no calculation for the direction uncertainty, $\sigma_{\psi,\text{dir}}$ is fixed to 3°. To take into account a possible correlation of the two components, they are simply added linearly.

The uncertainty on the observer angle $\sigma_{\phi'}$ is mainly due to the uncertainty on the position of the shower core with respect to the position of the observing antenna $\sigma_{\phi',\text{core}}$. Here, the uncertainties estimated by the SD core reconstruction are used. Afterwards, the most conservative scenario is applied, i.e. the angular deviation δ between the vector from the position of the observer to the original core position (x_c, y_c) and the vector from the observer to the maximum shifted core position $(x_\text{c} \pm \sigma_x, y_\text{c} \pm \sigma_y)$ is calculated and $\sigma_{\phi',\text{core}} = \max(\delta)$ is used. However, for observers very close to the shower core this estimation can produce large uncertainties, when the area of the tested core positions overlaps with the observer position. In this case, the core position can "move" to the opposite site of the observer, which then will result in very large angles δ up to 180°. Furthermore, also here we linearly add an uncertainty of $\sigma_{\phi',\text{dir}} = 3°$ for the determination of the $\vec{v} \times \vec{B}$-axis.

Generally, the emission of the air shower is expected to be fully polarized, which would correspond to a degree of polarization of $p \approx 1$. Figure 9.18a shows p as a function of the atmopheric electric field for the quality set. In normal atmospheric conditions most of the RDS show a degree of polarization close to unity. However, there are also RDS with very low values of p. There are two possible effects, which can account for this. On the one hand, there might be a significant influence on the determination of the Stokes parameters by the radio background, which will be mostly unpolarized. This interference is of course most efficient for RDS with a low SNR as can be seen in Fig. 9.18b. For higher SNR there is a clear trend towards values of $p > 0.9$, but also here some very low degrees of polarization can be found. Those might be caused by the remaining presence of single noise RDS in specific events.

The situation changes for the RDS of events recorded during TS conditions. Here, the distribution of p is spread over the whole parameter range, some measurements even reach the state of an almost unpolarized signal. Thus, the corresponding emission must have been produced under significantly altered field conditions, which for sure are present in the charge regions of thunderclouds.

For the analysis of the polarization patterns of individual events, the required number of RDS is increased to # RDS ≥ 8. This is done, to achieve a better accuracy for the

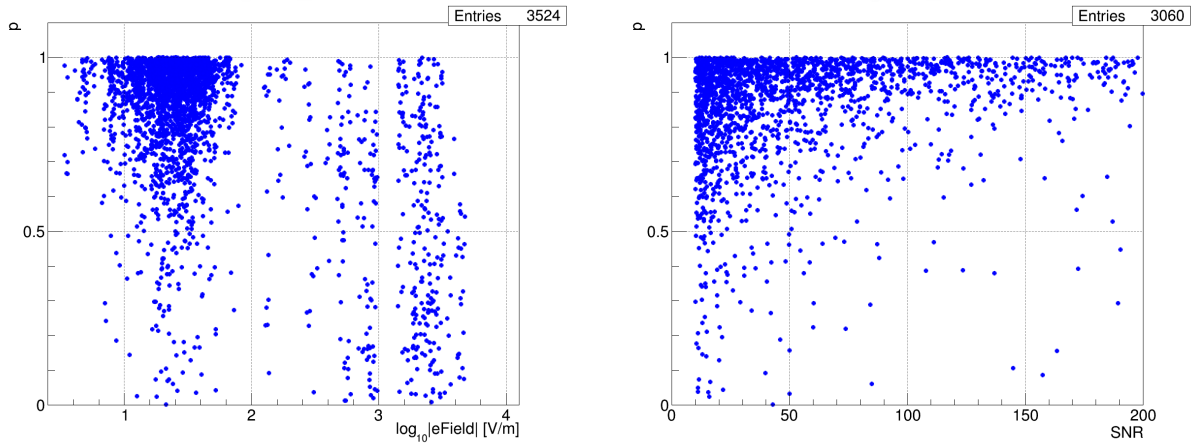

(a) **(b)**

Figure 9.18: Degree of polarization p per RDS as a function of the atmospheric electric field (a) and as a function of the SNR for no TS events (b) for the quality dataset.

fit of Eq. 9.5. The fit is performed with two free parameters, the angle between shower axis and the geomagnetic field α and the charge-excess fraction a. The parameter α is initialized with the value resulting from the reconstruction, but can be varied within a window of $\pm 3°$ due to the uncertainty on the shower direction. The parameter a uses the theoretical expectation of 0.14 as start value and is fitted within the range from 0 to 1. In addition, RDS with a degree of polarization $p < 0.8$ are excluded from the fit.

Figure 9.19a shows the polarization pattern for an event recorded under normal atmospheric field conditions from the measured quality dataset. The event has been recorded by a total of 13 RDS with an incoming direction of $\theta = 46°$, $\phi = 324°$, thus an angle to the geomagnetic field of $\alpha = 85°$ and a shower energy of $E = 8.8 \times 10^{17}$ eV. The distribution of the polarization angles is in nice agreement with the fit, yielding a $\chi^2 \,/\, ndf = 5.5 \,/\, 11$, which results in charge-excess fraction of $a_{\text{data}} \approx 15.5\%$. The simulation of the same event is shown in Fig. 9.19b, which includes 26 RDS. Also here the reduced χ^2 is close to unity and the corresponding fitted charge-excess fraction of $a_{\text{sim}} \approx 14.5\%$ agrees with the measured data as well as with the theoretical expactations.

The correlation between the fitted value of a for the measured and the simulated dataset is shown in Fig. 9.20. Here, events have been excluded, where the fit for one or both sets has converged to the parameter limits respectively not converged at all. The good agreement between data and simulation holds despite the partially huge uncertainties for a large fraction of the remaining sample measured under normal atsmopheric conditions. In general, the fitted fraction seems to be higher by roughly $3 - 5\%$ for the measured dataset. However, there are also some events that show a significant difference. Due to the increased requirement with respect to the data quality, the sample of events recorded

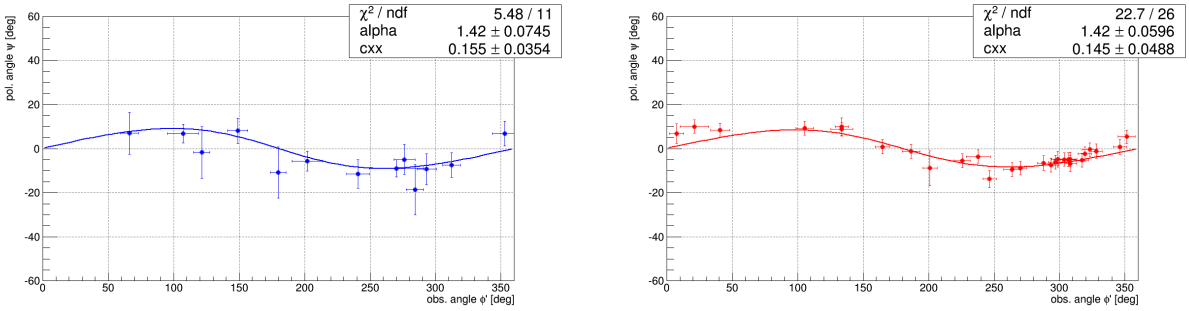

(a) **(b)**

Figure 9.19: Polarization pattern of an air shower recorded under normal atmospheric field conditions from the measured (a) and simulated quality dataset (b).

during thunderstorm conditions has reduced to a single event. This one though yields a compatible fraction of $a \approx 0.2$ for both, measured and simulated dataset. Figure 9.21 depicts the reduced χ^2 as measure of the fit quality. As can be seen most events have been fitted with $0 \leq \chi^2 \leq 2$ for the measured and the simulated dataset in equal measure, which further supports the general agreement with the theoretical expectation.

Figure 9.22 shows the fitted charge-excess fraction a as a function of the atmospheric electric field. As discussed in Section 4.3.1 a value of $a = 14 \pm 2\%$ was found for measurements at the Pierre Auger Observatory under normal atmospheric conditions. However, it is known (e.g. from measurements by LOFAR [179]), that a is not a constant value, but includes several dependencies i.a. on the shower inclination or the distance of the observer to the shower axis. In this analysis, only the events recorded during TS conditions will be investigated. For the moment, the primary aim is to check for deviations from the general charge-excess expectation without a precise determination of the actual value.

For the simulated dataset a rather constant charge-excess fraction is found for the whole range. A linear fit yields $\bar{a}_{\text{sim}} = 19.7\%$. This behaviour is expected as no atmospheric electric field is applied during the simulation. The measured dataset is distributed not as uniformly. A major part of the sample has been fitted with $0 \leq a \leq 0.3$, including some events with a very low charge-excess fraction. Additionally, three events are found, which yield a fraction around 50%. Overall a mean fraction of $\bar{a}_{\text{data}} = 25.3\%$ is fitted.

However, no statistically significant trend can be determined for the charge-excess fraction with an increasing strength of the atmospheric electric field. It should be mentioned though, that due to the cut on the angle to the electric field vector of $\beta < 55°$, which is calculated for a charge-excess fraction of 14%, during the RdObserver reconstruction, some RDS of specific events or even whole events with the most extreme deviations from the expected behaviour might even not be available in the currently used dataset.

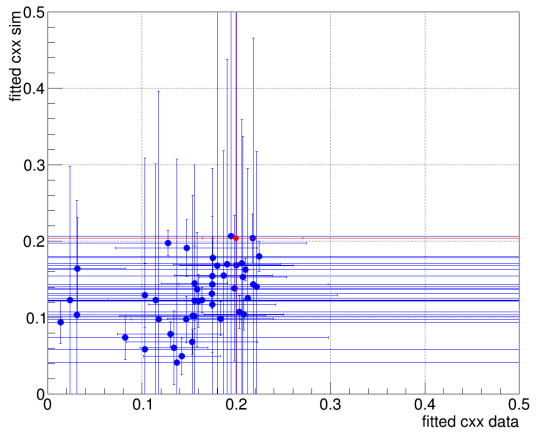

Figure 9.20: Correlation of the fitted charge-excess fraction a between the measured and simulated dataset. No TS (blue) and TS cond. (red).

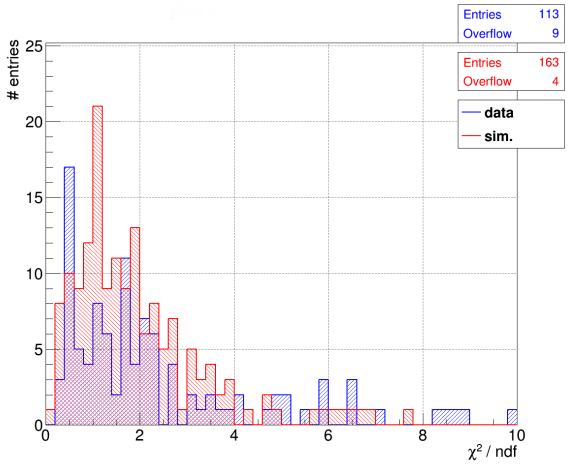

Figure 9.21: Distribution of the reduced χ^2 from the fitting of the charge-excess fraction a for the individual events of the quality set. No TS (blue) and TS cond. (red).

9.6 Simulations with electric fields

Beside the basic agreement of the measured dataset with the charge-excess expectation, some events have been found, which show a completly different behaviour. Figure 9.23 depicts the polarization pattern for an event in the measured and the simulated dataset recorded during an atmospheric electric field of $\varepsilon \approx 700$ V/m with shower direction $\theta = 35°$, $\phi = 289°$ and energy $E = 1.3 \times 10^{17}$ eV. While the simulation is in excellent agreement with the expectation, the distribution of polarization angles is shifted upwards, which corresponds to a global rotation of ψ with respect to the expected angle for normal atmospheric conditions. The measurement of events with the same behaviour has recently been reported by the LOFAR collaboration [175]. This rotation can be used in the fit, which modifies Eq. 9.5 to

$$\psi_{\mathrm{mod}} = \tan^{-1}\left(\frac{\sin(\phi' + \omega)}{\frac{\sin\alpha}{a} + \cos\phi'}\right) + \delta \tag{9.6}$$

with δ as the global shift of the polarization pattern. Furthermore, a phase ω was added to the determined observer angle with limits at $[-\pi, \pi]$. Fitting this modified version to the event from the measured dataset yields a rotation of $\delta \approx 19°$ with a phase of $\omega = 106°$.

To evaluate the influence of an external field on this event, it has be re-simulated, this time adding an atmospheric electric field during the simulation process and allowing a one-to-one comparison of data and the different simulations. A detailed, analytical description of the full field configuration is almost impossible due to the chaotic and turbulent charge distributions inside thunderclouds. Therefore, as a first and simple approach, a two-layered

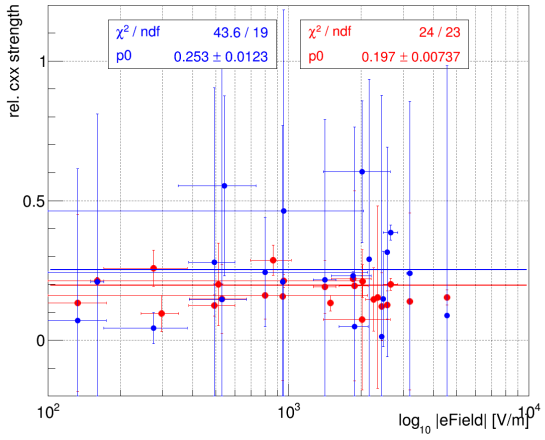

Figure 9.22: The fitted charge excess strength versus the measured atmospheric electric field for the quality dataset. Measured (blue) and simulated (red) dataset.

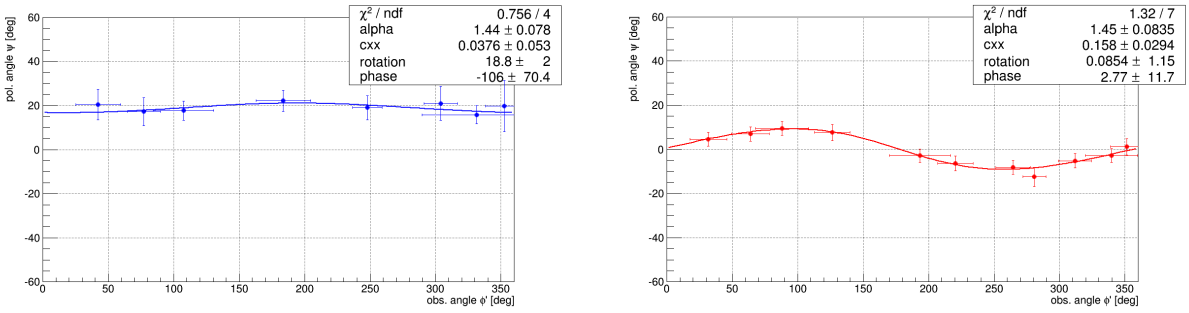

(a) **(b)**

Figure 9.23: Polarization pattern of an air shower recorded under TS cond. from the measured dataset (a) and from the simulated dataset (b) with a fit of Eq. 9.6.

model is chosen to modulate the interference of a polarity change of the electric field during the shower development without being to restrictive on the configuration. The selected configuration is shown in Fig. 9.24.

The lower, positive charge layer was chosen to start at a height of 3000 m a.s.l. reaching its maximum at 4000 m with a field strength of $\varepsilon_{\text{lower}} = 100$ kV/m. From there on the field decreases again, changes polarity and reaches the maximum value of the upper, negative charge layer with $\varepsilon_{\text{upper}} = -100$ kV/m at a height of 7000 m. This layer ends at 8000 m in an uncharged field situation. In addition, a second configuration is simulated with a reduced maximum field strength in the lower layer of $\varepsilon_{\text{lower}} = 50$ kV/m. These values have been selected similar to the atmospheric description presented in Section 4.5. The linear gradient and the strict separation will surely not represent the realistic conditions inside a thundercloud, however it should be sufficient to compare the general features of the shower development.

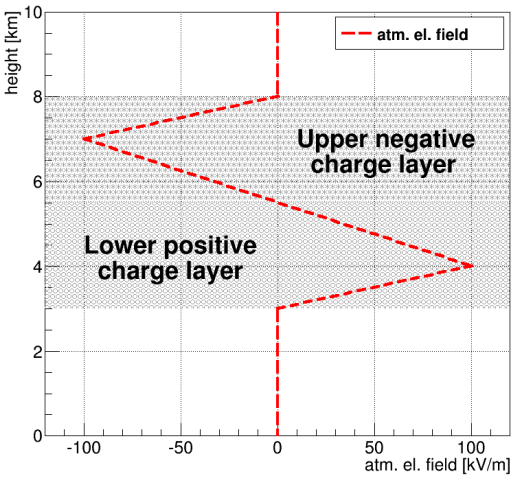

Figure 9.24: Configuration of the atmospheric electric field used for the re-simulation of events.

The resulting polarization patterns for the configuration with an even maximum field strength in both layers are depicted in Fig. 9.25. As can be seen both scenarios would not fit to the expectation of Eq. 9.5, but can be described at least to some extend with the modified version in Eq. 9.6. Inserting a vertical electric field results in a fitted rotation of $\delta \approx 10.8°$ with a phase of $\omega = 126°$, similar to the values for the event from the measured dataset. Most of the participating stations agree quite well with the fit, however, there are few stations, which do not follow this general modification. In case of a horizontal electric field a similar shift is found, but with the rotation going in the opposite direction with $\delta \approx -65°$ this time.

The patterns for the simulations with the reduced field strength in the lower layer yield similar rotations. The spread in between the individual RDS is much larger though and some RDS even show a completely different behaviour. Therefore, it can be concluded that the first scenario is closer to the true conditions for this specific event. However, the polarization pattern for all events, which have been re-simulated with an external electric field do not show a good agreement neither with the measured data nor the underlying expectation for normal conditions. This is additionally expressed in the non-significant fit results for the charge-excess fraction. Furthermore, the simulations do not present any common trends in the fitted rotation and phase parameters with respect to the chosen field. This is most likely a result of the although science-based, but still somehow random selection of the field parametrization, in its strength as well as its structure. So from this point of view it is not reasonable to draw any quantitative conclusion regarding the effect of a strong atmospheric field on the polarization of the radio emission. However, it can be stated from the simulation results that a uniformly aligned field configuration generally gives rise to a global rotation of the polarization angle.

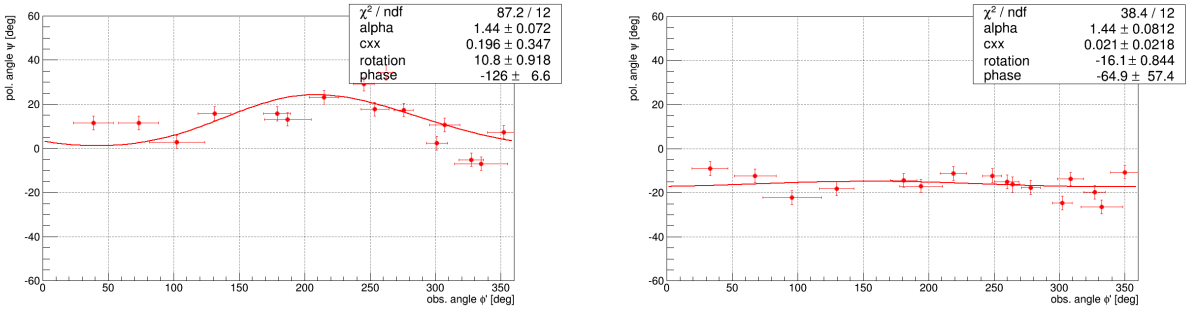

(a) **(b)**

Figure 9.25: Same as Fig. 9.23a, but for the simulated dataset includinging a two-layered vertical (a) and horizontal (b) atmospheric electric field with $|\varepsilon_{\text{lower}}| = |\varepsilon_{\text{upper}}|$.

For the measured event a radiated energy of $E_{\text{RD, data}} = 1.1 \times 10^7$ eV has been reconstructed, while the simulation with normal atmospheric conditions predicts only $E_{\text{RD, sim}} = 1 \times 10^5$ eV, thus a factor 100 lower. In the simulations with the external field ($|\varepsilon_{\text{lower}}| = |\varepsilon_{\text{upper}}|$) the energy increases and is calculated to $E^{+}_{\text{RD, sim}} = 8.5 \times 10^5$ eV for a vertical field and $E^{+}_{\text{RD, sim}} = 8.2 \times 10^5$ eV for a horizontal field respectively, so rather similar for both configurations. But there is still a discrepancy of one order of magnitude between measured and simulated event. This might result from the CoREAS simulations, where low energy particles, which drop below an energy of 150 keV are not further tracked during the shower development. However, when these particles enter a strong atmospheric field, they can be re-accelerated to energies, which makes them relevant again for the further shower development. In addition, they can even participate in the pile-up for the avalanche. These effects will surely lead to an amplified radio emission and therefore to an increased radiated energy.

Due to the enhanced electro-magnetic component in strong electric fields, the air shower will also reach its shower maximum at a lower slant depth, i.e. closer to the observer. The simulation under normal atmospheric conditions yields a geometrical distance to the shower maximum of $R_{\text{max}} = 5330$ m. When an electric field is applied, this value decreases to 4178 m for a vertical field and to 3900 m for a horizontal field. So as soon as the stand-alone determination of R_{max} by the RD reconstruction has reached a mature state, also this quantity can be used to further deduce information on the strength as well as the orientation of the atmospheric electric field.

CHAPTER 10

Summary

The detection of radio emission from air showers has matured towards a promising candidate for the next generation of cosmic ray detectors. In this context many technical and scientific problems have been adressed in the last decade. The general feasibility of this method has been proven by the LOPES and CODALEMA experiments, who set the stage for their successors, which will try to gather all the information hidden in the radio signal.

The Auger Engineering Radio Array located at the Pierre Auger Observatory has mainly driven the evolution towards a large scale application, currently consisting of 153 autonomous radio detector stations on roughly 12 km^2. Being operated for more than five years now several major steps in the development of detector hardware like the physics antenna or front-end electronics have been taken. Also infrastructural issues like data transfer, background removal as well as timing and amplitude calibration have been targeted.

The individual contributions of the emission mechanisms could be tracked down to a significant precision by polarization measurements, identifying the geomagnetic emission as dominant source with a fraction of 14% resulting from a charge-excess. Also the propagation of the emission through the atmosphere has been understood to much better detail. The radio shower front could be determined to be of hyperbolic shape and the flattening of the lateral distribution of the signal strength towards the shower axis was related to the varying index of refraction throughout the development of the air shower. All these findings were added to the existing modelling approaches and the corresponding simulations have started

to converge and finally deliver a consistent picture of the way the radiation is produced, which is in good agreement with the measured data.

The software to analyse these data has to fulfill many requirements in case of a radio detector. As useable information is not only carried in the signal amplitude, but also the frequency spectrum, both domains have to be covered. In addition, the detector itself is a very complex structure and its response to different frequencies or arrival directions has to be known precisely and incorporated while reconstructing the data. In this thesis a detector database has been developed, which yields an individual description of each radio detector station of the array and can be accessed by the analysis framework. It contains a full overview of all hardware components of the specific station, changes can be inserted via an interface on the monitoring webpage. Every configuration is provided with a period of deployment, making the description completly time-dependent.

The RdObserver has been developed as standard reconstruction tool for the externally triggered data measured with AERA. During this process a multitude of different algorithms and cuts were evaluated and integrated into the sequence with special focus on an increased purity of the finally reconstructed dataset. For this purpose, an additional technique for the efficient identification and removal of RFI pulses was implemented and two methods for the selection of stations based on geometrical relations have been tested. Furthermore, a dedicated analysis was performed on the influence of timing-related quantities and improved the overall time consistency with respect to the reconstruction quality. Finally, the purity of the reconstructed dataset could be increased by more than a factor of two, raising from $\sim 30\%$ to now more than 80%.

A complete reconstruction of the full externally triggered dataset collected by AERA so far was performed for the first time. It yields a mean of 9.3 events per day, which show an excellent agreement with the reconstruction of the surface detector, e.g. in shower geometry or the energy spectrum. The distributions of important shower parameters in this dataset have been presented, which now can serve as a starting point for upcoming high level analysis. Still several technical and phenomenological points remain for further improvement, which have also been discussed in this context. An automated production of AERA data using the RdObserver has been set up on a dedicated server at the detector site to provide immediate access to the recently measured data.

This dataset and the corresponding set of simulations were used to investigate another topic, which is also related to the quality of the data. The presence of strong atmospheric fields, most likely contained in thunderstorms, in the emission region of the shower is known to alter the amount as well as the properties of the radiated signal. A method for the estimation of a mean electric field value for a period around a measured event has been developed. The analysis of the conditions at the AERA site using the continuous monitoring of the atmosphere has shown that roughly 4% of the up to now accumulated exposure were taken during periods of strong electric fields. A set of event based cuts has been developed

to provide a high-quality dataset for the evaluation of the influence of the atmospheric field.

In this analysis it was found, that already a field strength of $\varepsilon \geq 100$ V/m (measured on ground level) can significantly increase the radio emission from air showers. This can lead to a misidentification of the shower energy by the radio detector up to two orders of magnitude. However, no unique behaviour with respect to field strength or polarity could be determined. By the usage of twin events, it was shown that the amplified emission results in an increase of the lateral footprint of the radio shower by a factor of 2 to 10. Additionally, it was confirmed that the largest amplification is achieved, if the shower evolves its maximum inside the region of maximum field strength.

A huge discrepancy was found in the signal polarization with respect to the expectations for events measured during thunderstorm conditions, while the events measured during normal field strength are in excellent agreement with simulations. Furthermore, it was shown that for strong electric fields the degree of polarization of the signal is more or less randomly distributed. No significant correlation between the estimated field strength and the charge-excess fraction could be found, though few events have fractions of $\gtrsim 50\%$.

A small subset of events measured during strong atmospheric electric fields and showing a completly different polarization pattern has been re-simulated. This time the simulations included a rather simple two-layered model of a polarized charge region during the shower development. Although the resulting events show an increased radiated energy in comparison to their counterpart simulated with a normal atmosphere, they do not match the measured data by one order of magnitude. The same holds for the polarization patterns, which also show a modified behaviour with respect to the field-less expectation, but no quantitative description can be deduced.

In general, the modification of the emission is surely a result of a combination of conditions. The strength of the atmospheric field surely plays a major role, but in the same context also the location of its source, the distance to the observer and its geometrical position and distance with respect to the path of the air shower is of great importance. This makes a explicit parametrization or prediction of the resulting emission very difficult as an accurate determination of all these components is very hard to achieve.

In summary, it is justified to say, that the radio technique has made significant progress towards being a true alternative in the detection of cosmic rays, be it as part of a hybrid array or potentially even as a stand-alone detector. Especially with the recently published energy correlation and several methods under development for determining the depth of the shower maximum and consequential a sensitivy to the chemical composition, it will be able to take part in the amazing journey in revealing the final mysteries of cosmic rays. The ingredient of this thesis will help with starting a lot of further analysis providing a sophisticated environment for data reconstruction as well as a high-qualtiy dataset.

Appendix

APPENDIX A

RdObserver v1r3 ModuleSequence

```
<module> EventFileReaderOG                    </module>
<module> RdEventPreSelector                   </module>

<module> EventCheckerOG                       </module>
<module> SdQualityCutTaggerOG                 </module>
<module> SdPMTQualityCheckerKG                </module>
<module> TriggerTimeCorrection                </module>
<module> SdCalibratorOG                       </module>
<module> SdBadStationRejectorKG               </module>
<module> SdSignalRecoveryKLT                  </module>
<module> SdEventSelectorOG                    </module>
<module> SdPlaneFitOG                         </module>
<module> LDFFinderKG                          </module>
<try>
  <module> SdHorizontalReconstruction         </module>
</try>

<module> RdEventInitializer                   </module>
<module> RdStationPositionCorrection          </module>
<module> RdStationRejector                    </module>
<module> RdChannelADCToVoltageConverter       </module>
<module> RdChannelSelector                    </module>
<module> RdChannelPedestalRemover             </module>
<module> RdChannelResponseIncorporator        </module>
<module> RdChannelBeaconTimingCalibrator      </module>
<module> RdChannelBeaconSuppressor            </module>
```

```
<module> RdStationTimingCalibrator              </module>
<module> RdStationTimeWindowConsolidator        </module>
<module> RdChannelTimeSeriesTaperer             </module>
<module> RdChannelBandstopFilter                </module>
<module> RdChannelUpsampler                     </module>
<module> RdChannelRiseTimeCalculator            </module>

<module> RdAntennaChannelToStationConverter     </module>
<module> RdStationSignalReconstructor           </module>
<module> RdStationEFieldVectorCalculator        </module>

<loop numTimes="unbounded">
  <module> RdTopDownStationSelector             </module>
  <module> RdPlaneFit                           </module>
</loop>

<module> RdClusterFinder                        </module>
<module> RdPlaneFit                             </module>

<module> RdStationRiseTimeCalculator            </module>
<module> RdEventPostSelector                    </module>
<module> RdLDFMultiFitter                       </module>
<module> Rd2dLDFFitter                          </module>

<try>
  <module> FdCalibratorOG                       </module>
  <module> FdEyeMergerKG                        </module>
  <module> FdPulseFinderOG                      </module>
  <module> FdSDPFinderOG                        </module>
  <module> FdAxisFinderOG                       </module>
  <module> HybridGeometryFinderOG               </module>
  <module> HybridGeometryFinderWG               </module>
  <module> FdApertureLightKG                    </module>
  <module> FdEnergyDepositFinderKG              </module>
  <module> FdProfileReconstructorKG             </module>
</try>

<module> RdStationTimeSeriesWindowCutter        </module>
<module> RdStationTimeSeriesTaperer             </module>
<module> RdREASSimPreparator                    </module>
<module> EventFileExporterOG                    </module>
<module> RecDataWriterNG                        </module>
```

APPENDIX B

RdSimulationObserver v1r3 ModuleSequence

```
<module> EventFileReaderOG </module>

<loop numTimes="1" pushEventToStack="yes">
  <module> RdStationAssociator              </module>
  <module> EventGeneratorOG                 </module>

  <loop numTimes="unbounded" pushEventToStack="no">
    <module> CachedShowerRegeneratorOG      </module>
    <module> TabulatedTankSimulatorKG       </module>
  </loop>

  <module> SdSimulationCalibrationFillerOG </module>
  <module> SdPMTSimulatorOG                 </module>
  <module> SdFilterFADCSimulatorMTU         </module>
  <module> SdBaselineSimulatorOG            </module>
  <module> TankTriggerSimulatorOG           </module>
  <module> TankGPSSimulatorOG               </module>
  <module> CentralTriggerSimulatorXb        </module>
  <module> CentralTriggerEventBuilderOG     </module>
  <module> EventBuilderOG                   </module>

  <module> EventCheckerOG                   </module>
  <module> SdCalibratorOG                   </module>
  <module> SdEventSelectorOG                </module>
  <module> SdMonteCarloEventSelectorOG      </module>
```

```
  <module> SdPlaneFitOG                          </module>
  <module> LDFFinderKG                           </module>
  <module> SdEventPosteriorSelectorOG            </module>
  <module> Risetime1000LLL                       </module>

  <module> RdAntennaStationToChannelConverter    </module>
  <module> RdChannelResponseIncorporator         </module>
  <module> RdChannelResampler                    </module>
  <module> RdChannelTimeSeriesClipper            </module>
  <module> RdChannelVoltageToADCConverter        </module>
  <module> RdChannelNoiseImporter                </module> (optional)

  <module> RdEventInitializer                  </module>
  <module> RdStationRejector                   </module>
  <module> RdChannelADCToVoltageConverter      </module>
  <module> RdChannelSelector                   </module>
  <module> RdChannelPedestalRemover            </module>
  <module> RdChannelResponseIncorporator       </module>
  <module> RdChannelTimeSeriesTaperer          </module>
  <module> RdChannelBandstopFilter             </module>
  <module> RdChannelUpsampler                  </module>
  <module> RdChannelRiseTimeCalculator         </module>

  <module> RdAntennaChannelToStationConverter </module>
  <module> RdStationSignalReconstructor        </module>
  <module> RdStationEFieldVectorCalculator     </module>

  <loop numTimes="unbounded" pushEventToStack="no">
    <module> RdTopDownStationSelector          </module>
    <module> RdPlaneFit                        </module>
  </loop>

  <module> RdClusterFinder                     </module>
  <module> RdPlaneFit                          </module>

  <module> RdStationRiseTimeCalculator         </module>
  <module> RdEventPostSelector                 </module>
  <module> Rd2dLDFFitter                       </module>

  <module> RdStationTimeSeriesWindowCutter     </module>
  <module> RdStationTimeSeriesTaperer          </module>
  <module> RecDataWriterNG                     </module>
</loop>
```

Bibliography

[1] V. F. Hess and W. Kolhoerster. "Über Beobachtungen der durchdringenden Strahlung bei sieben Freiballonfahrten". *Physikalische Zeitschrift* (1912).

[2] P. Auger et al. "Extensive Cosmic-Ray Showers". *Reviews of Modern Physics* 11 (1939), pp. 288–291.

[3] G. A. Askaryan. "Excess negative charge of an electron-photon shower and its coherent radio emission". *Soviet Physics JETP* 14 (1962), pp. 441–443.

[4] J. V. Jelley et al. "Radio Pulses from Extensive Cosmic-Ray Air Showers". *Nature* 205 (1965), pp. 327–328.

[5] I. Lerche. "Theory of Radio Pulses from Cosmic Ray Air Showers". *Nature* 215 (1966), pp. 268–269.

[6] F. D. Kahn and I. Lerche. "Radiation from Cosmic Ray Air Showers". *Proceedings of the Royal Society London A* 289 (1966), pp. 206–213.

[7] H. R. Allan. "Radio Emission from Extensive Air Showers". *Progress in Elementary Particles and Cosmic Ray Physics* 10 (1971), pp. 169–302.

[8] H. Falcke for the LOPES collaboration. "Detection and imaging of atmospheric radio flashes from cosmic ray air showers". *Nature* 435 (2005), pp. 313–316.

[9] A. Belletoile. "First results of the Standalone Antenna Array of the CODALEMA Radio Detection Experiment". *Proceedings of the 32th International Cosmic Ray Conference, Beijing, China* (2011).

[10] E. S. Seo, J. F. Ormes, R. E. Streitmatter, et al. "Measurement of Cosmic-Ray Proton and Helium Spectra during the 1987 Solar Minimum". *Astrophysical Journal* 378 (1991), pp. 763–772.

[11] N. Grigorov et al. "Study of Energy Spectra of Primary Cosmic Rays at Very High Energies on the Proton Series of Satellites". *Space Research XII* (1972), p. 1617.

[12] R. Abbas, T. Abu-Zayyad, and M. Allen. "First Observation of the Greisen-Zatsepin-Kuzmin Suppression". *Physical Review Letters* 100 (2009), p. 101101.

[13] F. Salamida. "Update on the Measurement of the Cosmic Ray Energy Spectrum above 10^{18} eV made using the Pierre Auger Observatory". *Proceedings of the 32th International Cosmic Ray Conference, Beijing, China* (2011).

[14] J. W. Cronin, T. K. Gaisser, and S. P. Swordy. "Cosmic Rays at the Energy Frontier". *Scientific American* (1997), pp. 44–49.

[15] D. Ravignani. "Measurement of the energy spectrum of cosmic rays above 10^{17} eV using the AMIGA 750 m surface detector array of the Pierre Auger Observatory". *Proceedings of the 33th International Cosmic Ray Conference, Rio de Janeiro, Brazil* (2013).

[16] The KASCADE-Grande Collaboration. "Cosmic Rays in the Knee-Region - Recent Results from KASCADE". *Acta Physica Polonica B* 35 (2004), pp. 1799–1812.

[17] A. Hillas. "The Origin of Ultra-High-Energy Cosmic Rays". *Annual Review of Astronomy and Astrophysics* 20 (1984), pp. 425–444.

[18] V. Berezinsky, A. Gazizov, and S. Grigorieva. "Propagation and Signatures of Ultra High Energy Cosmic Rays". *Nuclear Physics B (Proc. Suppl.)* 136 (2004), pp. 147–158.

[19] T. K. Gaisser and T. Stanev. "High-Energy Cosmic Rays". *Nuclear Physics A* 777 (2006), pp. 98–110.

[20] The KASCADE Collaboration. "Energy Spectra of Elemental Groups of Cosmic Rays: Update on the KASCADE Unfolding Analysis". *Astroparticle Physics* 31 (2009), pp. 86–91.

[21] J. Bluemer, R. Engel, and J. R. Hoerandel. "Cosmic Rays from the Knee to the Highest Energies". *Progress in Particle and Nuclear Physics* 63 (2009), pp. 293–338.

[22] M. Unger for the Pierre Auger Collaboration. "Study of the Cosmic Ray Composition above 0.4 EeV using the Longitudinal Profiles of Showers observed at the Pierre Auger Observatory". *Proceedings of the 30th International Cosmic Ray Conference, Merida, Mexico* (2007).

[23] J. W. Fowler et al. "A measurement of the cosmic ray spectrum and composition at the knee". *Journal of Astroparticle Physics* 15 (2001), pp. 49–64.

[24] S. Paling and others for the CACTI Collaboration. *Proceedings of the 25th International Cosmic Ray Conference, Durban, South Africa* (1997).

[25] S. P. Swordy and D. B. Kieda. "Elemental composition of cosmic rays near the knee by multiparameter measurements of air showers". *Journal of Astroparticle Physics* 13 (2000), pp. 137–150.

[26] D. J. Bird for the HIRES Collaboration. "The cosmic ray energy spectrum observed by the Fly's Eye". *Astrophysical Journal* (1994), pp. 491–502.

[27] A. A. Watson. "Ultra-high-energy cosmic rays: The experimental situation". *Physical Reports* (2000), pp. 309–327.

[28] F. Arqueros for the HEGRA Collaboration. "Energy spectrum and chemical composition of cosmic rays between 0.3 PeV and 10 PeV determined from the Cherenkov-light and charged-particle distributions in air showers". *Astronomy & Astrophysics* 359 (2000), pp. 682–694.

[29] T. Abu-Zayyad et al. "Evidence for Changing of Cosmic Ray Composition between 10^{17} and 10^{18} eV from Multicomponent Measurements". *Physical Review Letters* 84 (2000), pp. 4276–4279.

[30] R. U. Abbasi and others for the HiRes Collaboration. "A Study of the Composition of Ultra High Energy Cosmic Rays Using the High Resolution Fly's Eye". *Astrophysical Journal* 622 (2005), pp. 910–926.

[31] M. Cha et al. *Proceedings of the 27th International Cosmic Ray Conference, Hamburg, Germany* (2001).

[32] J. Dickinson et al. *Proceedings of the 26th International Cosmic Ray Conference, Salt Lake City, United States of America* (1999).

[33] D. Chernov et al. "Primary energy spectrum and mass composition determined with the Tunke EAS Cherenkov Array". *International Journal of Modern Physics A* 20 (2006), pp. 6799–6801.

[34] S. Knurenko et al. *Proceedings of the 27th International Cosmic Ray Conference, Hamburg, Germany* (2001).

[35] N. N. Kalmykov and S. Ostapchenko. "Comparison of chracteristics of the nucleus nucleus interaction in the model of the quark-gluon strings and in the superposition model". *Soviet Journal of Nuclear Physics* (1989), pp. 315–318.

[36] S. Ostapchenko. "Non-linear screening effects in high energy hadronic interactions". *Physical Review D74* (2006), p. 014026.

[37] R. Engel et al. "Air shower calculations with the new version of SIBYLL". *Proceedings of the 26th International Cosmic Ray Conference, Salt Lake City, United States of America* (1999).

[38] T. Pierog and K. Werner. "The hadronic interaction model EPOS and air shower simulations: New results on muon production". *Proceedings of the 30th International Cosmic Ray Conference, Merida, Mexico* (2007).

[39] A. Letessier-Selvon for the Pierre Auger Collaboration. "Highlights from the Pierre Auger Observatory". *Highlight contribution of the 33rd International Cosmic Ray Conference, Rio de Janeiro, Brazil* (2013).

[40] E.-J. Ahn et al. "Cosmic ray interaction event generator SIBYLL 2.1". *Physical Review D* 80 (2009), p. 094003.

[41] T. Pierog et al. "EPOS LHC : test of collective hadronization with LHC data". *arXiv:1306.0121v2* (2013).

[42] S. Ostapchenko. "QGSJET-II: physics, recent improvements, and results for air showers". *European Physical Journal Conferences* 20 (2013).

[43] E. Fermi. "On the Origin of Cosmic Radiation". *Physics Review* 75 (1949), pp. 1169–1174.

[44] T. K. Gaisser. *Cosmic Rays and Particle Physics*. Cambridge and New York, Cambridge University Press, 1990.

[45] R. D. Blandford and J. P. Ostriker. "Particle Acceleration by Astrophysical Shocks". *Astrophysical Journal* 221 (1978), pp. L29–L32.

[46] The Pierre Auger Collaboration. "Searches for Anisotropies in the Arrival Directions of the Highest Energy Cosmic Rays Detected by the Pierre Auger Observatory". *Astrophysical Journal* 804 (2014).

[47] D. F. Torres and L. A. Anchordoqui. "Astrophysical Origins of Ultrahigh Energy Cosmic Rays". *Reports on Progress in Physics* 67 (2004), pp. 1663–1730.

[48] C. T. Hill. "Monopolonium". *Nuclear Physics* B224 (1983), p. 469.

[49] M. B. Hindmarsh and T. W. B. Kibble. "Cosmic Strings". *Reports on Progress in Physics* 68 (1995), pp. 477–562.

[50] V. Berezinsky, M. Kachelriess, and A. Vilenkin. "Ultra-High Energy Cosmic Rays without GZK Cutoff". *Physical Review Letters* 79 (1997), pp. 4302–4305.

[51] M. Birkel and S. Sarkar. "Extremely High Energy Cosmic Rays from Relic Particle Decays". *Astroparticle Physics* 9 (1998), pp. 297–309.

[52] Z. Fodor and S. D. Katz. "Grand Unification Signal from Ultrahig-Energy Cosmic Rays?" *Physical Review Letters* 86 (2001), pp. 3224–3227.

[53] T. J. Weiler. "Resonant Absorption of Cosmic Ray Neutrinos by the Relic Neutrino Background". *Physical Review Letters* 49 (1982), p. 234.

[54] D. Fargion, B. Mele, and A. Salis. "Ultrahigh Energy Neutrino Scattering onto Relic Light Neutrinos in Galactic Halo as a Possible Source of Highest Energy Extragalactic Cosmic Rays". *Astrophysical Journal* 517 (1999), pp. 725–733.

[55] C. Bleve for the Pierre Auger Collaboration. "Update of the neutrino and photon limits from the Pierre Auger Observatory". *Proceedings of the 34th International Cosmic Ray Conference, The Hague, The Netherlands* (2015).

[56] J. D. Barrow, P. G. Ferreira, and J. Silk. "Constraints on a Primordial Magnetic Field". *Physical Review Letters* 78 (1997), pp. 3610–3613.

[57] P. P. Kronberg. "Extragalactic Magnetic Fields". *Reports on Progress in Physics* 57 (1994), pp. 325–382.

[58] T. Stanev, D. Seckel, and R. Engel. "Propagation of Ultra-High Energy Protons in Regular Extragalactic Magnetic Fields". *Physical Review D* 68 (2003), p. 103004.

[59] A. A. Penzias and R. W. Wilson. "A Measurement of Excess Antenna Temperature at 4080-Mc/s". *Astrophysical Journal* 142 (1965), pp. 419–421.

[60] K .Greisen. "End to the Cosmic Ray Spectrum". *Physical Review Letters* 16 (1966), pp. 748–750.

[61] G. T. Zatsepin and V. A. Kuzmin. "Upper Limit of the Spectrum of Cosmic Rays". *JETP Letters* 4 (1966), pp. 78–80.

[62] G. R. Blumenthal. "Energy Loss of High-Energy Cosmic Rays in Pair-Producing Collisions with Ambient Photons". *Physical Review D* 1 (1970), pp. 1596–1602.

[63] D. Allard, M. Ave, N. Busca, et al. "Cosmogenic Neutrinos from the Propagation of Ultrahigh Energy Nuclei". *Journal of Cosmology and Astroparticle Physics* 09 (2006), p. 5.

[64] J. W. Cronin. "Cosmic Rays: The Most Energetic Particles in the Universe". *Reviews of Modern Physics* 71 (1999), pp. 165–172.

[65] J. Linsley. "Evidence for a Primary Cosmic-Ray Particle with Energy 10^{20} eV". *Astrophysical Journal* 789 (2014), p. 160.

[66] The HiRes Collaboration. "Observation of the GZK Cutoff using the HiRes Detector". *Nuclear Physics B (Proc. Suppl.)* 165 (2006), pp. 19–26.

[67] The Pierre Auger Collaboration. "Measurement of the Energy Spectrum of Cosmic Rays above 10^{18} eV using the Pierre Auger Observatory". *Physics Letters B* 685 (2010), pp. 239–246.

[68] The AGASA Collaboration. "The Anisotropy of Cosmic Ray Arrival Dircetions around 10^{18} eV". *Astroparticle Physics* 10 (1999), pp. 303–311.

[69] J. A. Bellido et al. "Southern Hemisphere Observations of a 10^{18} eV Cosmic Ray Source near the Direction of the Galactic Centre". *Astroparticle Physics* 15 (2001), pp. 167–175.

[70] Pierre Auger Collaboration. "Anisotropy Studies around the Galactic Centre at EeV Energies with the Auger Observatory". *Astroparticle Physics* 27 (2007), pp. 244–253.

[71] The Pierre Auger Collaboration. "Update on the correlation of the Highest-Energy Cosmic Rays with Nearby Extragalactic Matter". *Astroparticle Physics* 34 (2010), pp. 314–326.

[72] The Pierre Auger Collaboration. "Correlation of the Highest-Energy Cosmic Rays with Nearby Extragalactic Objects". *Science* 318 (2007), pp. 938–943.

[73] M. P. Véron-Cetty and P. Véron. "A Catalogue of Quasars and Active Nuclei: 12th Edition". *Astronomy & Astrophysics* 455 (2006), pp. 774–777.

[74] S. Fliescher. "Antenna Devices and Measurement of Radio Emission from Cosmic Ray induced Air Showers at the Pierre Auger Observatory". Ph.D. Thesis. RWTH Aachen University, 2011.

[75] W. Heitler. *Quantum Theory of Radiation*. Oxford University Press, 1944.

[76] T. Bergmann et al. "One-Dimensional Hybrid Approach to Extensive Air Shower Simulations". *Astroparticle Physics* 26 (2007), pp. 420–432.

[77] D. Heck et al. *CORSKIA: A Monte Carlo Code to Simulate Extensive Air Showers*. FZKA-6019, Forschungszentrum Karlsruhe, 1998.

[78] D. Heck and T. Pierog. *Extensive Air Shower Simulation with CORSIKA: A User's Guide*. Forschungszentrum Karlsruhe, 2010.

[79] D. Kuempel. "Multivariate Search for a Directional Excess of EeV Photons with the Pierre Auger Observatory". Ph.D. Thesis. Bergische Universität Wuppertal, 2011.

[80] T. Gaisser and A. Hillas. "Reliability of the Method of Constant Intensity Cuts for Reconstructing the Average Development of Vertical Showers". *Proceedings of the 15th International Cosmic Ray Conference, Plovdiv, Bulgaria* (1977).

[81] A. Haungs, H. Rebel, and M. Roth. "Energy Spectrum and Mass Composition of High-Energy Cosmic Rays". *Reports on Progress in Physics* 66 (2003), p. 1145.

[82] A. F. Nelles. "Radio emission of air showers - The perspective of LOFAR and AERA". Ph.D. Thesis. Radboud University Nijmegen, 2014.

[83] F. Arciprete, M. Bohacova, J. Bluemer, et al. "AIRFLY: Measurement of the Air Fluorescence Radiation Induced by Electrons". *Nuclear Physics B (Proc. Suppl.)* 150 (2006), pp. 186–189.

[84] D. J. Bird et al. "Detection of a Cosmic Ray with Measured Energy well beyond the Expected Spectral Cutoff due to Cosmic Microwave Radiation". *Astrophysical Journal* 441 (1995), pp. 144–150.

[85] M. Nagano and A. A. Watson. "Observation and Implications of the Ultrahigh-Energy Cosmic Rays". *Review of Modern Physics* 72 (2000), pp. 689–732.

[86] P. W. Gorham et al. "Observations of Microwave Continuum Emission from Air Shower Plasmas". *Physical Review D* 78 (2008), p. 032007.

[87] R. Smida et al. "First Experimental Characterization of Microwave Emission from Cosmic Ray Air Showers". *Physical Review Letters* 113 (2014), p. 221101.

[88] J. Alvarez-Muniz et al. "Search for microwave emission from ultrahigh energy cosmic rays". *Physical Review D* 86 (2012), p. 051104.

[89] R. Gaior. "Detection of cosmic rays using microwave radiation at the Pierre Auger Observatory". *Proceedings of the 33th International Cosmic Ray Conference, Rio de Janeiro, Brazil* (2013).

[90] G. A. Askaryan. *Atomnaya Energiya* 3 (1957), p. 152.

[91] F. G. Schröder for the LOPES collaboration. "Cosmic Ray Measurements with LOPES: Status and Recent Results". *ARENA conference, Erlangen, Germany, AIP Conf. Proc.* 1535 (2012).

[92] A. van den Berg. "Radio detection of cosmic rays at the southern Auger Observatory". *Proceedings of the 31th International Cosmic Ray Conference, Lodz, Poland* (2009).

[93] The LOFAR Collaboration. "LOFAR: The LOw-Frequency ARray". *Astronomy & Astrophysics* 556 (2013), A2.

[94] D. Kostunin for the Tunka-Rex Collaboration. "Tunka-Rex: Status and results of the first measurements". *Nuclear Instruments and Methods in Physics Research A* 742 (2014), pp. 89–94.

[95] H. Flacke and P. Gorham. "Detecting Radio Emission from Cosmic Ray Air Showers and Neutrinos with a Digital Radio Telescope". *Astroparticle Physics* 19 (2003), p. 477.

[96] H. Flacke and T. Huege. "Radio Emission from Cosmic Ray Air Showers: Coherent Geosynchrotron Radiation". *Astronomy and Astrophysics* 412 (2003), pp. 19–34.

[97] T. Huege et al. "The Convergence of EAS Radio Emission Models and a Detailed Comparison of REAS3 and MGMR Simulations". *Nuclear Instruments and Methods in Physics Research A* 662 (2012), pp. 179–186.

[98] H. Schoorlemmer. "Tuning in on Cosmic Rays". Ph.D. Thesis. Radboud University Nijmegen, 2012.

[99] P. Grieder. *Extensive Air Showers*. Springer Berlin Heidelberg, 2010.

[100] W. N. Charman. "Atmospheric Electric Field as a Possible Cause of Radio Pulses from Extensive Air Showers". *Nature* 215 (1967), p. 497.

[101] S. Buitink et al. "Simulation of radio emission from air showers in atmospheric electric fields". *Astroparticle Physics* 33 (2010), p. 296.

[102] E. D. Fraenkel. "From Radio Pulse to Elusive Particle". Ph.D. Thesis. Rijksuniversiteit Groningen, 2014.

[103] J. Jackson. *Classical Electrodynamics, Vol. 2*. John Wiley & Sons Inc., 1975.

[104] A. Horneffer. "Primary Particle Energy Calibration of the EAS Radio Pulse Height". *Proceedings of the 30th International Cosmic Ray Conference, Merida, Mexico* (2007).

[105] W. D. Apel et al. "The Wavefront of the Radio Signal Emitted by Cosmic Ray Air Showers". *Journal of Cosmology and Astroparticle Physics* 09 (2014), p. 25.

[106] F. G. Schröder. "Instruments and Methods for the Radio Detection fo High Energy Cosmic Rays". Ph.D. Thesis. Karlsruhe Institute of Technology, 2010.

[107] A. Corstanje et al. "The Shape of the Radio Wavefront of Extensive Air Showers as Measured with LOFAR". *Astroparticle Physics* 61 (2015), pp. 22–31.

[108] R. S. Roger et al. "The Radio Emission from the Galaxy at 22 MHz". *Astronomy & Astrophysics Suppl.* 137 (1999), pp. 7–19.

[109] T. Huege, M. Ludwig, and C. W. James. "Simulating Radio Emission from Air Showers with CoREAS". *American Institute of Physics Conference Series* 1535 (2013), pp. 128–132.

[110] J. Alvarez-Muniz, W. R. Carvalho Jr., and E. Zas. "Monte Carlo Simulations of Radio Pulses in Atmospheric Showers using ZHAires". *Astroparticle Physics* 35 (2011), pp. 325–341.

[111] S. J. Sciutto. "AIRES: A System for Air Shower Simulations (Version 2.2.0)". *arXiv Astrophysics ePrint* (1999).

[112] C. W. James et al. "General Description of Electromagnetic Radiation Processes based on Instantaneous Charge Acceleration in 'End-Points'". *Physical Review E* 84 (2011), p. 056602.

[113] M. Ludwig and T. Huege. "REAS3: Monte Carlo Simulations of Radio Emission from Cosmic Ray Air Showers using an Ënd-pointFormalism". *Astroparticle Physics* 34 (2011), pp. 438–446.

[114] O. Scholten, K. Werner, and F. Rusydi. "A Macroscopic Description of Coherent Geo-Magnetic Radiation from Cosmic Ray Air Showers". *Astroparticle Physics* 29 (2008), p. 94.

[115] K. Werner, K .D. de Vries, and O. Scholten. "A Realistic Treatment of Geo-Magnetic Cherenkov Radiation from Cosmic Ray Air Showers". *Astroparticle Physics* 37 (2012), pp. 5–16.

[116] B. Revenu. "Overview of MHz Air Shower Radio Experiments and Results". *Proceedings of the ARENA conference, Erlangen, Germany* (2012).

[117] K. F. Weidenhaupt. "Antenna Calibration and Energy Measurement of Ultra-High Energy Cosmic Rays with the Auger Engineering Radio Array". Ph.D. Thesis. RWTH Aachen University, 2014.

[118] The Pierre Auger Collaboration. "Probing the Radio Emission from Air Showers with Polarization Measurements". *Physical Review D* 89 (2014).

[119] F. Jonsson. "The Nonlinear Optics of Magneto-Optic Media". Ph.D. Thesis. The Royal Institute of Technology, Stockholm, 2000.

[120] W. D. Apel et al. "Lateral Distribution of the Radio Signal in Extensive Air Showers Measured with LOPES". *Astroparticle Physics* 32 (2010), p. 294.

[121] A. Rebai et al. "Correlations in Energy in Cosmic Ray Air Showers Radio-Detected by CODALEMA". *arXiv:1210:1739* (2010).

[122] V. Marin for the CODALEMA Collaboration. "Charge excess signature in the CODALEMA data. Interpretation with SELFAS2". *Proceedings of the 32th International Cosmic Ray Conference, Beijing, China* (2011).

[123] The Pierre Auger Collaboration. "Energy Estimation of Cosmic Rays with the Engineering Radio Array of the Pierre Auger Observatory". *Physical Review D (to be published)* (2015).

[124] The Pierre Auger Collaboration. "Atmospheric effects on extensive air showers observed with the surface detector of the Pierre Auger observatory". *Astroparticle Physics* 32 (2009), pp. 89–99.

[125] W. Charman. "Radio Pulses from Extensive Air Showers as a Result of Movement of Slow Electrons in the Atmospheric Electric Field". *Journal of Atmospheric and Terrestrial Physics* 30 (1968), p. 195.

[126] R. R. Wilson. "Atmospheric Signals Caused by Cosmic-Ray Showers". *Physical Review Letters* 108 (1957), p. 155.

[127] N. Mandolesi, G. Morigi, and G. G. C. Palumbo. "Radio Pulses from Extensive Air Showers during Thunderstorms - the Atmospheric Electric Field as a Possible Cause". *Journal of Atmospheric and Terrestrial Physics* 36 (1974), pp. 1431–1435.

[128] M. Stolzenburg et al. "Electrical Structure in Thunderstorm Convective Regions - 1. Mesoscale Convective Systems". *Journal of Geophysical Research* 103 (1998), pp. 14059–14078.

[129] S. Nehls. "Calibrated Measurements of the Radio Emission of Cosmic Ray Air Showers". Ph.D. Thesis. Universität Karlsruhe, 2008.

[130] J. R. Dwyer, M. A. Uman, and H. K. Rassoul. "Remote Measurement of Thundercloud Electrostatic Fields". *Journal of Geophysical Research* 114 (2009), p. D09208.

[131] M. Ender for the LOPES Collaboration. "Radio Emission of Extensive Air Showers during Thunderstorms". *Proceedings of the 31th International Cosmic Ray Conference, Lodz, Poland* (2009).

[132] A. V. Gurevich, G. M. Milikh, and R. Roussel-Dupre. "Runaway electron mechanism of air breakdown and preconditioning during a thunderstorm". *Physics Letters A* 165 (1992), p. 463.

[133] A. V. Gurevich and K. P. Zybin. "Runaway Breakdown and the Mysteries of Lightning". *Physics Today* 58/5 (1995), pp. 37–43.

[134] A. V. Gurevich et al. "Radio Emission due to Simultaneous Effect of Runaway Breakdown and Extensive Atmospheric Showers". *Physics Letters A* 301 (2002), pp. 320–326.

[135] S. Buitink for the LOPES Collaboration. "Amplified Radio Emission from Cosmic Ray Air Showers in Thunderstorms". *Astronomy & Astrophysics* 1467 (2008), pp. 385–394.

[136] H. P. Dembinski. "Measurement of the flux of ultra high energy cosmic rays using data from very inclined air showers at the Pierre Auger Observatory". Ph.D. Thesis. RWTH Aachen University, 2009.

[137] C. Bonifazi. "The Angular Resolution of the Pierre Auger Observatory". *Nuclear Physics B (Proc. Suppl.)* 190 (2009), pp. 20–25.

[138] D. Veberic and M. Roth. "SD Reconstruction; Offline Reference Manual". *internal Auger note* GAP-2005-035 (2005).

[139] The Pierre Auger Collaboration. "The Fluorescence Detector of the Pierre Auger Observatory". *Nuclear Instruments and Methods in Physics Research A* 620 (2010), pp. 227–251.

[140] The Pierre Auger Collaboration. "Depth of Maximum of Air-Shower Profiles at the Pierre Auger Observatory: Measurements at Energies above $10^{17.8}$ eV". *Physical Review D* 90 (2014), p. 122005.

[141] L. Valore. "Atmospheric Aerosol Attenuation Measurements at the Pierre Auger Observatory". *AtmoHEAD Conference proceeding* (2013).

[142] S. Y. BenZvi. "The Lidar System of the Pierre Auger Observatory". *Nuclear Instruments and Methods in Physics Research A* 574 (2007), pp. 171–184.

[143] F. Suarez for the Pierre Auger Collaboration. "The AMIGA Muon Detectors of the Pierre Auger Observatory: Overview and Status". *Proceedings of the 33th International Cosmic Ray Conference, Rio de Janeiro, Brazil* (2013).

[144] K.-H. Kampert for the Pierre Auger Collaboration. "The Pierre Auger Observatory: Selected Results and Future Plans". *Proceedings of VHEPA2014 (to be published)* (2014).

[145] The AERA Group. "AERA proposal for the construction of the 20 km^2 Auger Engineering Radio Array at the Southern Auger Observatory". *internal Auger note* GAP-2009-172 (2009).

[146] J. Neuser for the Pierre Auger Collaboration. "Detection of Radio Emission in the MHz Range at the Pierre Auger Observatory". *Proceedings of the ARENA conference, Anapolis, USA (to be published)* (2014).

[147] A. M. van den Berg et al. "First Detection of Radio Signals from Cosmic Rays at the Pierre Auger Observatory". *internal Auger note* GAP-2007-065 (2007).

[148] J. Coppens et al. "Observation of Radio Signals from Air Showers at the Pierre Auger Observatory". *Nuclear Instruments and Methods in Physics Research A* 604 (2009), p. 41.

[149] The Pierre Auger Collaboration. "Results of a Self-Triggered Prototype System for the Radio-Detection of Extensive Air Showers at the Pierre Auger Observatory". *Journal of Instrumentation* 7 (2012), p. 11023.

[150] S. Messina, J. van den Eijnden, and A. van den Berg. "Energy Calibration for the 433 m SD Infill Array". *internal Auger note* GAP-2014-094 (2014).

[151] K. F. Weidenhaupt. "LPDA-Antennas for Large Scale Radio Detection of Cosmic Rays at the Pierre-Auger-Observatory". Diploma Thesis. RWTH Aachen University, 2009.

[152] M. Erdmann et al. "Antenna Alignment for the first 24 Stations of AERA". *internal Auger note* GAP-2010-083 (2010).

[153] The Pierre Auger Collaboration. "Antennas for the detection of radio emission pulses from cosmic-ray induced air showers at the Pierre Auger Observatory". *Journal of Instrumentation* 7 (2012), p. 10011.

[154] J. B. Eser. "Verschiedene Methoden der Zeitkalibration für das Auger Engineering Radio Array". Diploma Thesis. Karlsruhe Institute of Technology, 2013.

[155] A. van den Berg adn G. Zarza and D. M. Varnav. "Communication System for the Auger Engineering Radio Array at the Southern Auger Observatory". *internal Auger note* GAP-2011-035 (2011).

[156] J. L. Kelley for the Pierre Auger Collaboration. "Data Acquisition, Triggering and Filtering at the Auger Engineering Radio Array". *Proceedings of the Very Large Volume Neutrino Telescope Workshop, Erlangen, Germany* (2011).

[157] B. Revenu et al. "AERA Central Trigger". *internal Auger note* GAP-2012-115 (2012).

[158] M. Melissas, T. Huege, and H. Schieler. "Weather Monitoring at the Central Radio Station". *internal Auger note* GAP-2011-066 (2011).

[159] T. Huege et al. "Nanosecond-level time synchronization of autonomous radio detector stations using a reference beacon and commercial airplanes". *Journal of Instrumentation (to be published)* (2015).

[160] F. G. Schrøder et al. "New Method for the Time Calibration of an Interferometric Radio Antenna Array". *Nuclear Instruments and Methods in Physics Research A* 615 (2010), pp. 277–284.

[161] A. Nelles et al. "A Survey of Narrowband and Broadband Radio-frequency Interference at AERA". *internal Auger note* GAP-2011-062 (2011).

[162] J. Neuser. "Radio Measurement of Extensive Air Showers at the Pierre Auger Observatory". Master Thesis. Bergische Universität Wuppertal, 2010.

[163] T. Paul et al. "The Offline Software Framework of the Pierre Auger Observatory". *Nuclear Instruments and Method in Physical Research A* 580 (2007), pp. 1485–1496.

[164] C. Glaser. "Energy Measurement and Strategy for a Trigger of Ultra High Energy Cosmic Rays Measured with Radio Technique at the Pierre Auger Observatory". Master Thesis. RWTH Aachen, 2012.

[165] I. Sedelnik et al. "Infill event reconstruction using the Auger Offline Software". GAP-2011-013 (2011). internal Auger note.

[166] A. Lang. "Time Calibration of the Auger Engineering Radio Array Using Airplanes". Diploma Thesis. Karlsruhe Institute of Technology, 2014.

[167] J. Maller. "Radio détection des gerbes dans le domaine du MHz à AUGER et CODALEMA". Ph.D. Thesis. SUBATECH Nantes, 2015.

[168] D. Kuempel. "Geometry Reconstruction of Fluorescence Detectors Revisited". Diploma Thesis. Bergische Universität Wuppertal, 2007.

[169] S. Falk et al. "A First Look at HEAT Data". *internal Auger note* GAP-2010-123 (2010).

[170] A. Tapia et al. "Study of the Infill array using Monte Carlo simulations with Offline". *internal Auger note* GAP-2012-004 (2012).

[171] F. Szeibert. "Radiomessung von ausgedehnten Luftschauern am Pierre Auger Observatorium - Optimierte Ereignisselektion und Hardware-Monitoring". Diploma Thesis. Bergische Universität Wuppertal, 2013.

[172] S. Mathys, J. Rautenberg, and J. Neuser. "Development and applications of a ROOT based IO library for AERA". *internal Auger note* GAP-2015-011 (2015).

[173] Q. Dorosti. private communication. 2014.

[174] O. Kambeitz for the Pierre Auger Collaboration. "Radio Detection of Horizontal Extensive Air Showers with AERA". *Proceedings of the ARENA conference, Anapolis, USA (to be published)* (2014).

[175] P. Schellart for the LOFAR collaboration. "Probing Atmospheric Electric Fields in Thunderstorms through Radio Emission from Cosmic-Ray-Induced Air Showers". *Physical Review Letters* 114 (2015), p. 165001.

[176] G. Battistoni et al. "FLUKA as a new high energy cosmic ray generator". *Nuclear Instruments and Methods in Physics Research A* 626-627 (2011), S191–S192.

[177] T. Huege. private communication. 2015.

[178] A. Nelles et al. "The radio emission pattern of air showers as measured with LOFAR - a tool for the reconstruction of the energy and the shower maximum". *Journal of Cosmology and Astroparticle Physics* 05 (2015), p. 18.

[179] P. Schellart for the LOFAR collaboration. "Polarized Radio Emission from Extensive Air Showers Measured with LOFAR". *Journal of Cosmology and Astroparticle Physics* 10 (2014), p. 014.

Acknowledgement

Although this thesis is supposed to be a representation of independent scientific research as stated in the adjacent declaration, it would not have been possible without the support of many people in multifaceted ways.

First of all, I am very thankful to Prof. Karl-Heinz Kampert, who offered me the opportunity to work on this interesting topic. Beside his mentoring, he was always willing to discuss pending questions, related to physics or any other business, even in busy times.

I am grateful to Dr. Tim Huege for writing the second report as well as many fruitful discussions and input especially with respect to the usage of Offline and CoREAS.

I am deeply indepted to Dr. Julian Rautenberg. Be it thematic discussions, technical support, travel company or just an open ear, he was always there, when needed. Thanks for proofreading, all the helpful comments and the assistance during the whole time.

Very special thanks go to Lukas "Justus" Niemietz and Sven "Peter" Querchfeld. Not only have they been the best detective associates I have ever had, but have become very close friends during our Ph.D. time in Wuppertal. Hopefully, there are still many "cases" to be solved in the future.

I really enjoyed being part of the Astroparticle Group in Wuppertal. Specifically, I would like to mention Ruth Hoffmann, Sebastian Mathys and Jörg Förtsch in this context. Thank you for helping in creating this friendly and relaxed working atmosphere and for all the fun we had during coffee breaks or the "Mettwoch" meetings. Many thanks also to Ms. Schaarwächter for assisting me in all the secretarial and logistic work.

Furthermore, I would like to thank the members of the AERA and Radio Offline Group for all the helpful discussions during the meetings or teleconferences and for the exciting time during the deployment in Argentina. I am thankful to Anna Nelles, Christan Glaser, Qader Dorosti and Johannes Schulz for sharing their expertise, keeping up the mood while bug-tracking and all the co-operation and cross-checking during the code development.

I am incredibly grateful to my family and my friends, who supported me all the way with encouragement, patience and so many other things. Finally, I want to express my deep gratitude to Anna for her continuous support, for being my backing and for accepting my mental absence especially during the final months of this thesis.

Erklärung

Eidesstattliche Erklärung

Hiermit versichere ich, die vorliegende Arbeit selbstständig und nur unter Verwendung der angegebenen Literatur und Hilfsmittel erstellt zu haben.

Die Arbeit wurde bisher in gleicher oder ähnlicher Form keiner anderen Prüfungsbehörde vorgelegt und auch nicht veröffentlicht.

Wuppertal, den _____ _____

Unterschrift